INTERPRETATION OF DOWNHOLE TEMPERATURE MEASUREMENTS

FOR MULTISTAGE FRACTURE STIMULATION IN HORIZONTAL WELLS

A Dissertation

by

SHUANG ZHANG

Submitted to the Office of Graduate and Professional Studies of
Texas A&M University
in partial fulfillment of the requirements for the degree of

DOCTOR OF PHILOSOPHY

Chair of Committee,	Ding Zhu
Committee Members,	A. Daniel Hill
	Akhil Datta-Gupta
	Yalchin Efendiev
Head of Department,	Jeff Spath

August 2019

Major Subject: Petroleum Engineering

ABSTRACT

The ideal outcomes of multistage hydraulic fracturing in horizontal wells are to create a controlled fracture distribution along the horizontal well with maximum contact with the reservoir which can provide the sufficient production after stimulation. Downhole temperature sensing is one of the valuable tools to monitor hydraulic fracture treatment process and diagnose fracture performance during production. Today, there are still many challenges in quantitative interpretations of distributed downhole temperature measurements for flow profiling. These challenges come from the following aspects: the uncertainties of the parameters ranging from the reservoir properties, well completion, to fracture geometry; the need of a fast and robust forward model to simulate temperature behavior from injection, shut-in and production accurately; the need of an inversion methodology that can converge fast, reduce the uncertainties and lead to a practically meaningful solution.

In this study, an integrated multiphase black-oil thermal and flow model is presented. This model is developed to simulate the transient temperature and flow behavior during injection, shut-in, and production for multistage hydraulic fractured horizontal wells. The model consists of a reservoir model and a wellbore model, which are coupled interactively through boundary conditions to each other. It is assumed that the oil and water components are immiscible, and the gas component is only soluble in oil. Comparing with the compositional model, this model has an improved computational

efficiency while still maintains the maximum robustness. This study gives guidance on when and how to apply this black-oil thermal model to fulfill its full advantages.

This study also proposed a new temperature interpretation methodology which incorporates the black-oil thermal model as the forward model for temperature simulation and the inversion model for inverting the flow rate profile along the wellbore by matching the simulated temperature with the measured temperature. The sensitivity study is first performed to determine the impact of parameters on temperature behavior such as fracture half-length, fracture permeability, matrix permeability, and matrix porosity. The inversion model uses the initial analysis on temperature gradient to identify the initial guess of fluid distribution which leads to a faster convergence as well as a sensible solution. The Levenberg-Marquart algorithm is adopted to update the inversion parameters during each iteration. A synthetic example with multiple fractures is presented to test the interpretation procedure's accuracy and speed.

The interpretation methodology is further applied to two different filed cases. One is a single-phase gas producing horizontal well with multiple hydraulic fractures; the other one is a two-phase water-oil producing horizontal well with multiple hydraulic fractures. This study illustrates how to adjust the methodologies and perform the analysis for each particular case and explains how to reduce the uncertainties and increase the interpretation efficiency. The results reveal that this temperature interpretation methodology is efficient and effective to translate temperature measurements to flow profile quantitatively with reasonable assumptions.

DEDICATION

       To my grandmother, parents and husband for their endless love, encouragement, and support.

ACKNOWLEDGMENTS

I want to express my sincere gratitude to my committee chair and advisor, Dr. Ding Zhu for her guidance, encouragement, and support through my Ph.D. study. Also, I would like to give special thanks to Dr. A. Daniel Hill for his valuable advice and motivation through all my study. I have learned from them not only the knowledge but also the wisdom and positive attitude towards my future career and life.

I want to thank Dr. Akhil Datta-Gupta for his valuable ideas and discussions for this work. His course on data integration and his advice are significant to the foundation of this work. I also would like to thank Dr. Yalchin Efendiev for his valuable suggestions and comments.

Thanks also go to my friends and colleagues and the department faculty and staff for making my time at Texas A&M University a great experience.

Finally, thanks to my parents for their love and encouragement, and to my beloved husband Xu Xue for his endless inspiration, support, and love.

CONTRIBUTORS AND FUNDING SOURCES

Contributors

This work was supervised by a dissertation committee consisting of Professor Ding Zhu [advisor] and Professors A. Daniel Hill and Akhil Datta-Gupta of the Department of Petroleum Engineering and Professor Yalchin Efendiev of Department of Mathematics.

All work for the dissertation was completed independently by the student.

Funding Sources

NOMENCLATURE

A	Surface area of the well segment, m^2
A	Accumulative term
A_f	Face area between the cell and its adjacent cell, m^2
B	Formation volume factor
b	Inverse of formation volume factor
C_{Go}	Mass fraction of dissolved gas in the oil phase
C_{Oo}	Mass fraction of oil component in the oil phase
C_o	Distribution parameter
C_p	Specific heat capacity, J/kg·K
c	Isothermal compressibility, 1/psi
c_l	Specific heat capacity of fluid, J/kg·K
c_r	Isothermal compressibility of the rock, 1/psi
c_t	Total compressibility, 1/psi
D	Pipe inner diameter, m
d	Observed temperature data, ^{o}F
f	Frictional factor
f	Objective function
F	Flux term
g	Acceleration of gravity, m/s^2
g	Temperature profile, ^{o}F

G	Sensitivity matrix
H	Specific enthalpy, J/kg
H	Hessian matrix
h	Heat transfer coefficient, W/m²·K
h_l	Heat transfer coefficient, W/m²·K
J	Jacobian matrix
j	Mixture volumetric flux, m/s
k	Intrinsic permeability, m²
k_f	Fracture permeability, md
k_r	Relative permeability
k_{rw}	Relative permeability of the wetting phase
k_{rnw}	Relative permeability of the nonwetting phase
N_{Re}	Reynold's number
n	Number of moles
p	Pressure, Pa
p_i	Initial pressure, psi
q	Phase mass flux per cell, kg/m³·s
Q_{wb}	Heat transfer rate per unit volume, J/m³·s
R	Wellbore radius, m
R	Residual vector
R	Universal gas constant, 8.31 J/mol·K
R_s	Solution gas-oil ratio

r_o	Equivalent wellbore radius, m
r_w	Wellbore radius, m
S	Saturation
S_{iw}	Wetting-phase irreducible saturation
S_w	Wetting-phase saturation
S_{wn}	Normalized wetting-phase saturation
s	Skin factor
T	Temperature, K
T_{fr}	Temperature inside the fracture, K
T_{init}	Initial reservoir temperature, K
T_{inj}	Injection fluid temperature, K
T_{res}	Reservoir sandface temperature, K
T_{wf}	Wellbore fluid temperature, K
u	Volumetric flux vector, m/s
u_{fr}	Fracturing fluid velocity inside the fracture along the direction of fracture propagation, m/s
U	Specific internal energy, J/kg
U_T	Overall heat transfer coefficient, $W/m^2 \cdot K$
V	Volume of gas at a specified temperature and pressure
V_b	Volume of the grid that contains the wellbore, m^3
V_d	Drift velocity of the gas, m/s
V_{ijk}	Cell volume, m^3
v	Fluid in-situ velocity, m/s

w	Fracture width, m
w	Derivative vector
WI	Well index
x_f	Fracture half-length, ft
x_{root}	Root
x_m	Inversion parameters
x_{mi}	Initial guess of the inversion parameters
y	Volumetric friction
z	Gas deviation factor

Greek

β	Thermal expansion coefficient, 1/K
γ	Pipe open ratio
γ_g	Specific gas gravity
ε	Convergence criteria
λ	Damping factor
λ_f	Fluid thermal conductivity, W/m·K
λ_T	Total thermal conductivity, W/m·K
μ	Viscosity, Pa·s
ρ	Density, kg/m^3
ρ_l	Fluid density, kg/m^3
ϕ	Formation porosity

Subscripts

c	Phase, can be gas, oil or water
c	Casing
cal	Calculated
cem	Cement
con	Continuous phase
dis	Dispersed phase
f	Cell face index
g	Gas
I	Inflow/outflow fluid
i	Inner
inv	Inversion point
l	Liquid
m	Mixture mean value
o	Oil
o	Outer
obs	Observed
pc	Pseudocritical
pr	Pseudoreduced
R	Reservoir
r	Rock
ref	Reference condition

sc	Standard condition
w	Water
y	Y-direction
z	Z-direction
θ	Thermal

TABLE OF CONTENTS

LIST OF FIGURES

xvii

xviii

LIST OF TABLES

CHAPTER I

INTRODUCTION

1.1 Background

The unconventional oil and gas resources are widespread throughout the United States (EIA 2016) and the world (West Virginia GIS Technical Center 2014), and hydraulic fracturing with horizontal drilling is the critical practice to produce from these shale reservoirs. Tremendous studies have been performed to better understand the fracture growth (Tang and Wu 2018; Tang et al. 2018a; Tang et al. 2018b), the fracture interference and network (Huang et al. 2016; Yang et al. 2018), and enhanced oil recovery technologies for unconventional reservoirs (Zhang et al. 2018a; Zhang et al. 2018b). The ideal outcomes of multistage hydraulic fracturing in horizontal wells are to create a controlled fracture distribution along the horizontal well that provides maximum production after stimulation (Tang et al. 2019; Xie et al. 2018). Such goal promotes different methods of fracture monitoring and diagnosis (Roberts et al. 2018; Xue et al. 2018; Yang et al. 2016). Nowadays, the hydraulic fracturing treatment is moving towards a reduced cluster spacing and more complex fracture network, which makes fracture diagnosis an even more challenging task.

Downhole temperature monitoring, as one of the downhole diagnosis tools, has been successfully applied in the field in many different aspects for years. Downhole temperature measurements are mainly from the temperature logs as a part of production logging tools (PLT), and distributed temperature sensing (DTS) from fiber optic sensors.

In recent years, downhole temperature monitoring has new applications in the field for fracture diagnosis during injection, shut-in and production periods, and supports the hydraulic fracturing design. At the same time, temperature models are improved continuously by many researchers. However, there are still many challenges in the interpretation of downhole temperature measurements, especially quantitative interpretation. These challenges include: the uncertainties of the parameters ranging from reservoir properties, well completion, to fracture geometry; the needs of a fast and robust forward model to simulate temperature behavior from injection, shut-in to production period accurately and efficiently; and the needs of an inversion methodology that can converge fast, reduce the uncertainties and lead to a practically meaningful solution. Under the motivation to conquer these challenges, this study conducts a systematic investigation on quantitative interpretation of the downhole temperature measurements.

1.2 Literature Review

1.2.1 Downhole Temperature Measurements

Downhole temperature is commonly measured by temperature logs which are part of the production logging tool package, or fiber optic sensors. Temperature logging was first introduced to the petroleum industry in the 1930s (Whittaker 2013). Figure 1.1 shows a typical production logging tool, which integrates the spinner flow meter, pressure and temperature sensors, and other sensors (Davarpanah et al. 2017). The typical temperature sensor on the production logging tool is a platinum resistance temperature detector with an accuracy of ± 1 $^{\circ}$C and a resolution of 0.006 $^{\circ}$C (Whittaker 2013). The production

logging tool is usually running inside the wellbore and can measure the temperature spatially along the wellbore at the running time.

Figure 1.1 Typical production logging tool (reprinted from (Davarpanah et al. 2017))

From the production logging tool, the flow rate along the wellbore can be obtained from either spinner flow meter or the quantitative interpretation of temperature logs (Hill 1990). A spinner flow meter is used to measure the fluid velocity so that the flow rate profile for single-phase flow and multi-phase flow can be obtained. However, according to Hill (1990) and Liao (2013), the spinner flow meters have some problems in the following aspects:

(1) The spinner flow meter is susceptible to mechanical problems and the quality of the log depends strongly on the care taken in running the log. This care includes: a constant and sufficient flow rate is required while running the log; spinner flowmeter interpretation is based on a constant wellbore cross-section area; the production must be free of sand.

(2) In highly deviated and horizontal wells with multiphase flow, downhole flow regimes can be complex and can include stratification, misting and recirculation. Spinner flow meter can misinterpret the flow rate profile due to this non-uniform phase distribution at the wellbore cross-section.

On the other hand, according to Hill (1990), temperature logs can measure temperature accurately no matter what the wellbore flow conditions are. Also, the temperature log tends to reflect the long-term behavior of a well. However, to obtain flow rate profile from temperature logs is an interpretation process which relies on an understanding of the fluid flow and heat transfer in and around the wellbore.

In recent years, fiber optic cables have become a popular technology which measures real-time temperature continuously along a wellbore, thus referred to as Distributed Temperature Sensor (DTS). Fiber optic cables can be installed outside the casing or inside the wellbore. It also can be a permanent measurement or temporary measurement (Halliburton.com 2019). When used as a temporary measurement, it is usually run through coil tubing which is inside the wellbore. There are also other practices to convey fiber optic cable, such as through a carbon rod for temporary measurement (Attia et al. 2019). When a fiber optic cable is installed outside the casing, with good cementing, the measured temperature will reflect the reservoir temperature since it is influenced less by the fluid mixture inside the wellbore. When permanently installed, the fiber optic cable can measure the temperature for the entire life of a well, during completion, during hydraulic fracturing, shut-in, and production. Figure 1.2 shows a standard deployment of fiber optic cables. Currently, the most common fiber optic cables have a temperature resolution of 0.01 $^{\circ}$C with a spatial resolution about 1 m (Halliburton.com 2019).
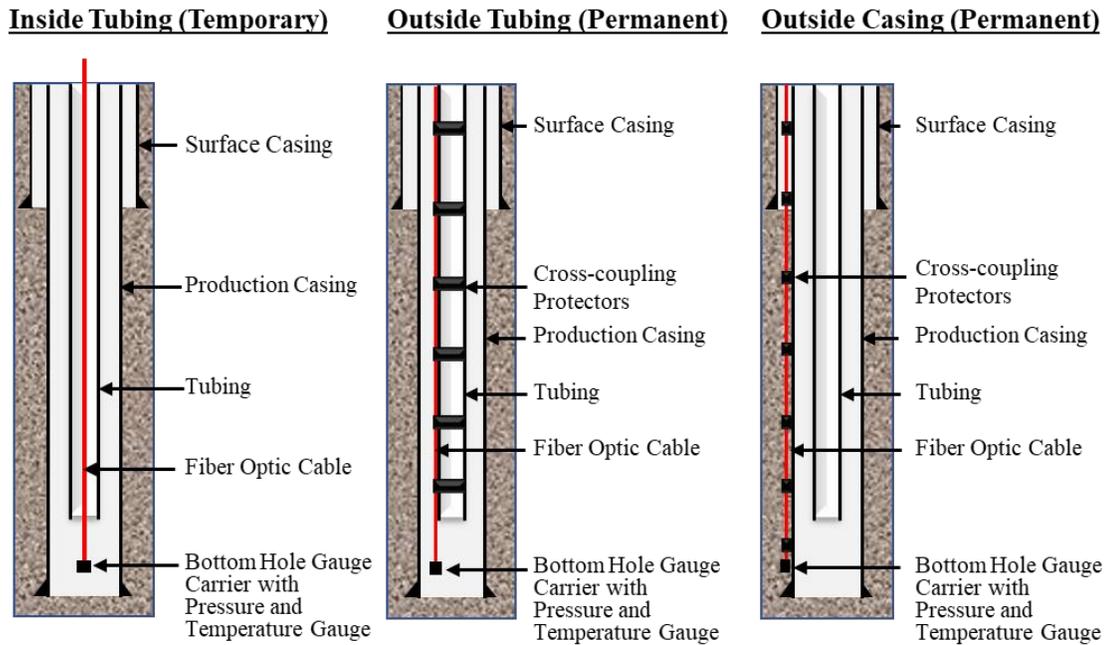
Figure 1.2 Common deployment of fiber optic cable

Fiber-optic distributed temperature measurement uses an industrial laser to launch bursts of light down the optical fiber. During the passage of each package of light, a small amount is backscattered from molecules in the fiber. This backscattered light can be used to estimate the temperature along the fiber. Figure 1.3 shows the frequency response of the back-scattered signal. The amplitudes of the Stokes Raman and anti-Stokes Raman signals are collected and averaged. A characteristic of each spectrum of backscattered light is that the ratio of the Stokes Raman bands to the anti-Stokes Raman bands is directly proportional to the temperature at the location where the backscatter is generated. Consequently, a log of temperature can be calculated every meter along the whole length of the fiber by using only the laser source, analyzer, and a reference temperature in the surface system (Schlumberger 2009).
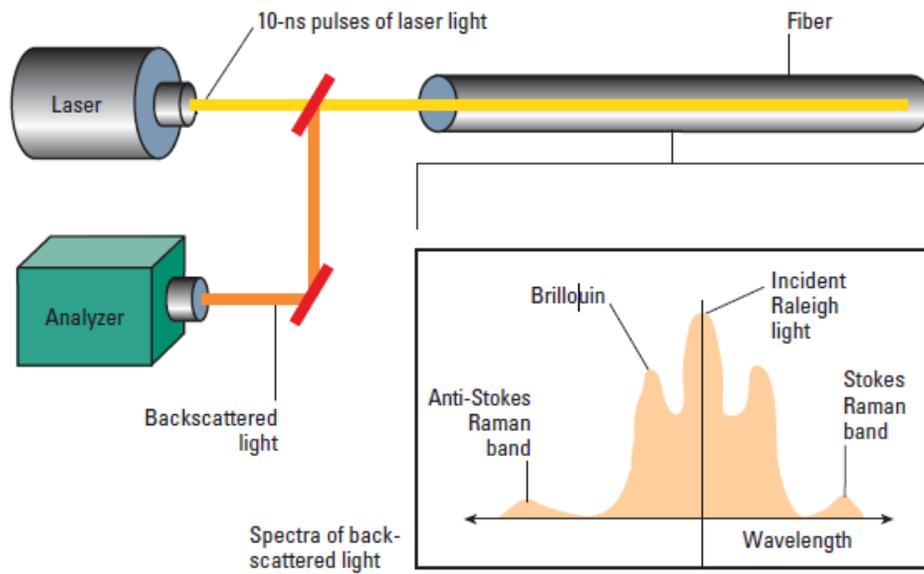
Figure 1.3 Distributed temperature measurement (reprinted from (Schlumberger 2009))

1.2.2 Field Applications of Downhole Temperature Measurements

Downhole temperature measurements have been applied in the field for years. The applications of the temperature measurements from the production logging tools have shown successful results in locating cement tops (Peacock 1965), detecting casing leaks and fluid movement behind casing, estimating fracturing fluid profile (Aslanyan et al. 2013), interpreting fracture height (Davis et al. 1997) and detecting gas/oil entry from productive intervals (Li and Zhu 2010). It has also been applied to the flow rate profiling in gas-producing horizontal wells with multiple transverse fractures (Cui et al. 2016a). The applications of temperature interpretation for gas-producing wells during production period show promising results. The strong Joule-Thomson effect of gas flow makes temperature interpretation viable for flow profiling.

For recent years, there is a great increase in the deployment and applications of the fiber optics sensors. The early-time installation of the fiber optic sensors can be traced back to 1993 when Shell installed their first in-well fiber optic system in the Sleen field in the Netherlands (Kragas et al. 2001). After that, DTS had many different applications. DTS was used to evaluate the matrix acidizing treatment (Al-Najim et al. 2012; Tardy et al. 2012). It was also applied to monitor the steam injection in horizontal injectors for heavy oil fields, providing the quantitative steam injection flow profile (Shirdel et al. 2016), and identifying the steam breakthrough zones (Gonzalez et al. 2018). DTS data analytics was used for real-time anomaly detection in gas-lift well operations, including monitoring the gas lift valves performance and raising alarms (Bello et al. 2018).

Recent years, due to the dramatically increasing practice of hydraulic fracturing, there are more applications of DTS measurement for fracture stimulation diagnosis. DTS is often deployed together with Distributed Acoustic Sensors (DAS), the combined application of DTS and DAS provide more confidence in fracture diagnosis.

During hydraulic fracturing treatments and well shut-in periods after pumping, the DTS technology can be used to estimate fracture initiation location. Sierra et al. (2008) showed the field example for such an application. They also pointed out that the location of fiber optic sensors, either inside the flow path or behind casing, has a significant impact on the temperature response. Ugueto et al. (2015) showed, in their DTS waterfall maps for multi-stage fracturing stimulation, the 'stair-step' temperature distribution shows effective zonal isolations. Ugueto et al. (2016) further discussed perforation cluster efficiency in the cemented plug-and-perf completions investigating the DTS and the DAS responses during

fracturing treatment, shut-in and production period. Comparing the DTS and DAS responses during injection and production, they concluded, while all perforations received the injected fluid, only half or two-thirds of the perforation clusters are properly stimulated or produced at significant rates. In 2018, DTS, together with DAS, and pressure and temperature gauges, has been applied to monitor the performance of another type of completion - cemented single point entry system well (Ugueto et al. 2018a). The fiber optic cable was deployed through coil tubing. The purpose was to diagnose the entry-to-entry isolation quality in the wellbore. The result from the pressure/temperature gauges, DTS and DAS, are consistent for most of the stages. According to the analysis result of stage communication, they estimated that several hundred thousand US$ were wasted from the misplacement of stimulation energy and materials. DTS and DAS measurements have also been used to monitor the cross-well communication during hydraulic fracturing (Sahdev and Cook 2016). Both DTS and DAS observed large cross-well communication events through the treatment.

Another recent application of DTS is evaluating refracturing effectiveness using warmback temperature data (Attia et al. 2019), which takes the guesswork out of refracturing and is a method for understanding how effective the refracturing designs performed.

During the production of horizontal wells with multiple fractures, DTS shows real-time production profiling for single-phase gas production. Menkhaus et al. (2012) illustrated a multi-well logging campaign in the Marcellus shale, which highlights the

benefits of fiber optic technology as a suitable alternative to traditional production logging.

The above-mentioned field applications have shown the effectiveness and advantages of using DTS and DAS in the diagnosis of the hydraulic fracturing. Ugueto et al. (2018b) and Natareno et al. (2019) have both shown their applications of the continuously monitoring of a well using fiber optics to accelerate stimulation optimization. Ugueto et al. (2018b) stated that the traditional approach of industry towards the stimulation optimization is to use "trial" wells with new technologies to compare with several "reference" wells. This approach takes several years and more wells, and can be over-capitalized to determine the optimum completion. Ugueto et al. (2018b) pointed out that the new approach of using fiber optic monitoring allows the test of different completion technologies on the same well which can accelerate the completion optimization and reduce over-capitalization risk. Also, according to Natareno et al. (2019), with fiber optic sensors, completion design evaluation time changed from about 6 months historically to 1 month. Temperature diagnosis of multistage fracturing provides us with guidelines on further field development such as infill well drilling and refracturing (Huang et al. 2016).

1.2.3 Temperature Modeling

Together with the development of downhole temperature measurements application, quantitative temperature models were also developed. Many researchers have contributed to different temperature models including wellbore models, reservoir models,

wellbore/reservoir coupled models for vertical wells and horizontal wells, wellbore/reservoir coupled models for fractured vertical wells, and models for horizontal wells with multiple transverse fractures in different periods - during injection, shut-in, and production.

The early-time wellbore thermal model developed by Ramey (1962) predicts the temperature of fluids, tubing, and casing as a function of depth and time by assuming steady-state heat transfer in the wellbore and unsteady radial conduction to the earth.

App and Yoshioka (2013) developed a reservoir temperature model for single-phase flow and both for the steady-state and transient state. This model was applied to evaluate the impact of reservoir permeability on sandface temperature.

For the wellbore/reservoir coupled model for vertical wells, Hasan et al. (1997) developed the model to study the temperature behavior of a single-phase oil flow in the wellbore. The wellbore model was solved numerically while the reservoir model was solved analytically. Xu et al. (2018) extended the previous model for single-phase gas flow while considering the Joule-Thomson effect and the dependence of gas properties on temperature and pressure. The reservoir part was solved semi-analytically.

For the wellbore/reservoir coupled models for horizontal wells, Yoshioka et al. (2007) proposed a steady-state wellbore temperature model. Since the geothermal temperature change is small for horizontal wells, this model considered the subtle thermal effects caused by thermal expansion. They used the model to predict the temperature change in a deviated horizontal well, detection of water or gas entry in the horizontal direction and the vertical direction (water coning). Li and Zhu (2010) developed a transient

10

reservoir/wellbore model that solves the coupled pressure distribution and temperature distribution. Their work successfully captured the transient behavior of temperature along horizontal wells for a water coning case and a water injection case from the adjacent horizontal well. Duru and Horne (2010) presented a transient pressure and temperature model for both single-phase and multi-phase flow.

Temperature models for hydraulic fractured wells were also developed. Harrington et al. (1978) presented an analytical solution to predict the formation and stimulation fluid heat-up once the well has been shut-in after stimulation. It only considered one-dimensional linear heat flow. Biot et al. (1987) provided a theoretical method to determine the fracturing fluid temperature as a function of time and location during fracture growth. Meyer (1989) presented an analytical model which coupled the energy equation and the fracture propagation equation. Kamphuis et al. (1993) used the finite-difference method to compute the temperature profiles in a propagating fracture. Their work showed different temperature behavior due to different fracture geometry. Davis et al. (1997) developed a mathematical model to simulate the wellbore temperature after fracturing for cases where the wellbore and fracture are not coincident for the entire extent of the fracture, and this model was applied to interpret the fracture height. Seth et al. (2010) presented a numerical model for interpretation of DTS data during fracturing treatment and shut-in period associated with fracture propagation model based on a simple volume balance. Hoang et al. (2012) developed a radial model for temperature simulation which was still capturing the fluid-flow and heat-transport of the fracture propagation for limited-entry fracturing.

The models mentioned above were mainly applied for hydraulic fracturing in vertical wells.

Meanwhile, temperature models were also developed for horizontal wells with multiple transverse fractures in different periods - during injection, shut-in, and production. Tabatabaei and Zhu (2012) showed the study of the temperature during injection and warm-up periods by considering the effects of injection rate allocation on wellbore temperature profile. Ribeiro and Horne (2013) discussed pressure and temperature behavior inside fracture during stimulation and shut-in (fracture closure) period, and then further extended their model to consider the effect of fracture growth and closure, as well as the well effects and interaction between multiple fractures (Ribeiro and Horne 2014). Li and Zhu (2016) proposed a model for horizontal well during fracture treatments. In this model, the propagation of the fracture and fluid leak-off into the formation were considered. During the production of multi-stage hydraulic fracture horizontal well, a semi-analytical model was developed to predict single-phase temperature behavior and was applied for several field cases to quantitatively estimate inflow rate profiles (Cui et al. 2016a). Fast Marching simulation technique later was adopted to improve the computation efficiency (Cui et al. 2016b). A fully numerical flow and thermal model for the multi-stage fractured horizontal wells was presented by Yoshida et al. (2018), serving as a validation tool to analytical/semi-analytical models. Among the production models for fractured horizontal wells, the semi-analytical model (Cui et al. 2016a) has a fast computation speed but can only handle single-phase flow and homogenous reservoirs, while the fully numerical compositional model (Yoshida et al.

2018) can handle the multi-phase flow and heterogeneous formations but with low computational efficiency. For further application of the thermal models to temperature interpretation, the compromise between the computational efficiency and the model robustness is necessary.

1.2.4 Inversion Algorithms

The temperature models mentioned above are useful to calculate temperature behavior based on known properties such as reservoir properties, fracture properties, and well structure. However, in order to quantitatively interpret the measured temperature to a flow rate profile, we need an inversion model to invert the unknown properties from the measured temperature and then generate the flow rate profile.

The inverse problem is defined in contrast to the forward problem. From a complete description of a physical system to predict the outcome of some measurements is called a forward problem. The inverse problem consists of using the actual result of some measurements to infer the values of the parameters that characterize the system (Tarantola 2005). In our case, the temperature interpretation is a nonlinear inverse problem which results in massive complexity.

There are some inversion algorithms using iterations to assist the updates of inversion parameters. These algorithms are usually rooted in the inversion theory to minimize the appropriately defined objection function to obtain the match between simulation results with the measured data. The commonly used inversion algorithms include gradient-based methods, such as Gradient Descent (Ruder 2016), Gauss-Newton

(Hartley 1961) and Levenberg-Marquart (Oliver et al. 2008); and stochastic algorithms, such as Markov Chain Monte Carlo (Ma et al. 2008), Simulated Annealing (Van Laarhoven and Aarts 1987), Ensemble Kalman Filter (Oliver et al. 2008) and Genetic Algorithm (Holland 1992). The gradient-based method usually starts from a single initial value. It requires the computation of the sensitivity matrix to update the parameter vector. It needs a smaller number of iterations to minimize the objective function compared to the stochastic methods while it possibly falls into the so-called 'local minimum' due to the non-linearity of the solution space. On the other hand, the stochastic algorithms usually can avoid the problem of convergence to local optimum nearest to the initial starting point. However, these methods often require a large number of forward simulations, which can be computationally expensive, especially when the parameter space is enormous.

1.3 Objective and Organization of the Dissertation

According to the current research, the interpretation of downhole temperature measurement for multi-stage hydraulic fractured horizontal wells still has the following problems to solve. First, it is essential to have a temperature model that compromise both robustness and computational efficiency. This model should be able to handle more complex situations compared to the semi-analytical model (Cui et al. 2016a), for example, multiphase flow for different periods – injection, shut-in, and production. Meanwhile, the model should be more efficient than the fully-numerical compositional model (Yoshida et al. 2018). Second, an efficient inversion procedure is the key to practical application of downhole temperature sensing. This procedure needs to be able to converge fast, reduce

the uncertainties maximumly, and lead to a sensible solution. Third, for more generalized applications, the inversion procedure should also be capable of interpreting temperature measurements both from PLT and DTS considering different sensor locations and be flexible to adjust to interpret both liquid flow and gas flow. Consequently, this work is performed to solve these problems.

In this work, a black-oil thermal model is first developed to simulate the transient temperature behavior during hydraulic fracturing treatment, shut-in, and well production. Chapter 2 presents the details of the model development, including the mathematical equations, the numerical solution for the governing equations, and the model validation. Chapter 2 also discusses the advantages and limitations of the developed model, and how to apply this model to its full advantages. Chapter 3 proposes the general temperature interpretation procedure which consists of the measured data pre-processing, initial evaluation, local temperature matching, and global re-examination. A sensitivity study is performed to determine the most influential parameters. The interpretation procedure is tested by a synthetic example and shows both effectiveness and efficiency. Chapter 4 shows the application of this interpretation procedure to single-phase gas producing horizontal wells with multiple fractures. A field example is presented to illustrate the process of using the developed method. In Chapter 5, the developed procedure is applied to a two-phase water/oil producing horizontal well with multiple fractures. The interpretation of temperature for two-phase liquid producing well is a more complex problem compare to the single-phase gas producing well problem. This chapter discusses how to adjust the developed general interpretation procedure to solve the additional

complexity induced by the two-phase liquid flow with reasonable assumptions, and how to analyze the temperature measurement at the beginning to avoid misinterpretation. Eventually, Chapter 6 summarizes the conclusions from this study.

CHAPTER II

BLACK OIL THERMAL MODEL

2.1 Introduction

Downhole temperature measurements are usually obtained from production logging tools or fiber optic cables. For permanently installed fiber optic cables, the distributed temperature can be measured from the treatment of hydraulic fracturing to shut-in and well production. There are many reservoir simulation models have been developed to simulate the pressure and flow distribution ranging from theoretical models (Deng and King 2018, 2019) to comprehensive numerical models involved fracture networks and geomechanics (Chen et al. 2018; Xue et al. 2019a; Xue et al. 2019b). To quantitatively interpret the downhole temperature measurement, we need an integrated flow and thermal model that can not only simulate the pressure and flow profile but also temperature profile simultaneously. This model needs to be able to simulate the multiphase flow and transient temperature behavior during fluid injection, shut-in, and production. Meanwhile, for further application of the model in temperature interpretation the model needs to have reasonable computational efficiency while maintaining the maximum accuracy that can be achieved. Consequently, a black oil thermal model is developed to meet these requirements.

In this chapter, a detailed description of the multiphase black-oil thermal model is presented.

2.2 Model Description

The integrated multiphase black-oil thermal and flow model can simulate the transient temperature behavior during the fluid injection, shut-in, and the production for multi-stage hydraulic fractured horizontal wells. The model consists of two sub-models: the reservoir model and the wellbore model (Figure 2.1). Both sub-models solve the flow problem through mass and momentum balance equations for pressure and velocity in the simulation domain, and thermal problem through energy balance equation for the temperature distribution in the flow field.
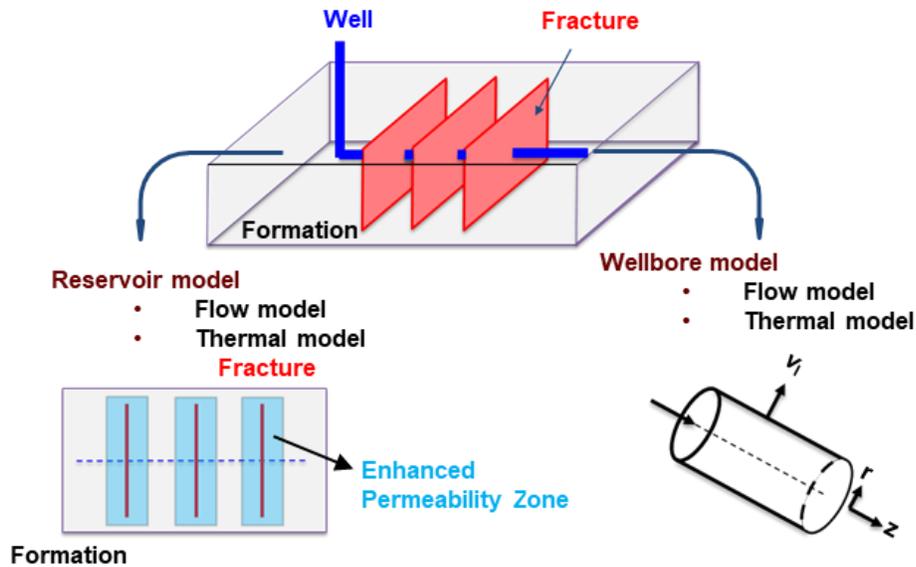
Figure 2.1 Model description

2.2.1 Reservoir Model

The reservoir model contains the formation, the enhanced permeability zone, and the fracture. The reservoir model is formulated in three dimensions. By assuming a

symmetric geometry, the simulation domain can be reduced as shown in Figure 2.2. This method can reduce the computational time. Also, we assume that the fluid and matrix are in thermal equilibrium locally and ignore the capillary pressure. To simplify the problem, we adopt a black-oil fluid model (Ertekin et al. 2001). In black-oil fluid model, there are three phases (oil phase, water phase, and gas phase), and three fluid components (oil component, water component, and gas component). Figure 2.3 shows the distribution of the components among phases in the black-oil fluid. The oil and water components are assumed to be immiscible, and therefore there is no mass transfer between the oil and water phases. The gas component is assumed to be soluble in oil phase but not in water phase. Therefore, there is mass transfer of the gas component between gas phase and oil phase.
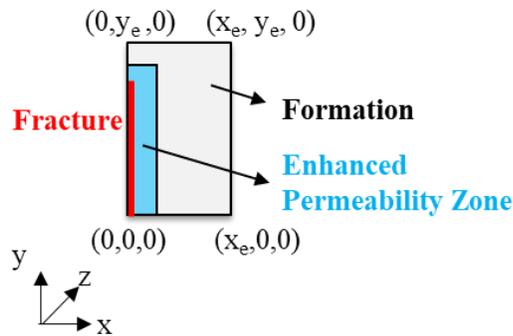
Figure 2.2 Reservoir model simulation domain (top view)

Figure 2.3 Distribution of components among phases in black-oil fluid (redrawn from (Ertekin et al. 2001))

19

Because of the mass transfer between oil and gas phases, mass is not conserved within each phase, but the total mass of each component must be conserved. The component mass balance equations are as the following.

For the oil component:

$$\frac{\partial}{\partial t}(\phi c_{Oo}\rho_o S_o) + \nabla \cdot (c_{Oo}\rho_o \boldsymbol{u}_o) = c_{Oo}q_o \tag{2.1}$$

For the water component:

$$\frac{\partial}{\partial t}(\phi \rho_w S_w) + \nabla \cdot (\rho_w \boldsymbol{u}_w) = q_w \tag{2.2}$$

For the gas component:

$$\frac{\partial}{\partial t}(\phi \rho_g S_g + \phi c_{Go}\rho_o S_o) + \nabla \cdot (\rho_g \boldsymbol{u}_g + c_{Go}\rho_o \boldsymbol{u}_o) = (q_g + c_{Go}q_o) \tag{2.3}$$

In the above equations, the subscripts o, w, and g denote oil, water, and gas phase respectively; ϕ is the formation porosity, ρ is the density, S is the saturation, $\boldsymbol{u}$ is the volumetric flux vector, q is the phase mass flux per cell volume; c_{Go} is the mass fraction of dissolved gas in the oil phase, and c_{Oo} is the mass fraction of oil component in the oil phase, which can be calculated from solution gas-oil ratio R_s based on the following equations.

$$c_{Go} = \frac{R_s \rho_{Gsc}}{B_o \rho_o} \tag{2.4}$$

$$c_{Oo} = \frac{\rho_{Osc}}{B_o \rho_o} \tag{2.5}$$

in which the subscript sc denote the standard condition, ρ_{Gsc} and ρ_{Osc} are the density of gas component and oil component at the standard condition, and B is the formation volume factor. The solution gas-oil ratio R_s, the formation volume factor B and the density of oil

phase ρ_o depend on the pressure and temperature, which will be discussed in detail in Section 2.2.4.

In Equations 2.1 to 2.3, the first term on the left-hand-side denotes the mass accumulation, the second term on the left-hand-side denotes the mass flux, the term on the right-hand-side is the mass source/sink. The source/sink term is nonzero only at the interaction between the wellbore and the reservoir, and this term denotes the fluid exchange between these two domains.

We use Darcy's law to calculate the volumetric flux vector.

$$\boldsymbol{u}_c = -\frac{kk_{rc}}{\mu_c}(\nabla p_c - \rho_c \boldsymbol{g}) \qquad (2.6)$$

where the subscript c denotes the phase, it can be gas, oil or water; k is the intrinsic permeability, k_{rc} is the relative permeability of phase c, μ_c is the viscosity of phase c, p_c is the pressure in phase c, and $\boldsymbol{g}$ is the acceleration of gravity.

The energy balance equation is expressed as:

$$\frac{\partial}{\partial t}\left[\phi \sum_c \rho_c S_c U_c + (1-\phi)\rho_r U_r\right] + \nabla \cdot \left[\sum_c \rho_c H_c \boldsymbol{u}_c - \lambda_T \nabla T\right] = \sum_c H_c q_c + Q_{wb}$$

$$(2.7)$$

in which the subscript r denotes the rock, U is the specific internal energy, H is the specific enthalpy, λ_T is the total thermal conductivity, T is the temperature. Q_{wb} is the heat conduction rate per unit volume between the wellbore and the reservoir. $\sum_c H_c q_c$ denotes the heat convection due to the flow between the reservoir and wellbore.

Similar to the mass balance equation, in Equation 2.7 the first and second terms on the left-hand-side are the heat accumulation, heat convection, and conduction respectively. The two terms on the right-hand-side are the heat source/sink term. $\sum_c H_c q_c$, which denotes

21

the heat convection, is only nonzero when there is a fluid flow between the reservoir and wellbore, for example, at the perforation locations. Q_{wb}, which is the heat conduction rate per unit volume between the wellbore and the reservoir, is nonzero when the reservoir grid contains the wellbore grid, both at the perforation locations and non-perforation locations.

In addition to the basic equations, there are two constraints. The saturation constraint is:

$$S_w + S_o + S_g = 1 \tag{2.8}$$

The mass fraction constraint is:

$$c_{Go} + c_{Oo} = 1 \tag{2.9}$$

The outer boundary of the formation is using the Neumann boundary condition with zero mass and heat flux.

$$\frac{\partial p}{\partial x}\Big|_{x=x_e} = 0 \tag{2.10}$$

$$\frac{\partial T}{\partial x}\Big|_{x=x_e} = 0 \tag{2.11}$$

$$\frac{\partial p}{\partial y}\Big|_{y=y_e} = 0 \tag{2.12}$$

$$\frac{\partial T}{\partial y}\Big|_{y=y_e} = 0 \tag{2.13}$$

$$\frac{\partial p}{\partial z}\Big|_{z=z_e} = 0 \tag{2.14}$$

$$\frac{\partial T}{\partial y}\Big|_{z=z_e} = 0 \tag{2.15}$$

At the symmetry axis where x equals to 0, the Neumann boundary condition with zero mass and heat flux is also used due to the symmetric geometry. The equation for the boundary condition is expressed as:

$$\frac{\partial p}{\partial x}\Big|_{x=0} = 0 \tag{2.16}$$

$$\frac{\partial T}{\partial x}\Big|_{x=0} = 0 \tag{2.17}$$

At the interface between the reservoir and wellbore, we use the wellbore solution as the boundary condition for the reservoir model.

2.2.2 Wellbore Model

The wellbore model developed by Yoshioka (2007) is adopted in this work and further extended to the transient condition. The same black-oil fluid assumption is kept for the wellbore model. The schematic graph of the coordinate system is shown in Figure 2.1.

The mass balance equations are as the following.

For oil:

$$\frac{\partial}{\partial t}(\rho_o y_o c_{Oo}) + \frac{\partial}{\partial z}(\rho_o y_o c_{Oo} v_o) = -\frac{2\gamma}{R}(\rho_{o,I} y_{o,I} c_{Oo,I} v_{o,I}) \tag{2.18}$$

For water:

$$\frac{\partial}{\partial t}(\rho_w y_w) + \frac{\partial}{\partial z}(\rho_w y_w v_w) = -\frac{2\gamma}{R}(\rho_{w,I} y_{w,I} v_{w,I}) \tag{2.19}$$

For gas:

$$\frac{\partial}{\partial t}(\rho_g y_g + \rho_o y_o c_{Go}) + \frac{\partial}{\partial z}(\rho_g y_g v_g + \rho_o y_o v_o c_{Go})$$

$$= -\frac{2\gamma}{R}(\rho_{g,I} y_{g,I} v_{g,I} + c_{Go,I} \rho_{o,I} y_{o,I} v_{o,I}) \tag{2.20}$$

in which y is the volumetric fraction, v is fluid in-situ velocity, R is the wellbore radius, the subscript I denotes the inflow/outflow fluid. γ is the pipe open ratio which is defined as the ratio of the open area of the pipe to the surface area of the pipe (Yoshioka 2007). In our numerical simulation, the grid block that contains the perforation has γ equal to one,

and the others have γ equal to zero. The terms on the right-hand side of Equations 2.18 to 2.20 denote the mass exchange between the reservoir and the wellbore.

The momentum equation which uses the phase-mixture average values is shown as the following.

$$\frac{\partial}{\partial t}\left(\sum_c y_c \rho_c v_c\right) + \frac{\partial p}{\partial z} + \frac{\partial}{\partial z}\left(\sum_c y_c \rho_c v_c v_c\right) = -\frac{1}{R}(\rho_m v_m |v_m| f_m) + \rho_m g_{m,z} \quad (2.21)$$

in which the subscript m denotes the mixture mean value, and f_m is the frictional factor of the mixture.

The frictional factor of the mixture f_m can be calculated using the mixture properties which include the following.

The mean density of the mixture ρ_m:

$$\rho_m = \sum_c y_c \rho_c \quad (2.22)$$

The mean velocity of the mixture v_m:

$$v_m = \frac{\sum_c y_c \rho_c v_c}{\sum_c y_c \rho_c} \quad (2.23)$$

The mean viscosity of the mixture μ_m takes account the phase inversion point (Jayawardena et al. 2000):

$$\mu_m = \mu_{con}(1 - y_{dis})^{-2.5} \quad (2.24)$$

There is an inversion point:

$$y_{inv} = \left[1 + \left(\frac{\mu_{con}}{\mu_{dis}}\right)^{\frac{1}{6}}\left(\frac{\rho_{con}}{\rho_{dis}}\right)^{\frac{5}{6}}\right]^{-1} \quad (2.25)$$

in which the subscript *inv* denotes the inversion point, the subscripts *dis* and *con* denote dispersed phase and continuous phase respectively.

24

Then the dimensionless number, Reynold's number N_{Re} used for calculating the frictional factor of the mixture is described as below.

$$N_{Re} = \frac{\rho_m v_m D}{\mu_m} \tag{2.26}$$

where D is the pipe inner diameter.

Then the frictional factor of the mixture f_m can be calculated from the following equations. In laminar flow,

$$f_m = \frac{16}{N_{Re}} \tag{2.27}$$

In turbulent flow, f_m can be calculated from Chen's correlation (1979).

$$\frac{1}{\sqrt{f_m}} = -4 \log \left\{ \frac{\varepsilon}{3.7065} - \frac{5.0452}{N_{Re}} \log \left[\frac{\varepsilon^{1.1098}}{2.8257} + \left(\frac{7.149}{N_{Re}} \right)^{0.8981} \right] \right\} \tag{2.28}$$

where ε is the relative pipe roughness.

The energy balance equation of the wellbore is:

$$\frac{\partial}{\partial t} \left(\sum_c y_c \rho_c \left(U_c + \frac{v_c^2}{2} \right) \right) = -\frac{\partial}{\partial z} \left[\sum_c y_c \rho_c v_c \left(H_c + \frac{v_c^2}{2} \right) \right] + \frac{\partial}{\partial z} \left(\lambda_f \frac{\partial T}{\partial z} \right)$$

$$- \frac{2\gamma}{R} \left[\sum_c y_{c,I} v_{c,I} \rho_{c,I} \left(H_{c,I} + \frac{v_{c,I}^2}{2} \right) \right] + \frac{2(1-\gamma)}{R} U_T (T_{res} - T)$$

$$+ \sum_c y_c \rho_c v_c g_{c,z} \tag{2.29}$$

in which λ_f is the fluid thermal conductivity, U_T is the overall heat transfer coefficient; T_{res} is the reservoir sand face temperature. The third and fourth terms on the right-hand side of Equation 2.29 denote the heat transfer between the reservoir and the wellbore due to heat convection and heat conduction respectively.

The solution of the model applies to oil/water two-phase flow and gas-liquid two-phase flow in the wellbore. For oil/water two-phase flow, a homogeneous model is employed. This model assumes the following:

$$v_o = v_w = j \tag{2.30}$$

where j is the mixture volumetric flux.

The gas-liquid two-phase flow could be either gas-water or gas-oil two-phase flow. A drift-flux model is used here, and the relationship between the fluid in-situ velocity and the mixture volumetric flux is given by Zuber and Findlay (1965).

$$v_g = C_o j + V_d \tag{2.31}$$

$$v_l = \frac{1-y_g C_o}{y_l}j - \frac{y_g}{y_l}V_d \tag{2.32}$$

where C_o is the distribution parameter to account for the non-uniform flow and the concentration profiles, V_d is the drift-velocity of gas, and these two parameters can be determined from experiments (Shi et al. 2005); the subscript l represents the liquid.

The three-phase water, oil and gas flow condition are not considered in this model.

2.2.3 Constitutive Relations

In the above two sections, we describe the governing equations which are used to solve the primary variables (pressure, temperature, and saturation). However, some other variables need to be calculated from the primary variables. These variables are called secondary variables, which are described by constitutive relations and equations of state. This section describes the main constitutive relations.

2.2.3.1 Relative Permeability

For multiphase flow, the relative permeability counts on the effective permeability of each phase. The relative permeability is a function of saturation. As discussed in the previous section, the solution of the model applies to oil/water, gas/water or gas/oil two-phase flow. Hence, Corey's two-phase model (1954) is adopted to compute relative permeability from saturation.

Corey's model is expressed as the following:

$$S_{wn} = \frac{S_w - S_{iw}}{1 - S_{iw}} \tag{2.33}$$

$$k_{rw} = S_{wn}^4 \tag{2.34}$$

$$k_{rnw} = (1 - S_{wn})^2 (1 - S_{wn}^2) \tag{2.35}$$

where S_{wn} is the normalized wetting-phase saturation, S_w and S_{iw} are the saturation and irreducible saturation of the wetting-phase, respectively, and k_{rw} and k_{rnw} are the relative permeability of the wetting and nonwetting phases respectively. The irreducible saturation S_{iw} can be determined from well logs or laboratory data.

2.2.3.2 Treatment of Source/Sink Terms

The mass balance equations in the reservoir model and wellbore model are coupled through the mass source/sink term (Equation 2.1 to 2.3). In the source/sink terms, the phase mass flux per cell volume q can be calculated as the following.

$$\boldsymbol{q}_c = WI \cdot \frac{k_{rc}\rho_c}{\mu_c}\left(p_{res} - p_{wf}\right) \tag{2.36}$$

in which the subscript c denotes phases including water, oil, and gas, WI is the well index which is calculated based on the Peaceman model (1993). The horizontal well is parallel to the x-direction.

$$WI = \frac{2\pi \bar{k} \Delta x}{\ln \frac{r_o}{r_w} + s} \tag{2.37}$$

where Δx is the length of the grid in x-direction which contains the wellbore, s is the skin factor, $\bar{k}$ is the average absolute permeability, and r_o is the equivalent wellbore radius. $\bar{k}$ and r_o can be obtained from the following equations.

$$\bar{k} = \sqrt{k_y k_z} \tag{2.38}$$

$$r_o = 0.28 \frac{\left[\left(\frac{k_z}{k_y} \right)^{\frac{1}{2}} (\Delta y)^2 + \left(\frac{k_y}{k_z} \right)^{\frac{1}{2}} (\Delta z)^2 \right]^{\frac{1}{2}}}{\left(\frac{k_z}{k_y} \right)^{\frac{1}{4}} + \left(\frac{k_y}{k_z} \right)^{\frac{1}{4}}} \tag{2.39}$$

in which the subscript y and z denote the y- and z-direction, Δy and Δz is the length of the grid in y-direction and z-direction which contains the wellbore.

Meanwhile, energy balance equations in the reservoir model and wellbore model are coupled through the heat source/sink term (Equation 2.7). The heat conduction rate per unit volume between the wellbore and the reservoir, Q_{wb} is computed by the following equation.

$$Q_{wb} V_b = A|_{r=r_w} U_T \left(T_{wf} - T_{res} \right) \tag{2.40}$$

where V_b is the volume of the grid that contains the wellbore, A is the surface area of the well segment, T_{wf} is the wellbore fluid temperature.

2.2.3.3 Overall Heat Transfer Coefficient

The overall heat transfer coefficient is used to calculate the heat transfer between the wellbore and the reservoir. Figure 2.4 shows the schematic plot for the near wellbore region, which includes the fluid, casing, cement, and formation rock. The overall heat transfer coefficient is a combined factor that counts on the heat convection inside the wellbore and the heat conduction through the casing and cement, which is given by:

$$\frac{1}{U_T|_{r=r_{ci}}} = r_{ci} \left[\frac{1}{r_{ci}h_{ci}} + \frac{\ln\frac{r_{co}}{r_{ci}}}{k_c} + \frac{\ln\frac{r_w}{r_{co}}}{k_{cem}} \right] \tag{2.41}$$

in which the subscripts c and cem are casing and cement respectively, the subscripts i and o denote the inner and outer, r_w is the wellbore radius, h is the heat transfer coefficient for forced convection is computed by Dittus-Boelter correlation (Dittus and Boelter 1930; Winterton 1998) as:

$$\frac{hd}{\lambda_f} = 0.023 \left(\frac{\rho v d}{\mu} \right)^{0.8} \left(\frac{\mu C_p}{k_f} \right)^n \tag{2.42}$$

in which d is the pipe inner diameter, λ_f is thermal conductivity of the fluid, ρ is the fluid density, v is the fluid velocity, μ is the fluid viscosity, C_p is the fluid specific heat capacity, n is 0.4 when the pipe temperature is higher than the fluid temperature, and 0.33 when fluid temperature is higher than the pipe temperature.
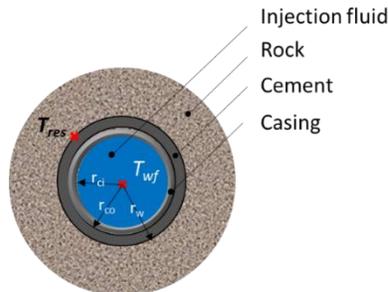
Figure 2.4 Near wellbore region

29

2.2.3.4 Specific Internal Energy and Specific Enthalpy

The fluid specific internal energy in the energy balance equations is calculated from the fluid specific enthalpy, phase pressure, and density.

$$U_c = H_c - \frac{p_c}{\rho_c} \tag{2.43}$$

The fluid specific enthalpy has the following relationship with the fluid temperature,

$$dH_c = C_{pc}dT + \frac{1}{\rho_c}(1 - \beta_c T)dp \tag{2.44}$$

where β is the thermal expansion coefficient.

2.2.4 Fluid and Rock Properties

In this section, the properties of fluid and rock which depend on the pressure and temperature are discussed in detail.

2.2.4.1 Dranchuk and Abou-Kassem Equation of State

The Dranchuk and Abou-Kassem Equation of State (1975) is based on the generalized Starling (1973) Equation of State and is expressed as:

$$z = 1 + \left(A_1 + \frac{A_2}{T_{pr}} + \frac{A_3}{T_{pr}^3} + \frac{A_4}{T_{pr}^4} + \frac{A_5}{T_{pr}^5}\right)\rho_{pr} + \left(A_6 + \frac{A_7}{T_{pr}} + \frac{A_8}{T_{pr}^2}\right)\rho_{pr}^2$$

$$- A_9\left(\frac{A_7}{T_{pr}} + \frac{A_8}{T_{pr}^2}\right)\rho_{pr}^5 + A_{10}\left(1 + A_{11}\rho_{pr}^2\right)\left(\frac{\rho_{pr}^2}{T_{pr}^3}\right) \times \exp\left(-A_{11}\rho_{pr}^2\right) \tag{2.45}$$

in which z is the gas-deviation factor, and the subscript *pr* stands for pseudoreduced.

The constants A_1 through A_{11} are shown in Table 2.1.

Table 2.1 The constants in Equation of State	
Constants	Value
A_1	0.3265
A_2	-1.0700
A_3	-0.5339
A_4	0.01569
A_5	-0.01565
A_6	0.5475
A_7	-0.7361
A_8	0.1844
A_9	0.1056
A_{10}	0.6134
A_{11}	0.7210

In Equation 2.45, the pseudoreduced properties are calculated from the pseudocritical properties (Towler 2002).

The pseudocritical pressure is calculated as:

$$p_{pc} = 756.8 - 131.07\gamma_g - 3.6\gamma_g^2 \tag{2.46}$$

and the pseudocritical temperature is calculated as:

$$T_{pc} = 169.2 + 349.5\gamma_g - 74.0\gamma_g^2 \tag{2.47}$$

in which the subscript *pc* represents pseudocritical, and γ_g is the specific gas gravities. Equations 2.46 to 2.47 are valid over $0.57 < \gamma_g < 1.68$.

With these two equations, the pseudoreduced pressure and pseudoreduced temperature are calculated by

$$p_{pr} = \frac{p}{p_{pc}} \tag{2.48}$$

$$T_{pr} = \frac{T}{T_{pc}} \tag{2.49}$$

The pseudoreduced density is calculated using the following equation.

$$\rho_{pr} = \frac{0.27 p_{pr}}{z T_{pr}} \tag{2.50}$$

2.2.4.2 Formation Volume Factor

The formation volume factor B is defined as the ratio of the volume at the reservoir condition to the volume at the standard condition.

$$B = \frac{V_R}{V_{sc}} \tag{2.51}$$

in which the subscripts R and sc represent reservoir and standard condition, respectively.

For gas, according to the real gas law:

$$pV = znRT \tag{2.52}$$

where V is the volume of gas at a specified temperature and pressure, n is the number of moles, and R is the universal gas constant, the gas formation volume factor B_g is expressed as:

$$B_g = \frac{p_{sc} z T}{p z_{sc} T_{sc}} \tag{2.53}$$

For oil and water, the inverse of the formation volume factor is defined as:

$$b_c = \frac{1}{B_c} = b_{ref} \times \exp\left(c_c(p - p_{ref})\right) \times \exp\left(-\beta_c(T - T_{ref})\right) \tag{2.54}$$

in which b is the inverse of the formation volume factor B, c is the isothermal compressibility, and β is the thermal expansion coefficient, the subscript ref stands for the reference condition, and the subscript c is the phase which can be oil or water here.

2.2.4.3 Isothermal Compressibility

The isothermal compressibility is defined as

$$c_c = -\frac{1}{V_c}\left(\frac{\partial V_c}{\partial p}\right)_T \tag{2.55}$$

32

For gas, Equation 2.55 can be derived to:

$$c_g = \frac{1}{p} - \frac{1}{z}\left(\frac{\partial z}{\partial p}\right)_T \tag{2.56}$$

For oil, when the pressure is above bubble point, Equation 2.55 can be written in terms of formation volume factor B_o.

$$c_o = -\frac{1}{B_o}\left(\frac{\partial B_o}{\partial p}\right)_T \tag{2.57}$$

When the pressure is below the bubble point,

$$c_o = -\frac{1}{B_o}\left(\frac{\partial B_o}{\partial p}\right)_T + \frac{B_g}{B_o}\left(\frac{\partial R_s}{\partial p}\right)_T \tag{2.58}$$

For water, Equation 2.55 can be written in terms of formation volume factor B_w.

$$c_w = -\frac{1}{B_w}\left(\frac{\partial B_w}{\partial p}\right)_T \tag{2.59}$$

2.2.4.4 Thermal Expansion Coefficient

The thermal expansion coefficient is defined as

$$\beta = \frac{1}{V}\left(\frac{\partial V}{\partial T}\right)_p \tag{2.60}$$

For water and oil, this work assumes that the thermal expansion coefficients of water and oil are constant and independent of pressure and temperature.

For gas, the thermal expansion coefficient can be approximated with a small temperature disturbance.

$$\beta_g = \frac{1}{V}\left(\frac{\partial V}{\partial T}\right)_p = \frac{1}{z(p,T)T}\frac{z(p,T+\Delta T)(T+\Delta T)-z(p,T)T}{\Delta T} \tag{2.61}$$

where ΔT is the small temperature disturbance.

2.2.4.5 Solution-Gas/Oil Ratio

The solution-gas/oil ratio can be estimated by Vazquez and Beggs (1977) correlation at any pressure below the bubble point.

$$R_s = p^{C_2} C_1 \gamma_g \exp\left(\frac{C_3 \gamma_{o,API}}{T_R + 460}\right) \tag{2.62}$$

In this equation, the parameters use the field unit. T_R is the reservoir temperature in ºF, p is the pressure in psi, and R_s is the solution-gas/oil ration in scf/stb. The constants in Equation 2.62 are shown in Table 2.2.

Table 2.2 Constants for solution-gas/oil ratio correlation

	≤30 ºAPI	≥ 30 ºAPI
C_1	0.0362	0.0178
C_2	1.0937	1.187
C_3	25.7240	23.9310

2.2.4.6 Fluid Density at Downhole Condition

The fluid density at the downhole condition can be computed from the formation volume factor.

For gas and water phases, there is only one component in each phase, so the phase density of gas and water is

$$\rho_c = \rho_{sc} b_c = \rho_{sc}/B_c \tag{2.63}$$

in which the subscript *sc* stands for the standard condition, the subscript *c* represents for the phase which can be gas or water here, and the other parameters are under the reservoir condition.

For oil phase, there are oil component and dissolved gas component. The phase density of oil can be calculated from the following equation.

$$\rho_o = b_o \rho_{Osc} + R_s b_o \rho_{Gsc} = \frac{\rho_{Osc}}{B_o} + \frac{R_s \rho_{Gsc}}{B_o} \tag{2.64}$$

where ρ_{Gsc} and ρ_{Osc} are the density of gas component and oil component at the standard condition, and R_s is the solution gas-oil ratio.

2.2.4.7 Fluid Viscosity

This work uses the exponential model to calculate fluid viscosity.

$$\mu = \mu_{ref} \times \exp\left(\mu_p(p - p_{ref})\right) \times \exp\left(-\mu_T(T - T_{ref})\right) \tag{2.65}$$

where the subscript *ref* stands for the reference condition, μ_p and μ_T are the coefficients of the pressure dependency and temperature dependency which can be obtained from laboratory test.

2.2.4.8 Rock Porosity

This work assumes the rock is slightly compressible. Hence, the porosity of the rock is expressed as:

$$\phi = \phi_{ref} \times \left(1 + c_r(p - p_{ref})\right) \tag{2.66}$$

where c_r is the isothermal compressibility of the rock.

2.3 Numerical Solution of the Model

This section discusses the details of the numerical solution of this developed black-oil thermal model. The finite difference method is adopted to discretize the governing equations, and the fully-implicit scheme with Newton-Raphson algorithm is used to solve the governing equations. This section also described the solution procedure to couple the reservoir model with the wellbore model.

2.3.1 Gridding System for Numerical Solution

The developed black-oil thermal model is solved numerically. In the numerical simulation, the gridding system is critical for computational accuracy as well as computational efficiency. This section presents the gridding system of the reservoir and the wellbore.

As shown in Figure 2.1, the reservoir model contains the fracture, the enhanced permeability zone, and the formation. Due to symmetric geometry, the simulation domain can be reduced as shown in Figure 2.2. This reduced simulation domain is then discretized, as shown in Figure 2.5. In y and z-direction, the grids are meshed uniformly, while in x-direction the tartan grid is used. The fracture only contains one grid in the x-direction. The grid width in the x-direction is increasing geometrically when the grid is getting further from the fracture.
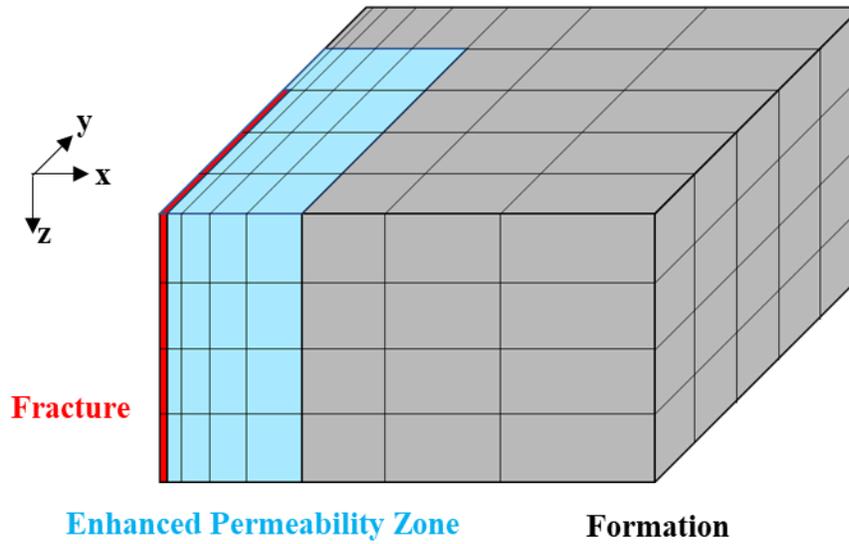
Figure 2.5 Gridding scheme for the reservoir model

The wellbore model is formulated in one dimension. For further coupling with the reservoir model, the width of the grids in the wellbore model is the same as their corresponding grids in the reservoir model. Hence, the grid width is also increasing geometrically when it is getting further from the fracture. Figure 2.6 shows the gridding scheme for the wellbore model. The red grid represents the part of the wellbore that contains the perforations, and this grid is coupled with the fracture grid. Its pipe open ratio γ equals to 1. The other grids represent the non-perforated region of the wellbore, whose pipe open ratio γ is 0. The coupling between the reservoir model and the wellbore model is shown in Figure 2.7. The mass exchange only happens at the perforation location.
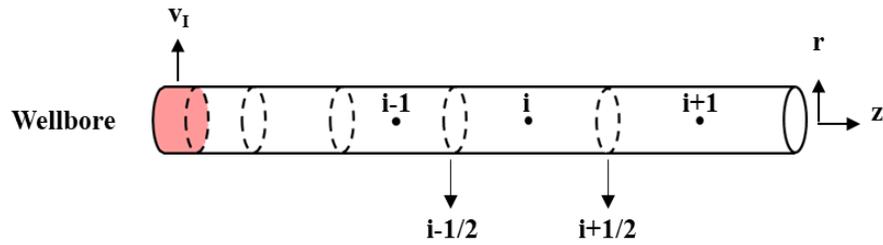
Figure 2.6 Gridding scheme for the wellbore model
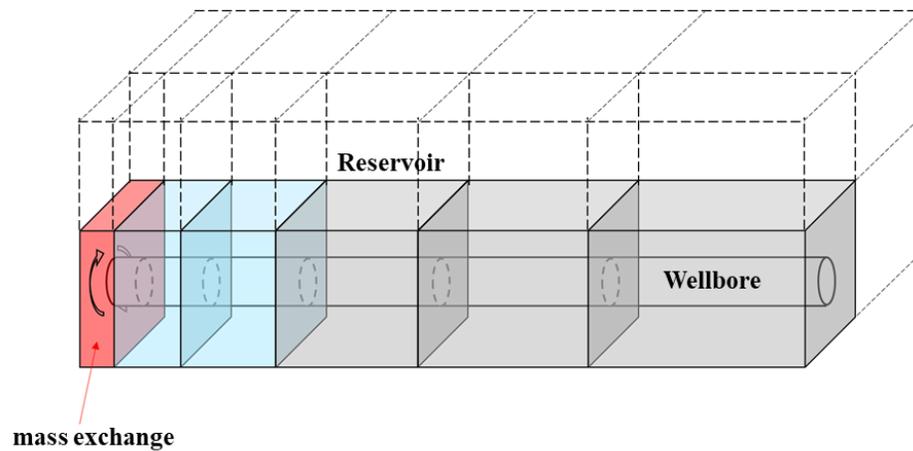
Figure 2.7 Reservoir model and wellbore model coupling

2.3.2 Model Discretization

In this section, the discretization for the governing equations is explained.

2.3.2.1 Reservoir Model

The reservoir model is formulated in 3-dimension. Figure 2.8 shows the numbering of the grid (i, j, k) and its adjacent grids.
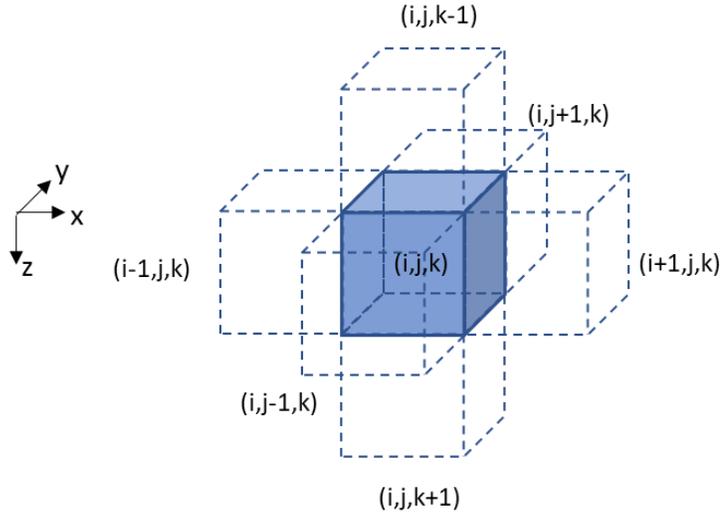
Figure 2.8 Reservoir grid block

For simplicity, define the mass accumulative terms for oil, water, and gas as the following.

$$A_o = \phi c_{Oo} \rho_o S_o \tag{2.67}$$

$$A_w = \phi \rho_w S_w \tag{2.68}$$

$$A_g = \phi \rho_g S_g + \phi c_{Go} \rho_o S_o \tag{2.69}$$

Define the mass flux terms for oil, water, and gas as:

$$F_o = c_{Oo} \rho_o \boldsymbol{u}_o \tag{2.70}$$

$$F_w = \rho_w \boldsymbol{u}_w \tag{2.71}$$

$$F_g = \rho_g \boldsymbol{u}_g + c_{Go} \rho_o \boldsymbol{u}_o \tag{2.72}$$

Define the heat accumulation term as the following.

$$A_\theta = \phi \sum_c \rho_c S_c U_c + (1 - \phi)\rho_r U_r \tag{2.73}$$

Define the heat flux term as the following.

$$F_\theta = \sum_c \rho_c H_c \boldsymbol{u}_c - \lambda \nabla T \tag{2.74}$$

39

In the above equations, A denotes the accumulative term, F denotes the flux term, and the subscript θ represents thermal.

The reservoir model described by Equations 2.1 to 2.3 and Equations 2.6 to 2.7 is discretized in space and time with the fully implicit scheme. n represents the current time which is the n-th timestep, and Δt is the timestep size. Take Equation 2.1 as an example, we discretize the equation and rearrange all the terms to one side of the equation, which is shown as the following.

$$\frac{1}{\Delta t}\left[(A_o)_{ijk}^{n+1} - (A_o)_{ijk}^n\right] + \frac{1}{V_{ijk}}\left(\sum_f A_f(F_o)_{ijk,f}^{n+1}\right) - (c_{Oo}q_o)_{ijk}^{n+1} = 0 \qquad (2.75)$$

We define this equation as the residual equation of the grid block (i, j, k) for the next timestep $(n+1)$, which is expressed by the following equation.

$$R_{ijk,oil}^{n+1} = \frac{1}{\Delta t}\left[(A_o)_{ijk}^{n+1} - (A_o)_{ijk}^n\right]$$

$$+ \frac{1}{V_{ijk}}\left(\sum_f A_f(F_o)_{ijk,f}^{n+1}\right) - (c_{Oo}q_o)_{ijk}^{n+1} = 0 \qquad (2.76)$$

To solve the equation, we use the Newton-Raphson method to find the root of this equation through iterations by approaching the residual close enough to 0. The method will be discussed in Section 2.3.3 in detail.

Because the governing equations are a set of equations, we have a set of residual equations which are expressed as the following.

Mass balance:

$$R_{ijk,oil}^{n+1} = \frac{1}{\Delta t}\left[(A_o)_{ijk}^{n+1} - (A_o)_{ijk}^n\right]$$

$$+ \frac{1}{V_{ijk}}\left(\sum_f A_f(F_o)_{ijk,f}^{n+1}\right) - (c_{Oo}q_o)_{ijk}^{n+1} = 0 \qquad (2.77)$$

40

$$R_{ijk,water}^{n+1} = \frac{1}{\Delta t}\left[(A_w)_{ijk}^{n+1} - (A_w)_{ijk}^n\right]$$

$$+ \frac{1}{V_{ijk}}\left(\sum_f A_f (F_w)_{ijk,f}^{n+1}\right) - (q_w)_{ijk}^{n+1} = 0 \tag{2.78}$$

$$R_{ijk,gas}^{n+1} = \frac{1}{\Delta t}\left[\left(A_g\right)_{ijk}^{n+1} - \left(A_g\right)_{ijk}^n\right]$$

$$+ \frac{1}{V_{ijk}}\left(\sum_f A_f \left(F_g\right)_{ijk,f}^{n+1}\right) - (q_g + c_{Go}q_o)_{ijk}^{n+1} = 0 \tag{2.79}$$

in which V_{ijk} is the cell volume, subscription f is cell face index, and A_f is the face area between cell (i, j, k) and its adjacent cell. Each grid cell has six faces, as shown in Figure 2.8, the left, right, front, back, up and down faces, which are indexed from 1 to 6 accordingly.

Energy balance:

$$R_{ijk,\theta}^{n+1} = \frac{1}{\Delta t}\left[(A_\theta)_{ijk}^{n+1} - (A_\theta)_{ijk}^n\right]$$

$$+ \frac{1}{V_{ijk}}\left(\sum_f A_f (F_\theta)_{ijk,f}^{n+1}\right) - (\sum_c H_c q_c + q_{wb})_{ijk}^{n+1} = 0 \tag{2.80}$$

2.3.2.2 Wellbore Model

The wellbore model is formulated in 1-dimension. Figure 2.9 shows the grid block numbering as well as the face numbering for the wellbore model.
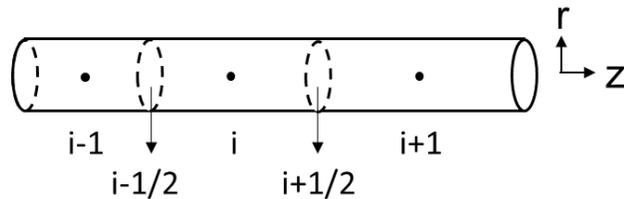
Figure 2.9 Wellbore grid block

Similar to the reservoir model, define the mass accumulative terms for oil, water, and gas for simplicity.

$$A_{o,well} = \rho_o y_o c_{Oo} \tag{2.81}$$

$$A_{w,well} = \rho_w y_w \tag{2.82}$$

$$A_{g,well} = \rho_g y_g + \rho_o y_o c_{Go} \tag{2.83}$$

Define the mass flux terms for oil, water, and gas as:

$$F_{o,well} = \rho_o y_o c_{Oo} v_o \tag{2.84}$$

$$F_{w,well} = \rho_w y_w v_w \tag{2.85}$$

$$F_{g,well} = \rho_g y_g v_g + \rho_o y_o v_o c_{Go} \tag{2.86}$$

Define the heat accumulation term as the following.

$$A_{\theta,well} = \Sigma_c \, y_c \rho_c \left(U_c + \frac{v_c^2}{2} \right) \tag{2.87}$$

Define the heat flux term as the following.

$$F_{\theta,well} = \Sigma_c \, y_c \rho_c v_c \left(H_c + \frac{v_c^2}{2} \right) - k_f \frac{\partial T}{\partial z} \tag{2.88}$$

The wellbore model described by Equations 2.18 to 2.21 and Equation 2.29 is discretized in space and in time. The residual equations for timestep $n+1$ are expressed as the following.

Mass balance:

$$R_{i,oil}^{n+1} = \frac{1}{\Delta t} \left[\left(A_{o,well} \right)_i^{n+1} - \left(A_{o,well} \right)_i^n \right]$$

$$+ \frac{1}{V_i} \left(A_{i+\frac{1}{2}} \left(F_{o,well} \right)_{i+\frac{1}{2}}^{n+1} - A_{i-\frac{1}{2}} \left(F_{o,well} \right)_{i-\frac{1}{2}}^{n+1} \right)$$

$$+ \frac{2\gamma}{R} \left(\rho_{o,I} y_{o,I} c_{Oo,I} v_{o,I} \right)_i^{n+1} = 0 \tag{2.89}$$

42

$$R_{i,water}^{n+1} = \frac{1}{\Delta t}\left[\left(A_{w,well}\right)_i^{n+1} - \left(A_{w,well}\right)_i^{n}\right]$$

$$+ \frac{1}{V_i}\left(A_{i+\frac{1}{2}}\left(F_{w,well}\right)_{i+\frac{1}{2}}^{n+1} - A_{i-\frac{1}{2}}\left(F_{w,well}\right)_{i-\frac{1}{2}}^{n+1}\right)$$

$$+ \frac{2\gamma}{R}\left(\rho_{wI}y_{wI}v_{wI}\right)_i^{n+1} = 0 \tag{2.90}$$

$$R_{i,gas}^{n+1} = \frac{1}{\Delta t}\left[\left(A_{g,well}\right)_i^{n+1} - \left(A_{g,well}\right)_i^{n}\right]$$

$$+ \frac{1}{V_i}\left(A_{i+\frac{1}{2}}\left(F_{g,well}\right)_{i+\frac{1}{2}}^{n+1} - A_{i-\frac{1}{2}}\left(F_{g,well}\right)_{i-\frac{1}{2}}^{n+1}\right)$$

$$+ \frac{2\gamma}{R}\left(\rho_{g,I}y_{g,I}v_{g,I} + c_{Go,I}\rho_{o,I}y_{o,I}v_{o,I}\right)_i^{n+1} = 0 \tag{2.91}$$

Momentum balance:

$$R_i^{n+1} = \frac{1}{\Delta t}\left[\left(\sum_c y_c\rho_c v_c\right)_i^{n+1} - \left(\sum_c y_c\rho_c v_c\right)_i^{n}\right] + \frac{1}{V_i}\left(A_{i+\frac{1}{2}}p_{i+\frac{1}{2}}^{n+1} - A_{i-\frac{1}{2}}p_{i-\frac{1}{2}}^{n+1}\right)$$

$$+ \frac{1}{V_i}\left(A_{i+\frac{1}{2}}\left(\sum_c y_c\rho_c v_c v_c\right)_{i+\frac{1}{2}}^{n+1} - A_{i-\frac{1}{2}}\left(\sum_c y_c\rho_c v_c v_c\right)_{i-\frac{1}{2}}^{n+1}\right)$$

$$+ \frac{1}{R}\left(\rho_m v_m |v_m| f_m\right)_i^{n+1} - \left(\rho_m\right)_i^{n+1}\boldsymbol{g}_{m,z} = 0 \tag{2.92}$$

Energy balance:

$$R_{i,\theta}^{n+1} = \frac{1}{\Delta t}\left[\left(A_{\theta,well}\right)_i^{n+1} - \left(A_{\theta,well}\right)_i^{n}\right]$$

$$+ \frac{1}{V_i}\left[A_{i+\frac{1}{2}}\left(F_{\theta,well}\right)_{i+\frac{1}{2}}^{n+1} - A_{i-\frac{1}{2}}\left(F_{\theta,well}\right)_{i-\frac{1}{2}}^{n+1}\right]$$

$$+ \left[\frac{2\gamma}{R}\left(\sum_c y_{c,I}v_{c,I}\rho_{c,I}\left(H_{c,I} + \frac{v_{c,I}^2}{2}\right)\right)\right]_i^{n+1}$$

$$- \left[\frac{2(1-\gamma)}{R}U_T\left(T_{res} - T_{wf}\right)\right]_i^{n+1} - \left[\sum_c y_c\rho_c v_c g_{c,z}\right]_i^{n+1} = 0 \tag{2.93}$$

In Equations 2.89 to 2.93, $A_{i+1/2}$ and $A_{i-1/2}$ are the face area for faces *i+1/2* and *i-1/2* as depicted in Figure 2.9.

2.3.3 Numerical Method

In Section 2.3.2, the discretized equations for the reservoir model and the wellbore model are presented. In each numerical simulation domain (the reservoir, and the wellbore), the system of equations is solved by the Newton-Raphson method.

Let $R(x)$ be the residual and x_{root} be the root of equation $R(x) = 0$. Since we are solving a set of equations for each cell, we use the vectors for the residual $\boldsymbol{R(x)}$, and $\boldsymbol{x_{root}}$. Newton-Raphson method starts with the initial estimation of $\boldsymbol{x_1}$, and approaches the root through iterations until the $\boldsymbol{R(x)}$ is close enough to 0.

Assume $\boldsymbol{x_n}$ is the current estimation, then the next estimation $\boldsymbol{x_{n+1}}$ can be calculated through the equation:

$$\boldsymbol{x_{n+1}} = \boldsymbol{x_n} + \boldsymbol{\delta x_{n+1}} \tag{2.94}$$

in which the update δx_{n+1} is computed as

$$\boldsymbol{\delta x_{n+1}} = -\boldsymbol{J}^{-1}\boldsymbol{R} \tag{2.95}$$

$\boldsymbol{R}$ is the residual vector, $\boldsymbol{J}$ is the Jacobian matrix which is expressed as:

$$\boldsymbol{J} = \begin{bmatrix} J_{11} & \cdots & J_{1n} \\ \vdots & \ddots & \vdots \\ J_{n1} & \cdots & J_{nn} \end{bmatrix} \tag{2.96}$$

and the component J_{ij} is calculated by the following equation.

$$J_{ij} = \frac{\partial R_i}{\partial x_j} \tag{2.97}$$

where R_i is the i-th element of the residual vector, and x_j is the j-th element of the solution vector.

2.3.4 Solution Procedure

The reservoir model and the wellbore model are solved separately and are solved using the fully implicit method. Then the two models are integrated iteratively within each time step. Figure 2.10 shows the solution procedure of the coupled model.

First, we start with initializing the reservoir system and wellbore system. For each time step, we first assume the wellbore hold up, pressure and temperature, and keep these parameters fixed as the boundary condition for the reservoir model. The reservoir flow and thermal models are solved simultaneously to estimate the reservoir pressure, saturation, temperature, and mass flow rate. Then we solve the wellbore model to get the velocity, hold up, pressure and temperature in the wellbore using the reservoir condition as the boundary condition. The calculation needs iterations until the calculated wellbore hold up, pressure and temperature are close enough to the assumptions, or the maximum number of iterations is obtained. Once it converged, we save the calculation results of reservoir pressure, temperature, saturation and wellbore hold up, pressure and temperature for this time step. Then we move to the next time step.
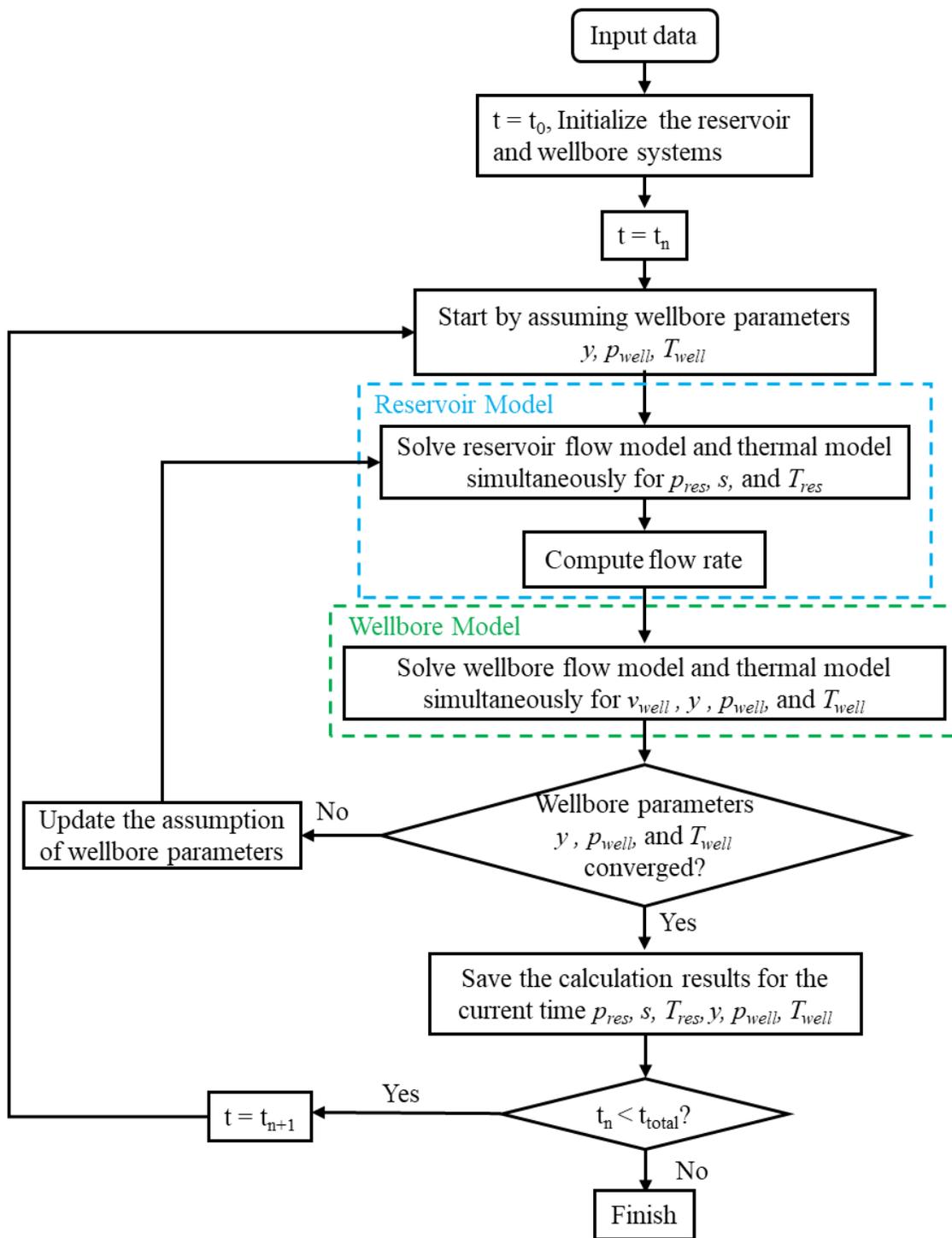
Figure 2.10 Solution procedure

46

2.4 Model Validation

The developed black-oil thermal model is validated against different models developed previously, including different situations from hydraulic fracturing treatment, and well shut-in to well production. Also, the result of this model is compared with the compositional model, the semi-analytical model, as well as the analytical model. The advantages and limitations of this model, as well as when and how to apply this black-oil thermal model to fulfill its full advantages, are discussed in this section.

2.4.1 Model Validation against Compositional Model

The developed model from this work is first validated against the multiphase compositional model (Yoshida 2016; Yoshida et al. 2018). For simplicity, the multiphase compositional model is referred to as Yoshida's model in the following content. In this model, we ignore the near-wellbore flow convergence effect and assume a linear flow within the fracture. Yoshida's model can include the near-wellbore flow convergence which has radial flow near the wellbore (Yoshida et al. 2018). Options are given to choose either consider or ignore the near wellbore flow convergence when using Yoshida's model. For better validation, it is also decided to ignore the near-wellbore flow convergence when using Yoshida's model to simulate the temperature profile. We use a similar single fracture example presented in the original publication (Yoshida et al. 2018) and use the same gridding systems.

In the validation case, a segment of a horizontal well with a single fracture is simulated. This geometry represents a part of a multi-stage fractured horizontal well.

47

Figure 2.11 shows the geometry. The well is treated with an injection rate of 18 bpm which is equivalent to 90 bpm for a stage with 5 clusters. The injection lasts 100 min, and the fluid injection temperature is constant at 80 °F. During injection, a fracture with 1000 ft half-length and infinite conductivity is created. Then, the well is shut in for 30 days, and after closure, the propped fracture half-length reduces to 300 ft and the fracture conductivity is 20 md·ft. We simulate a production period for 100 days, and the well is operating at constant bottomhole pressure of 2600 psi. Table 2.3 and Table 2.4 summarize the primary input data and the rock and fluid properties for this case.
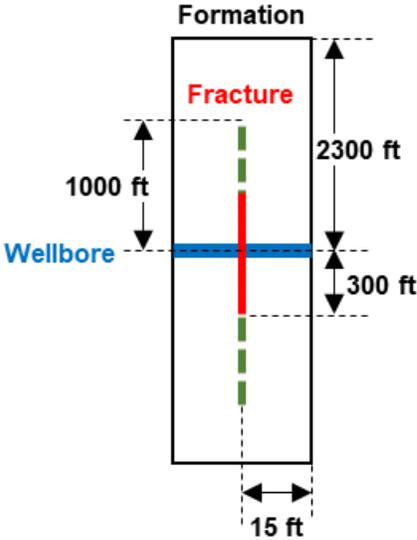
Figure 2.11 Single fracture geometry

Table 2.3 Input data for model validation against compositional model

Region	Parameter	Value
Reservoir	Net pay thickness, ft	160
	Matrix permeability, nD	583
	Matrix porosity, %	4.2
	Initial pressure, psi	4500
	Initial temperature, °F	238.4
	Residual water saturation, fraction	0.1
Fracture	Fracture width, in	0.24
	Fracture porosity, %	20
	Fracture height, ft	160
	Fracture half-length (injection), ft	1000
	Fracture half-length (shut-in and production), ft	300

Table 2.4 Rock and fluid properties

Media	Parameter	Value
Rock	Rock Density, kg/m^3	2380
	Thermal conductivity, W/m·K	1.6
	Specific heat, J/kg·K	847
	Pore compressibility, 1/Psia	6.89E-06
Gas	Density, kg/m^3	0.656
	Thermal conductivity, W/m·K	0.058
	Specific heat, J/kg·K	3078
	Viscosity, cp	0.0256
Water	Density, kg/m^3	985.9
	Thermal conductivity, W/m·K	0.66
	Specific heat, J/kg·K	4136
	Viscosity, cp	0.55

We first compare the temperature profile along the fracture plane during injection and shut-in. The results are shown in Figure 2.12. In this figure, the x-axis is the distance from the wellbore, and 0 ft starts from the sandface. In both plots, the dashed lines are the simulation results from this work, and the solid lines are the simulation results from Yoshida's model. The results show a satisfactory agreement.

We also compare the inflow temperature during production. Here we define the inflow temperature as the fluid temperature at the intersection of the fracture and wellbore before the inflow fluid mixes with the wellbore fluid. Figure 2.13 shows the comparison result. In general, the results match well, and the two models show consistency with each other. This good match has validated that the developed black-oil thermal model showed the correct computation from injection, shut-in until production for gas-water two-phase flow.

In this validation case, the simulation domain, which is a quarter of the original domain, is discretized with 14 grids along wellbore direction, 81 grids along fracture direction and 1 layer in the height direction. In total, there are 1134 grids. The time is discretized with 43 timesteps during injection, 10 timesteps during shut-in and 41 timesteps during production. The total computation time for this two-phase flow case from injection to shut-in and production is about 4.46 minutes using this developed black-oil thermal model. With Yoshida's model, the computation time is 89.21 minutes with the same grids. For this validation case, the computational time of this developed black-oil thermal model is approximately 20 times faster than Yoshida's model.
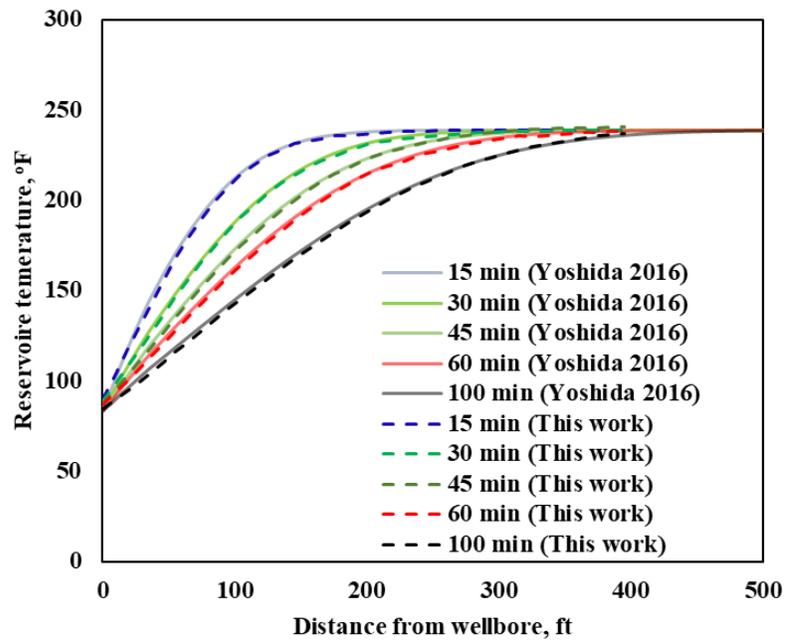
(a) Injection
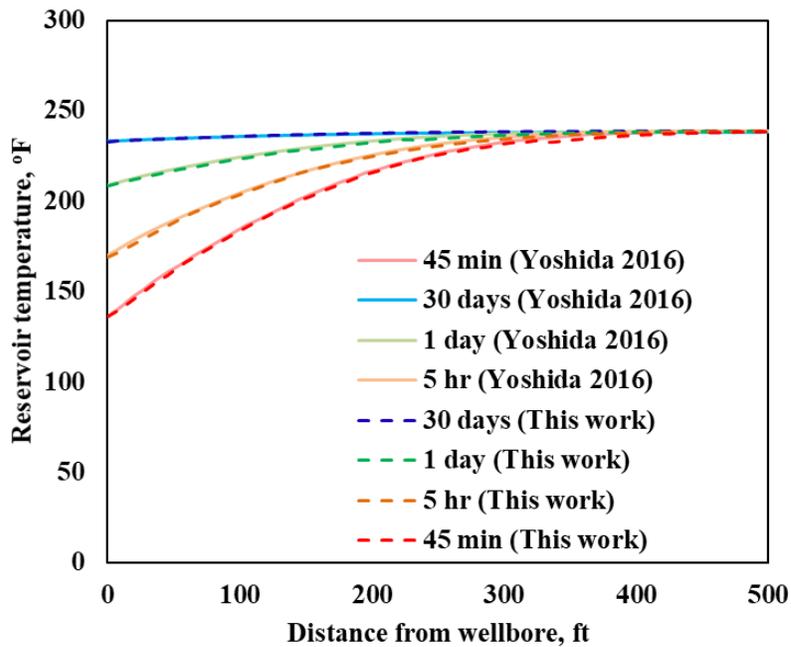
(b) Shut-in

Figure 2.12 Temperature profile along the fracture plane during injection and shut-in
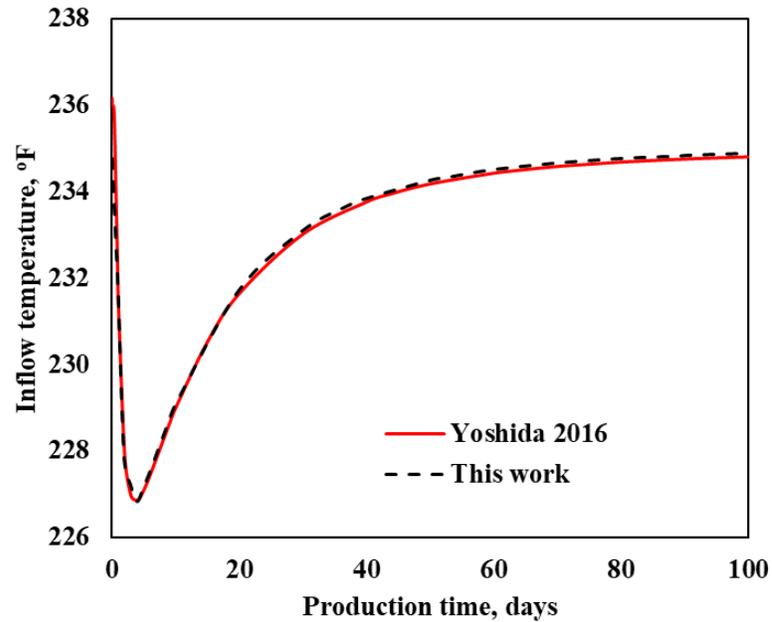
Figure 2.13 Inflow temperature during production

2.4.2 Model Validation against Semi-Analytical Model

This black-oil thermal model is also validated against the semi-analytical model (Cui 2015; Cui et al. 2016a). The semi-analytical model simulates the transient temperature response for single phase production in horizontal wells with multiple fractures. It assumes the homogenous reservoir and tri-linear flow during production. Figure 2.14 shows the tri-linear flow pattern in which the fluid is flowing from outer formation to inner formation, from inner formation to fracture and from fracture to horizontal wellbore. The semi-analytical model also consists of the reservoir model and the wellbore model. The wellbore model is solved numerically. The reservoir flow model is solved by Laplace transform with an analytical solution in the Laplace domain, and the results are converted back from Laplace domain to the real domain numerically.
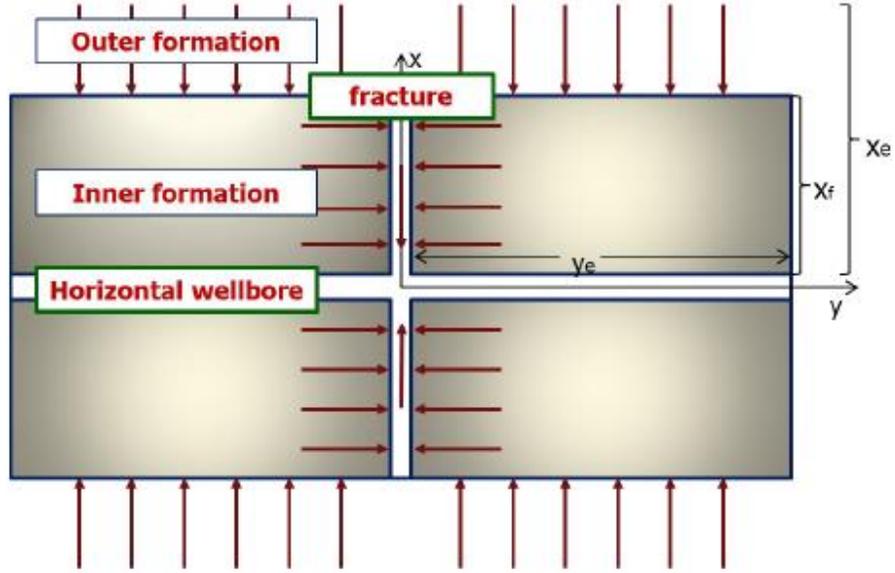
Figure 2.14 Tri-linear flow (reprinted from (Cui 2015))

In the semi-analytical model, the solution in the Laplace domain l for the outer formation is:

$$\bar{p}_{OD} = \bar{p}_{ID}|_{x_D=1} \exp\left[-\sqrt{\frac{l}{\eta_{OD}}}(x_D - 1)\right] \qquad (2.98)$$

The solution in the Laplace domain l for the inner solution is:

$$\bar{p}_{ID} = \frac{\bar{p}_{FD}}{1+\sqrt{\alpha_O}S} \exp\left(-\sqrt{\alpha_O}y_D\right) \qquad (2.99)$$

where $\alpha_O = \sqrt{l/\eta_{OD}} + l$.

The solution in the Laplace domain l for the fracture is:

$$\bar{p}_{FD} = \frac{\pi/F_{CD}}{l\sqrt{\alpha_F}\tanh\sqrt{\alpha_F}} \qquad (2.100)$$

where $\alpha_F = \frac{2/F_{CD}\sqrt{\alpha_O}}{1+\sqrt{\alpha_O}S} + \frac{l}{\eta_{FD}}$

In the above equations, the dimensionless parameters are defined as follows:

53

$$p_D = \frac{141.2kh}{qB\mu}(p_i - p) \text{ for oil} \tag{2.101}$$

$$p_D = \frac{kh}{1424qT}[m(p_i) - m(p)] \text{ for gas} \tag{2.102}$$

$$\eta = \frac{k}{\phi\mu c_t} \tag{2.103}$$

$$t_D = \frac{kt}{\phi\mu c_t x_f^2} = \frac{\eta t}{x_f^2} \tag{2.104}$$

$$x_D = \frac{x}{x_f} \tag{2.105}$$

$$y_D = y/y_e \tag{2.106}$$

$$F_{CD} = \frac{k_f w}{k x_f} \tag{2.107}$$

$$\eta_{FD} = \frac{\eta_F}{\eta} \tag{2.108}$$

$$\eta_{OD} = \frac{\eta_O}{\eta} \tag{2.109}$$

in which k is the reservoir permeability, h is the reservoir height, q is the surface flow rate, B is the formation volume factor, μ is the fluid viscosity, p_i is the initial pressure, p is the pressure, Φ is the porosity, c_t is the total compressibility, x_f is the fracture half-length, k_f is the fracture permeability, and w is the fracture width.

In the semi-analytical model, the reservoir thermal model is solved analytically by the operator splitting algorithm. During each timestep, the hyperbolic convection part is first solved to get the convective temperature distribution, and then this distribution is used as the initial condition to solve the diffusion part.

For $t \in (t^n, t^{n+1})$, the heat convection solution is:

$$T_{conv}(t^{n+1}, y) = T_0 e^{\left(F(t^{n+1}) - F(t^n)\right)} + \int_0^{t^{n+1}} \frac{\mu}{k\rho C_p} \frac{q^2}{(4x_f h)^2} e^{\left(F(t^{n+1}) - F(t^n)\right)} dt$$

$$(2.110)$$

At the same time step, the diffusion part is solved as:

$$T_{cond}(x, y, t^{n+1}) = \sum_{m=1}^{\infty} \sum_{n=1}^{\infty} D_{mn} \, e^{-(\mu_m^2 + v_n^2)\alpha(t^{n+1} - t^n)} \cos(\mu_m x) \cos(v_n y)$$

$$(2.111)$$

In the above two equations,

$$F(t) = \int \left(\frac{\phi\beta}{\rho C_p} \frac{\partial p}{\partial t} - \frac{\beta k}{\mu\rho C_p} \left(\frac{\partial p}{\partial t}\right)^2 \right) dt \qquad (2.112)$$

$$D_{mn} = \frac{4}{x_f y_e} \int_{y=0}^{y_e} \int_{x=0}^{x_f} F(x, y) \cos(\mu_m x) \cos(v_n y) \, dx dy \qquad (2.113)$$

where $F(x,y)$ is the initial condition, β is the thermal expansion coefficient.

Part of the semi-analytical model can be solved analytically which can save some computational time. Meantime, it still requires some numerical computation to solve the wellbore model and to perform the numerical Laplace transform.

To compare with the semi-analytical model, we simulate the same case using the developed black-oil model. In this validation case, a segment of a horizontal well with a single fracture is also simulated. Figure 2.15 shows the geometry. The well is producing gas at a constant bottomhole pressure of 2600 psi for 100 days. Table 2.5 summarizes the primary input data for this case. Table 2.6 shows the rock and fluid properties.
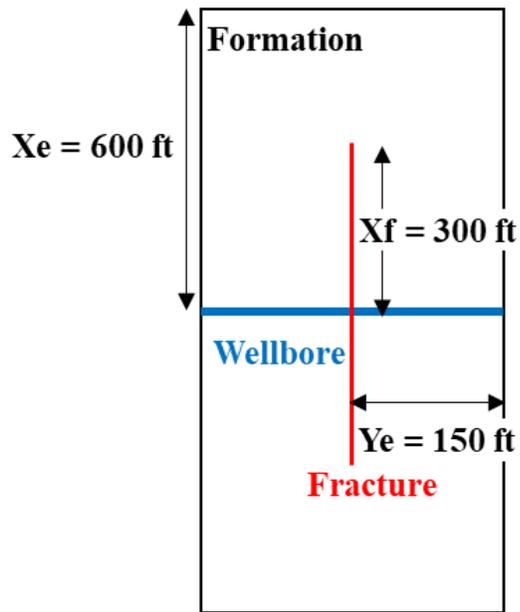
Figure 2.15 Single fracture geometry during production

Table 2.5 Input data for model validation against the semi-analytical model

Region	Parameter	Value
Reservoir	Net pay thickness, ft	160
	Matrix permeability, nD	583
	Matrix porosity, %	4.2
	Initial pressure, psi	4500
	Initial temperature, °F	238.37
Fracture	Fracture width, in	0.24
	Fracture permeability, md	1000
	Fracture porosity, %	20
	Fracture height, ft	160

Table 2.6 Rock and fluid properties

Media	Parameter	Value
Rock	Rock Density, kg/m^3	2380
	Thermal conductivity, W/m·K	3.1
	Specific heat, J/kg·K	845.7
	Pore compressibility, 1/Psia	6.89E-06
Gas	Gas type	Methane
	Molecular weight	16
	Thermal conductivity, W/m·K	0.058
	Specific heat, J/kg·K	3078
	Viscosity, cp	0.0256

Figure 2.16 and Figure 2.17 compare the temperature and pressure profile along the fracture plane during production. Despite some discrepancies near the fracture tip region (fracture tip is at 300 ft), the temperature and pressure match well along the fracture plane between these two models. These discrepancies are because that the semi-analytical model assumes linear flow from the outer formation to the inner formation, while in this model there is flow convergence around the fracture tip. Also, the gas flow rate is compared, as shown in Figure 2.18. The result of this model matches very well with the result of the semi-analytical model. Overall, the result for production matches well between each model and the two models show satisfactory consistency.

In this validation case, the simulation domain is discretized with 65 grids along the wellbore direction, 81 grids along the fracture direction and 1 layer in the height direction, which results in a total of 5265 grids. There are 80 timesteps in this simulation. The computation time for this validation case is 11.60 minutes using the developed black-oil

thermal model and 1.93 minutes using the semi-analytical model. For this validation case, the computational speed of the semi-analytical solution is about 6 times faster than this developed black-oil thermal model.
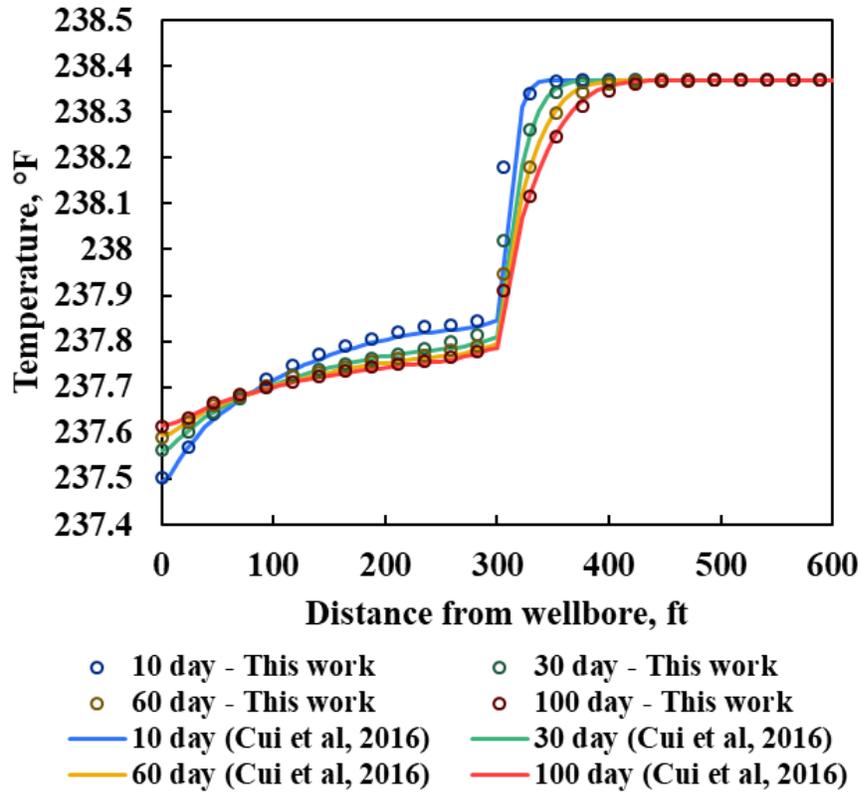

Figure 2.16 Temperature profile along the fracture plane during production
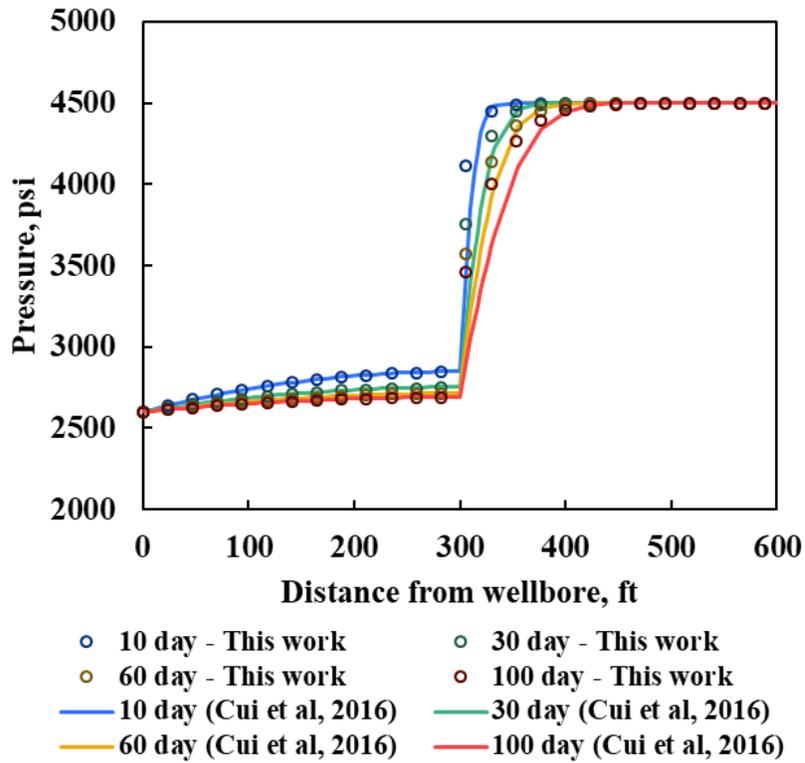
**Figure 2.17 Pressure profile along the fracture plane during production**
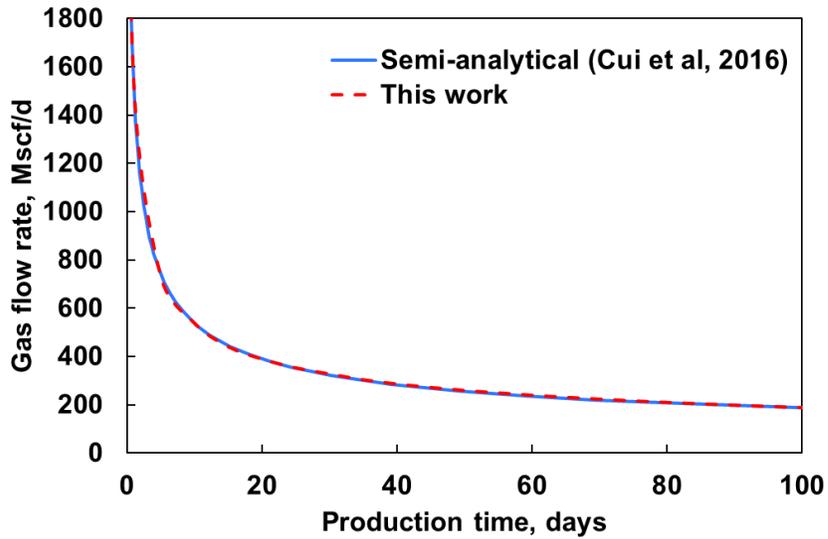
Figure 2.18 Gas production rate

59

2.4.3 Model Validation against Analytical Solution

During the hydraulic fracturing injection process, Seth et al. (2010) developed an analytical solution to compute the temperature inside the fracture. The analytical model ignores the fluid leak-off into the formation and assumes the rock matrix temperature is constant and equals initial reservoir temperature. In the analytical solution, the temperature inside the fracture can be calculated by:

$$T_D(x,t) = \begin{cases} 0 & \text{when } x - u_{fr}t > 0 \\ e^{-x\frac{\eta}{u_{fr}}} & \text{when } x - u_{fr}t < 0 \end{cases} \qquad (2.114)$$

in which x is the coordinate along the fracture plane, t is the injection time, u_{fr} is the fracturing fluid velocity inside the fracture along the direction of fracture propagation. The dimensionless parameters T_D and η are defined by the following equations.

$$T_D = \frac{T_{init} - T_{fr}}{T_{init} - T_{inj}} \qquad (2.115)$$

$$\eta = \frac{2h_l u_{fr}}{\rho_l u_{fr} c_l w} \qquad (2.116)$$

where T_{init} is the initial reservoir temperature, T_{fr} is the temperature inside the fracture, T_{inj} is the injection fluid temperature, h_l is the heat transfer coefficient, ρ_l is the fluid density, c_l is the specific heat capacity of fluid, and w is the fracture width.

To compare the developed black-oil thermal model with the analytical solution, the same validation case described in Section 2.4.1 is used here. In the simulation using the black-oil thermal model, and the zero fluid leak-off into the formation is adopted to be comparable to the analytical solution. Figure 2.19 shows the temperature profile along the fracture plane at the end of injection. The simulation result from the developed model

60

matches well with the analytical solution, which confirms the validation of the developed

black-oil thermal model for temperature simulation during injection.
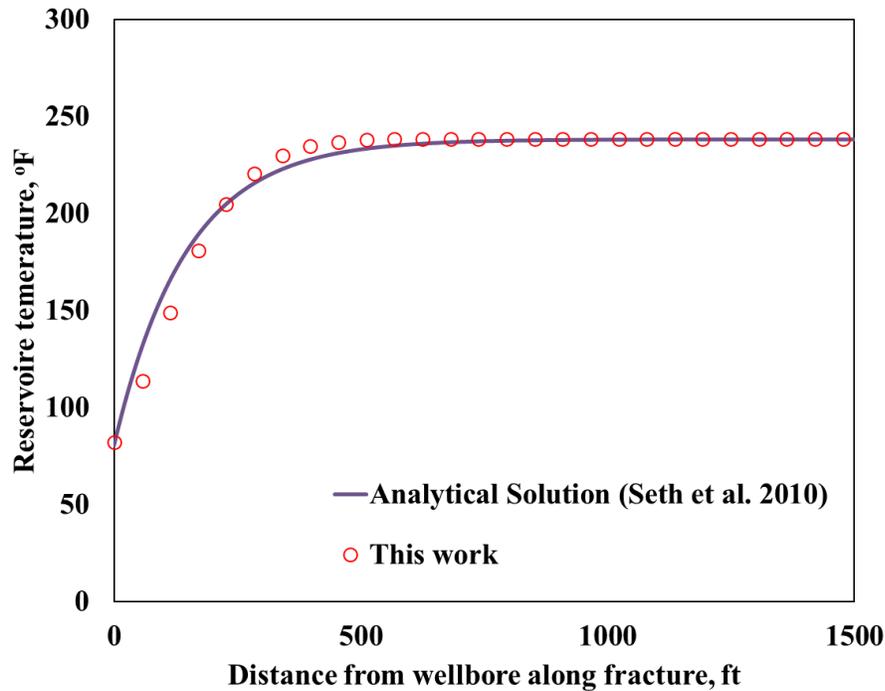
Figure 2.19 Temperature profile along the fracture plane at the end of the injection

2.4.4 Model Advantages and Limitations

Comparing with Yoshida's model (Yoshida 2016; Yoshida et al. 2018), the

computational time of this newly developed model is approximately 20 times faster. The

rapid computation time allows this model to be further used in the interpretation of

downhole temperature measurements. The interpretation requires many forward

simulations so that a reasonably fast computational speed of the forward model becomes

essential. These two models have two main differences. First, in this model, we assume

the black-oil fluid which only has mass transfer between the gas phase and the oil phase.

While the compositional model considers multiphase and multicomponent, which is more accurate but also results in more equations to solve. Second, Yoshida's model can consider the near-wellbore flow convergence which combines the linear and radial flow, while in this model we assume all linear flow in the fracture. Based on the results presented by Yoshida et al. (2018), ignoring the near-wellbore flow convergence may overestimate the temperature along the fracture plane near the wellbore region. However, the inflow temperature does not have significant differences. The inflow temperature is the fluid temperature at the intersection of fracture and wellbore, and that is what matters to temperature interpretation. The influence may be substantial in some extreme cases such as limited-entry completion design when the near-wellbore convergence is noteworthy. Considering the near-wellbore convergence requires a local grid refinement in the numerical simulation, which will dramatically increase the computational time. Overall, this model simplifies Yoshida's model with comparable simulation results for general cases and dramatically faster computational speed.

Compared with the semi-analytical solution (Cui et al. 2016a) for single phase production, this model can solve the multiphase flow during not only production but also the injection and shut-in period. Furthermore, this model can handle heterogenous formation while the semi-analytical solution assumes a homogenous reservoir. However, the computational speed of the semi-analytical solution is about 6 times faster than this multi-phase black-oil thermal model with 5265 grid blocks for the validation case presented in Section 2.4.2.

Overall, the model presented in this work is a compromise between the compositional model and the semi-analytical model. The developed black-oil model is suitable for the following situations:

- when two-phase flow needs to be considered

- when reservoir heterogeneity needs to be considered

- when the temperature needs to be computed from injection, to shut-in and production

- when a fast computation speed is needed but meantime the problem is more complicated than what the semi-analytical model can handle.

The developed black-oil model will show discrepancy and are not accurate enough or not applicable in the following situations:

- when the influence on the temperature of the composition change is not negligible

- when the interference between each fracture is non-negligible, for example, when the cluster space is too close to each other.

- when three-phase flow at the downhole must be considered.

2.5 Section Summary

This section introduces the multi-phase black-oil thermal model developed to simulate the transient temperature behavior during hydraulic fracturing fluid injection, shut-in, and well production. This model includes a reservoir model and a wellbore model, which are coupled iteratively through the boundary conditions. The details of the

governing equations and constitutive equations, as well as the numerical implementation of this model, are described in this section. The model is validated against the compositional model, semi-analytical model, and analytical solution. This model shows a consistent result as the other models. Compared with the compositional model, this model has a faster computational speed. Compared with the semi-analytical model, this model can handle two-phase oil/water or gas/liquid flow and heterogeneous reservoirs. When the influence of the composition changes and the impact of near wellbore flow convergence on temperature are significant, this developed model may have deviation. The model applies to most of the common field conditions.

CHAPTER III

TEMPERATURE INTERPRETATION METHODOLOGY

3.1 Introduction

Because of the current massive fracture treatments (large volume and high injection rate) and complex fracture networks that are created from fracture stimulation, an efficient interpretation procedure is essential for the downhole temperature measurement from fiber optic cable or production logging tools to be practically used in the industry. This interpretation procedure should include a robust and meanwhile relatively fast forward model to calculate the temperature response and a high-efficient inversion algorithm to match the forward simulation with the measured temperature data.

In the last chapter, the multiphase black-oil thermal model is presented. This model is computationally efficient while maintaining the robustness, which makes this developed model a practical tool for the forward simulation. However, we also need an efficient inversion algorithm to match the simulated temperature with the measured temperature by updating inversion parameters through iterations. The inversion algorithm needs to be able to converge fast, maximumly reduce the uncertainties, and lead to sensible solutions.

In this chapter, an inversion procedure is proposed to meet these requirements and is applied to a synthetic example, which proves the effectiveness and efficiency of this inversion procedure.

3.2 Sensitivity Analysis

The developed multi-phase black-oil thermal model can be applied to the interpretation of downhole temperature measurements to generate a flow rate profile along the horizontal well. When interpreting the downhole temperature, we use the developed model to simulate the temperature response and match the measured temperature with the simulation result by changing some input parameters (named as inversion parameters) and then generate the flow rate profile. It is essential to choose the parameters that have a higher impact on the temperature behavior as the inversion parameters. Hence, sensitivity analysis is performed first.

In the sensitivity study, it is assumed that the same parameters have the same level of impact on temperature behavior regardless of which fracture is studied. That is to say, we assume the fractures do not interfere with each other. Consequently, a base case is set up with only one fracture to represent a segment of the horizontal well. The well is producing gas. The parameter ranges and the base case values are given in Table 3.1 and Table 3.2. The parameters are changed by a certain percentage to compare their influence on temperature behavior. Due to the different uncertainties of each parameter, the ranges for each parameter are different. The gas and rock heat capacity has much less uncertainties compared to the other parameters. When studying one parameter's sensitivity, all the other parameters are kept at the base values, and only one parameter changes from the low value to the high value. When gas is entering the well, the Joule-Thomson cooling effect of gas will cause a temperature drop at the perforation location. By changing one parameter from the base case, the temperature drop at the perforation

location due to gas entering will changes accordingly. We compare the percentage of these temperature drops changing from the base case temperature drop to evaluate the parameters sensitivity. Figure 3.1 shows the sensitivity study result.

Table 3.1 Parameter range and base case input for sensitivity study

Parameters	-90%	-75%	-65%	-50%	-25%	Base	25%	50%	75%	150%
Matrix Permeability (nD)	58	145	-	290	435	580	725	870	1015	-
Matrix Porosity (%)	-	1.5	-	3	4.5	6	7.5	9	-	-
Fracture Permeability (md)	200	500	-	1000	1500	2000	2500	3000	3500	-
Fracture Half-length (ft)	-	80	-	160	240	320	400	480	560	-
Fracture Width (in)	-	-	0.021	-	0.045	0.06	0.075	0.09	0.105	0.15

Table 3.2 Parameter range and base case input of thermal properties

Parameters	-3.5%	-2.0%	-1.0%	Base	3.0%	4.0%	5.0%
Gas Heat Capacity (BTU/lb·°F)	0.532	0.540	0.546	0.551	0.568	0.573	0.579
Rock Heat Capacity (BTU/lb·°F)	0.191	0.194	0.196	0.198	0.204	0.206	0.208
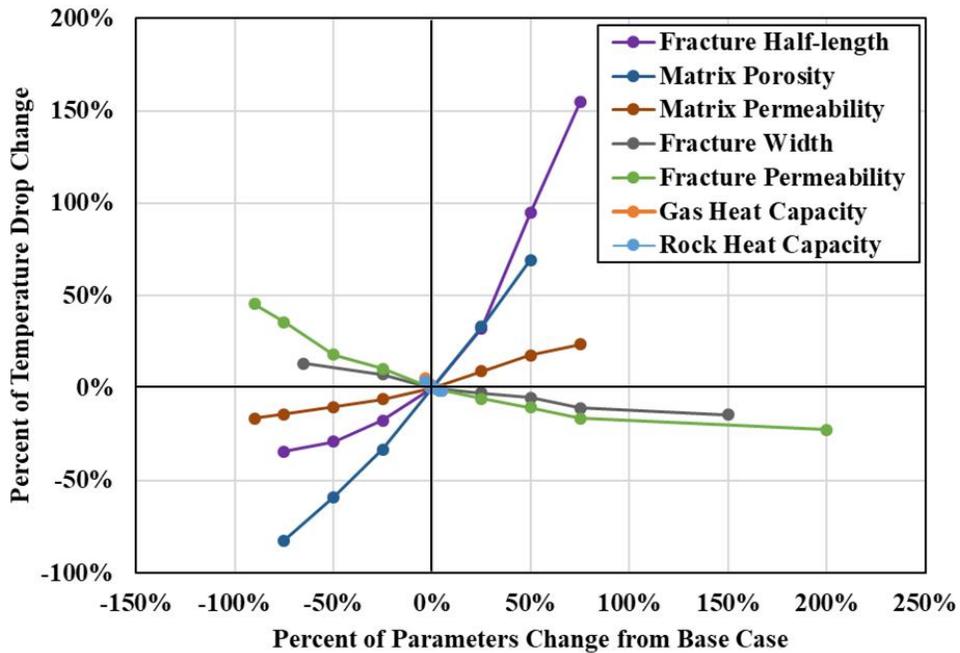
Figure 3.1 Sensitivity study result

From the sensitivity study, we can see that the fracture half-length, matrix porosity, and fracture permeability have significant influences on the temperature drop at the perforation location. When these parameters range from their low values to high values, the percentage of temperature change compared to the base case is substantial. Among these parameters, matrix porosity is more accessible from well logging. Hence, the fracture half-length and fracture permeability become the primary uncertain variables that are important to temperature behavior. If we have a fixed fracture width, the fracture conductivity will have the same sensitivity as the fracture permeability. In the temperature interpretation, we can choose either fracture conductivity or fracture half-length as the inversion parameters.

3.3 Temperature Interpretation Methodology

In this section, a generalized methodology for downhole temperature interpretation is presented. However, interpreting temperature for flow distribution is a complex problem. There are many parameters involved, from reservoir properties to well structure and completion, to fracturing design and operation. Each case should be interpreted based on its own condition, which requires modifications of the interpretation methodology based on each case. This section only explains the generalized methodology. Adjustment of the methodology for each case will be presented in Chapters 4 and 5 through field example.

3.3.1 General Interpretation Procedure

The general interpretation procedure used in this work includes four parts: Measured Data Pre-processing, Initial Evaluation, Local Temperature Matching, and Global Re-examination. Figure 3.2 shows the flow chart of the interpretation procedure. First, depending on different cases, the measured temperature data may need some pre-processing. For example, when interpreting the temperature warmback during the shut-in period, it is practical to convert the absolute temperature to the temperature recovery from the end of injection. When the signal-to-noise ratio is low which means the noise is high, data filtering helps the interpretation.
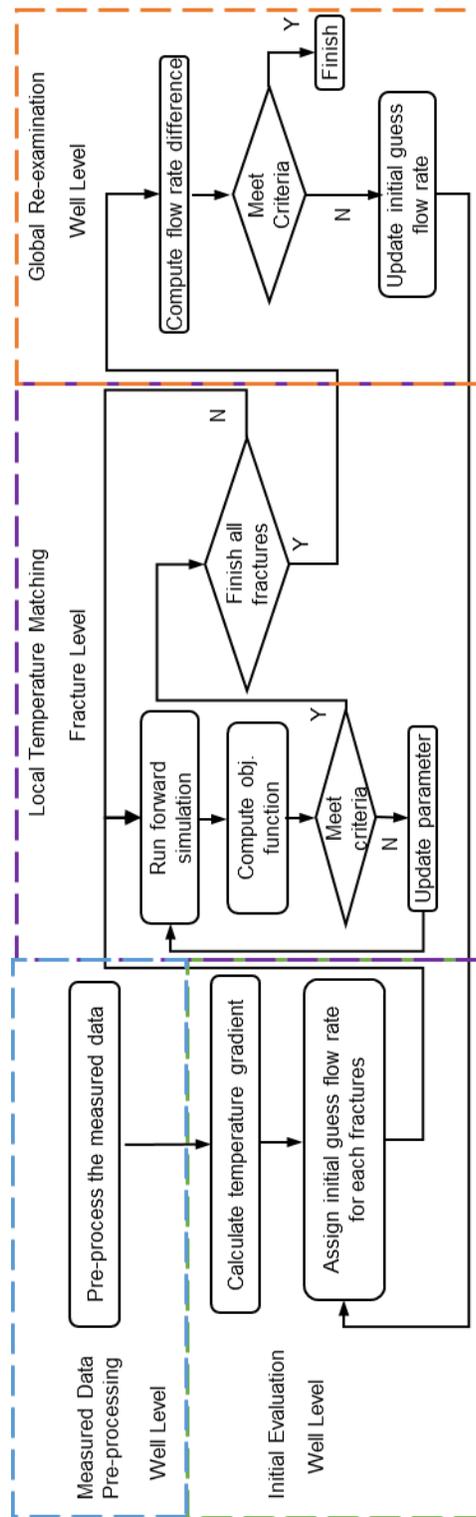
Figure 3.2 General interpretation procedure

70

The objective of Initial Evaluation is to identify the clusters contribution to flow and assign the non-uniform initial guess of the flow rate distribution. Identifying the contributing cluster is done by examining the temperature gradient along the well. The temperature gradient along wellbore is defined as the temperature derivative to distance. As shown in Figure 3.3, the temperature gradient dT/dx is defined as:

$$\frac{dT}{dx} = \frac{T_1 - T_2}{\Delta x}$$

(3.1)
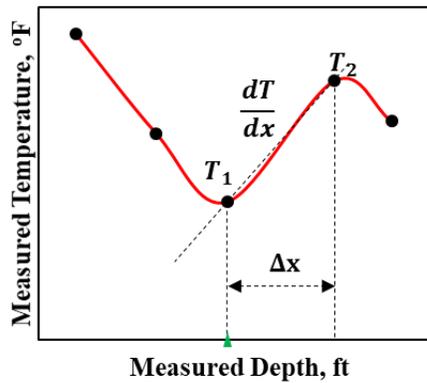
Figure 3.3 Definition of temperature gradient

For gas producing well, temperature changes sharply at the locations of gas production because of the Joule-Thomson effect. The temperature gradient at the gas production locations is negative. If the fracture does not contribute to production, the heat conduction between the reservoir and the gas in the tubing will heat the fluid, resulting in a temperature increase and therefore a positive gradient. Based on this principle we eliminate the clusters that do not contribute to gas production from interpretation. This procedure can save computation time. However, for a liquid producing horizontal well, the temperature behavior is not the same as the gas producing well during hydraulic

71

fracturing, injection and shut-in or production. Hence, we cannot diagnose the contribution of flow of each cluster only based on temperature gradient for injection, shut-in or production periods. In such a situation, it is assumed initially that all the clusters contribute to flow. Once we identify the clusters that contribute to flow, we further assign the initial guess of flow rate to each contributing cluster based on the level of temperature change. This is done by assuming that for all contributing clusters, the flow rate is proportional to how much the temperature change is, and the total flow rate from all contributing clusters must be equal to the surface flow rate from the well. Although the temperature behavior has a much more complicated relationship with the flow rate for each contributing cluster, this initial estimation provides a reasonable start point for the following inversion procedures.

The key procedure in the inversion is the third step, Local Temperature Matching. The objective is to match the simulated temperature with the measured temperature at each cluster location. A gradient method, Levenberg-Marquart algorithm (Oliver et al. 2008; Tardy et al. 2011) is adopted to update the inversion parameter during each iteration. The detailed implementation of the Levenberg-Marquart algorithm is presented in Section 3.3.2.

Once the local inversion for all the contributing clusters is finished, we need to re-examine the inverted total flow rate to match the measured total flow rate of the well. If the inverted total flow rate matches the measured total flow rate, the inversion procedure finishes; if not, an update of the initial guess based on the temperature change magnitude is needed to repeat the inversion.

72

3.3.2 Levenberg-Marquart Algorithm

In the primary step of the interpretation procedure - Local Temperature Matching, a gradient-based method Levenberg-Marquart algorithm (Oliver et al. 2008; Tardy et al. 2011) is adopted to update the inversion parameter during each iteration.

The algorithm finds the solution when the updates of the objective function become smaller than the criteria. The objective function is defined by

$$f(x_m) = \sum_i^n (T_{cal} - T_{obs})^2 \qquad (3.2)$$

where T_{cal} is the calculated temperature, T_{obs} is the observed temperature, n is the number of temperature data points, and i is the data index, x_m denotes the inversion parameters, which can be single or multiple parameters. In this study, x_m is a vector of fracture half-lengths.

We first use the forward model described in Chapter 2 to generate temperature profile, $g(x_m)$, with an initial guess of the inversion parameters, $x_{m,i}$.

$$g(x_m) = [T_{c1}, T_{c2}, \cdots, T_{cN}]^T \qquad (3.3)$$

The vector for the observed data is

$$d = [T_{o1}, T_{o2}, \cdots, T_{oN}]^T \qquad (3.4)$$

With the two vectors, we can calculate the objective function *f(x_m)*. The procedure starts with generating the sensitivity matrix

$$G = - \begin{bmatrix} \dfrac{\partial T_{c1}}{\partial x_{m,1}} & \dfrac{\partial T_{c1}}{\partial x_{m,2}} & \cdots & \dfrac{\partial T_{c1}}{\partial x_{m,M}} \\ \dfrac{\partial T_{c2}}{\partial x_{m,1}} & \dfrac{\partial T_{c2}}{\partial x_{m,2}} & \cdots & \dfrac{\partial T_{c2}}{\partial x_{m,M}} \\ \vdots & \vdots & \ddots & \vdots \\ \dfrac{\partial T_{cN}}{\partial x_{m,1}} & \dfrac{\partial T_{cN}}{\partial x_{m,2}} & \cdots & \dfrac{\partial T_{cN}}{\partial x_{m,M}} \end{bmatrix} \tag{3.5}$$

where:

$$\frac{\partial T_{c1}}{\partial x_{m,1}} = \frac{T_{c1}(x_{m,1}+\delta x_m) - T_{c1}(x_{m,1})}{\delta x_m} \tag{3.6}$$

We need to run the forward model M times to generate the sensitivity matrix. Once we have the sensitivity matrix, we can calculate the Hessian matrix.

$$H = G^T G \tag{3.7}$$

The derivative vector for measured data and simulated data is

$$w = G^T \big(d - g(x_m)\big) \tag{3.8}$$

and this is used to calculate the upgrade vector

$$\delta x_m = -(H + \lambda I)^{-1} w \tag{3.9}$$

where λ is the damping factor and the initial value of λ for the first iteration is 1. The property vector is updated next,

$$x_{m+1} = x_m + \delta x_m \tag{3.10}$$

Now we are ready to calculate the objective function $f(x_{m+1})$ with the updated property vector based on Equation 3.2. Note here the objective function $f(x_{m+1})$ is calculated using a damping factor λ. For the first iteration λ is 1, and for the other iterations λ is a value estimated for conversion. To distinguish, we denote the updated $f(x_{m+1})$ as $f(x_{m+1})_{Current}$. First, we change λ to $\lambda_{Up}=M\lambda$ and $\lambda_{Down}=\lambda/M$ respectively, where M is a given constant number. Using λ_{Up} and λ_{Down} to solve Equation 3.9 and Equation 3.10, we

obtain the new objective function $f(x_{m+1})_{Up}$ and $f(x_{m+1})_{Down}$. We need to choose the minimum value of these three objective functions $f(x_{m+1})_{Current}$, $f(x_{m+1})_{Up}$, and $f(x_{m+1})_{Down}$ as the new $f(x_{m+1})$ of current iteration, and update λ with its corresponding damping factor.

If $f(x_m) - f(x_{m+1}) \leq \varepsilon_1$ or $\frac{f(x_m)-f(x_{m+1})}{f(x_m)} \leq \varepsilon_2$, stop the updates. Otherwise, we need to determine the new property vector by repeating from calculating the damping factor λ to recalculating objective function until the convergence criteria, $f(x_m) - f(x_{m+1}) \leq \varepsilon_1$ or $\frac{f(x_m)-f(x_{m+1})}{f(x_m)} \leq \varepsilon_2$, meet.

Figure 3.4 illustrates how the algorithm finding the solution through iterations. Since the algorithm is a gradient-based method, each iteration leads to the steepest-decent direction.
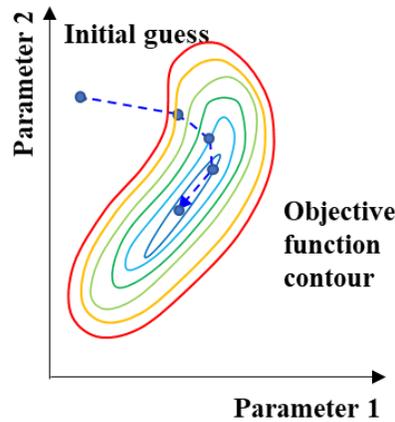

Figure 3.4 Illustration of Levenberg-Marquart algorithm

For non-linear inversion problems, the objective function may have multiple minima, as shown in Figure 3.5. If the initial guess starts from point 1 or 2, the algorithm is more likely to find the global minimum. However, if the initial guess starts from point

3, the algorithm is likely to be trapped into the local minimum and cannot obtain the global minimum. In our inversion procedure, the initial evaluation can give us a reasonable initial guess which has a higher chance to be closer to the real solution. This leads to a lower chance of trapping into the local minimum.
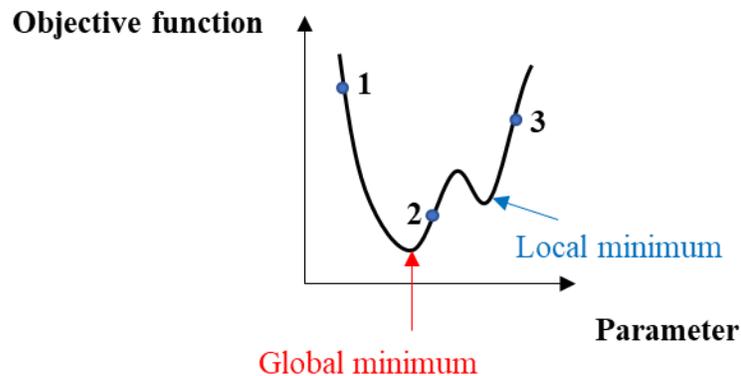
Figure 3.5 Local minimum and global minimum

3.4 Synthetic Example

In this section, a synthetic example is used to validate the effectiveness and efficiency of this interpretation procedure. Using monitored temperature interpretation only can provide a flow rate distribution. Multiple combinations of fracture geometry and fracture conductivity can result in similar temperature distribution and similar flow rate profile. To identify the fracture geometry or fracture conductivity, we need more constraints.

3.4.1 Synthetic Example Setup

The system used for the synthetic case has two fracture stages, and each stage has five clusters. The cluster spacing is 50 ft. The well is producing gas and the production

time is 120 days. The input used to build this synthetic case is given in Table 3.3 to Table 3.5. The parameters in Table 3.5 are designed carefully so that two different fracture geometries can provide us with the same flow rate and very similar temperature profile. One is that all fractures have the same conductivity but different fracture half-lengths, and the other is that all fractures have the same half-length but different conductivity. The geometries are illustrated in Figure 3.6. This example illustrates that using monitored temperature interpretation can only provide a flow rate distribution. Multiple combinations of fracture geometry and fracture conductivity can result in similar temperature distribution and similar flow rate profile. To identify the fracture geometry or fracture conductivity, we need more constraints. With all the information listed in Table 3.3 to Table 3.5, we can calculate the temperature distribution along the well (shown in Figure 3.7) and the flow rate of each fracture (given in Table 3.6). We use this temperature distribution as the "observed data" and assume we do not know the flow rate of each fracture. The objective is to interpret this "observed" temperture to generature the flow rate profile along the wellbore. These known fracture half-length, fracture conductivity and flow rate for each fracture in the synthetic example are the "True" values. In the interpretation, we can invert the flow rate for each fracture by matching the "observed data" with the forward simulation result. With additional constraint, we can further invert the fracture half-length or the fracture conductivity. The inversion results then can be compared with the "True" values to validate the interpretation procedure. In reality, we may not know either fracture half-length or conductivity. An additional constraint is

required to complete this step. The additional constraint can be distributed acoustic measurements.

Table 3.3 Reservoir properties of the synthetic example

Parameter	Value
Net pay thickness, ft	135
Reservoir depth, ft	4300
Matrix permeability, nD	580
Matrix porosity, %	12
Initial pressure, psi	4300
Initial temperature, °F	130
Total compressibility, 1/psi	1.74E-04
Bottomhole pressure, psi	2200

Table 3.4 Media properties of the synthetic example

Media	Parameter	Value
Rock	Bulk density, lbm/ft^3	148.6
	Dry thermal conductivity, BTU/hr·F·ft	2.0
	Specific heat, BTU/lb·F	0.202
	Pore compressibility, 1/psia	1.0E-06
Gas	Specific heat, BTU/lb·F	0.735
	Molecular weight, -	16
	Viscosity, cp	0.0256
	Dry thermal conductivity, BTU/hr·F·ft	1.50E-04
	Critical pressure, psi	667.17
	Critical temperature, ^{o}F	-116.66

Table 3.5 Fracture geometries of the synthetic example

Geometry	Parameter	Value
1	Fracture width, in	0.06
	Fracture height, ft	135
	Fracture half-length, ft	450, 320, 200, 230, 350, 350, 280, 200, 320, 500
	Fracture conductivity, md·ft	10, 10, 10, 10, 10, 10, 10, 10, 10, 10
2	Fracture width, in	0.06
	Fracture height, ft	135
	Fracture half-length, ft	320, 320, 320, 320, 320, 320, 320, 320, 320, 320
	Fracture conductivity, md·ft	13.44, 10.00, 4.65, 8.21, 10.07, 10.07, 9.42, 6.39, 10.00, 19.89
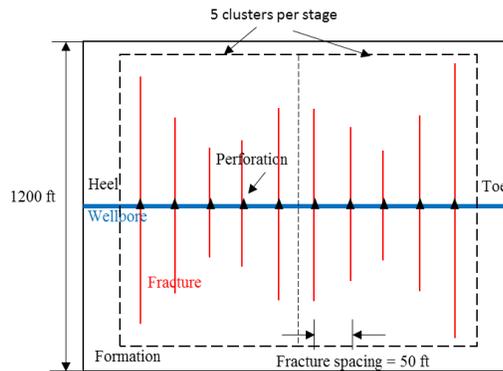
(a) Geometry 1
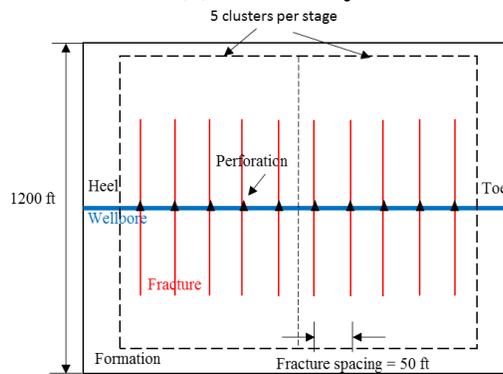
(b) Geometry 2

**Figure 3.6 Fracture geometries of the synthetic example**
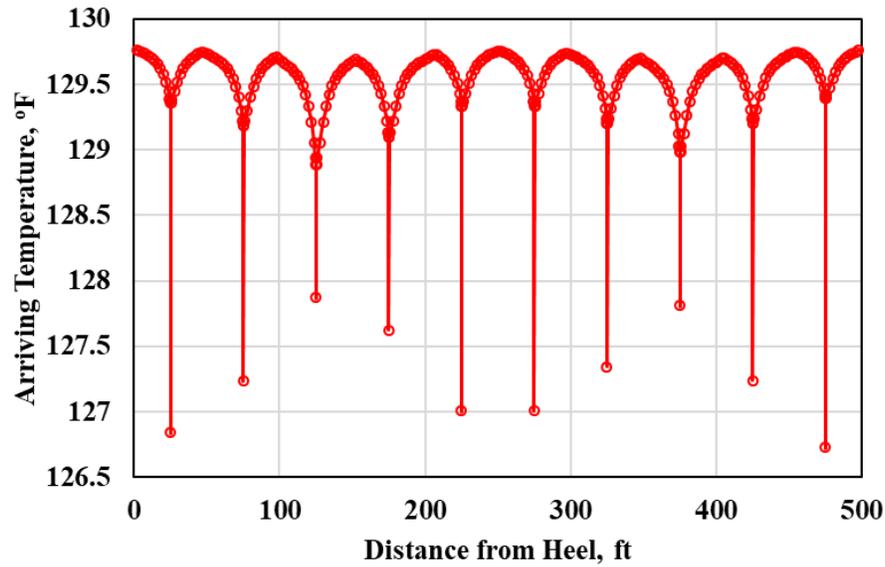
Figure 3.7 "Observed" temperature generated from synthetic example

Table 3.6 "True" flow rate

Fracture No. (from heel to toe)	1	2	3	4	5	6	7	8	9	10
Flow rate (Mscf/day)	463.3	313.5	222.6	242.0	341.8	341.8	278.5	222.6	313.5	532.4

3.4.2 Interpretation with Non-uniform Initial Guess

3.4.2.1 Geometry 1

As shown in Figure 3.7, the temperature drop at each fracture is different. According to the different temperature drop, we can start our interpretation with non-uniform initial guess. To obtain an inversion result of fracture half-length, we have to assume that the fracture conductivity is known. A lab-measured conductivity for the targeting reservoir is used as a reference in this case (McGinley et al. 2015). Figure 3.8 shows the inversion result of fracture half-length when fracture conductivity keeps

80

constant at 10 md·ft (Geometry 1). Figure 3.8(a) shows the non-uniform initial guess of fracture half-length and its values through each iteration. Each cluster requires different numbers of iterations, hence the last iteration value is the inversion result. In Figure 3.8(b), the inversion result (blue bars) holds consistent with the "true" value (red bars) with a maximum difference of 0.6%. The deviation is due to the grid block size of 2 ft. Figure 3.8(c) shows the objective function of each fracture changing as the iteration continues. We can see that the convergence is rapid and criteria meet within two to three iterations.
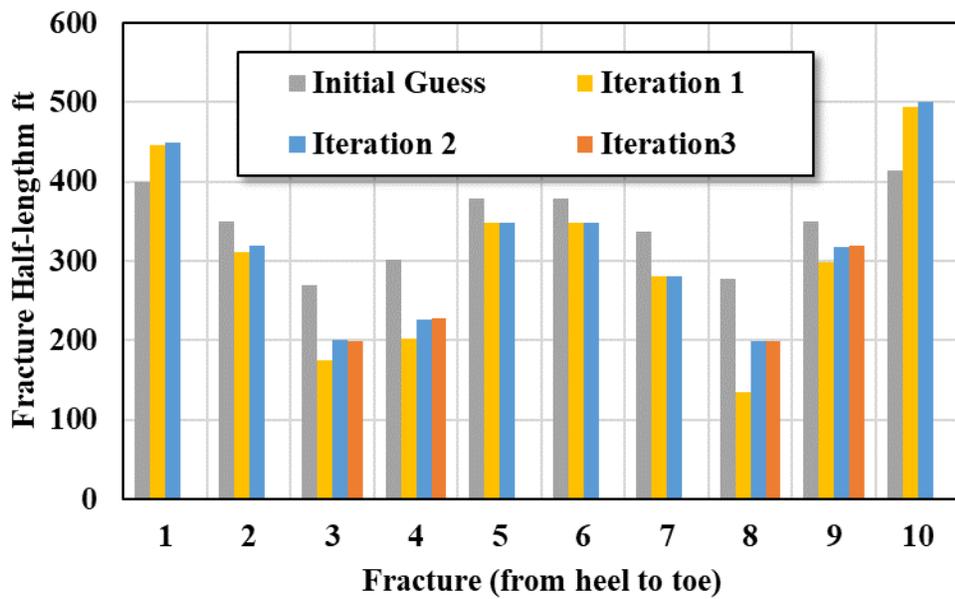
(a) **Fracture half-length for each iteration**
Figure 3.8 Fracture half-length inversion result with known fracture conductivity of 10 md·ft
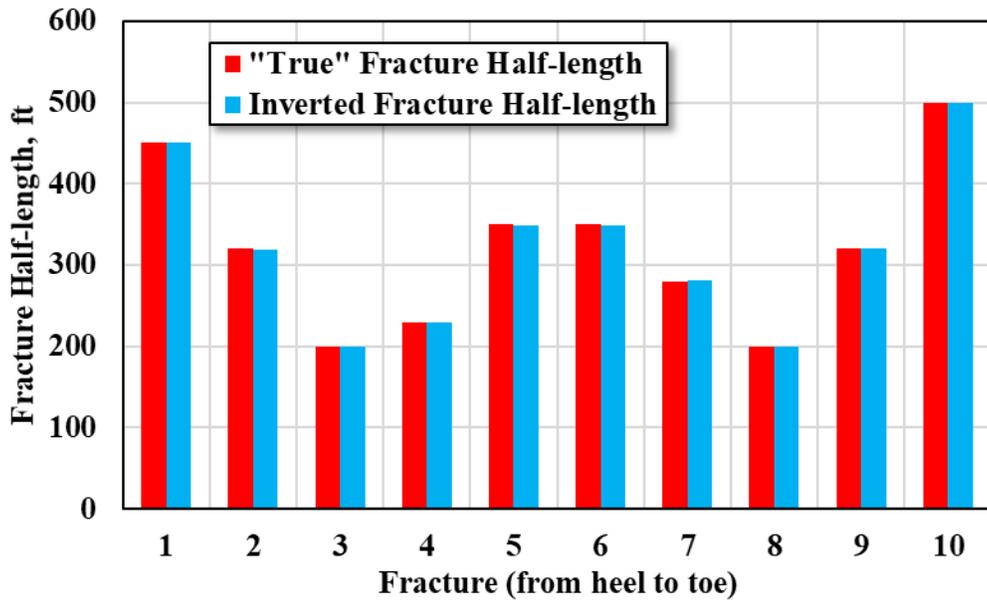
(b) Fracture half-length distribution along the wellbore
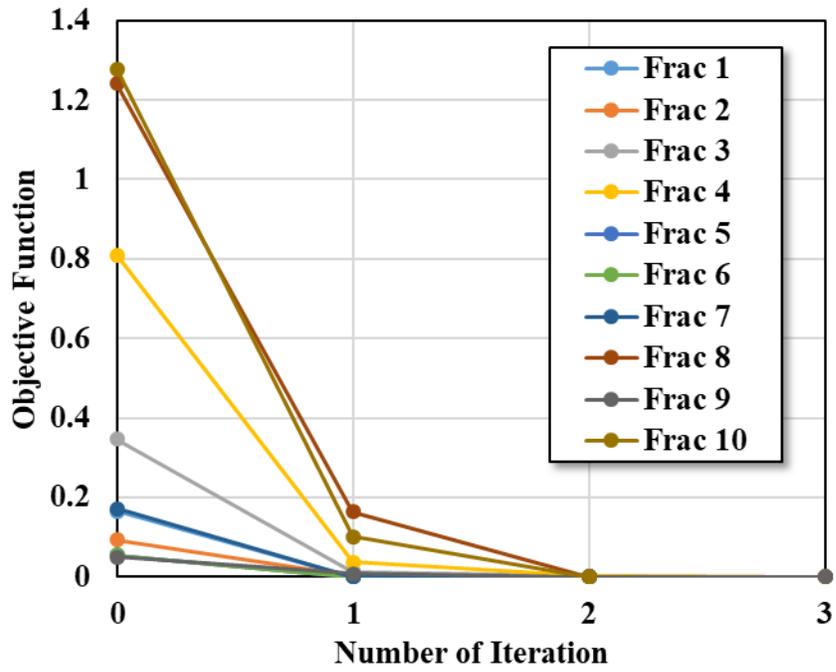
(c) Objective function changing with iterations
Figure 3.8 Continued

Figure 3.9 and Figure 3.10 present the inverted temperature and flow rate profile of this synthetic example. In Figure 3.9, the circle represents the "observed" temperature data, which is generated with a known system described before. The line is an inverted result of the temperature profile. The inversion result of temperature matches the "observed" data perfectly. In Figure 3.10, the red bars represent the "true" values of flow rate, and the blue bars represent the inversion result of the flow rate distribution. The inversion results have a good match with the "true" value.
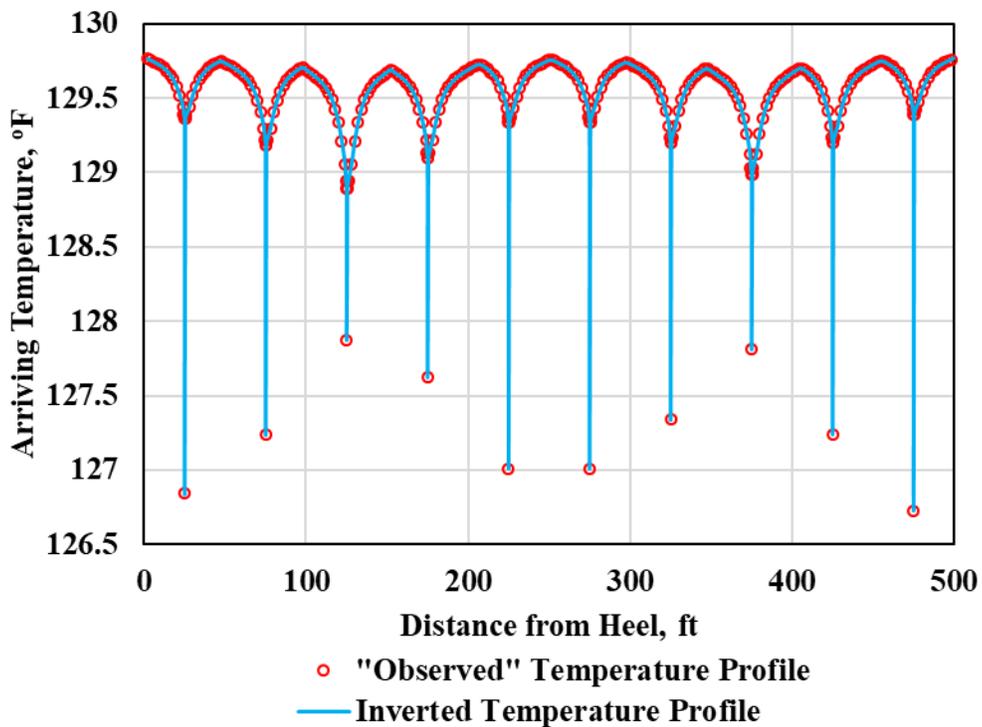
Figure 3.9 Inverted temperature distribution along the wellbore with known fracture conductivity of 10 md·ft
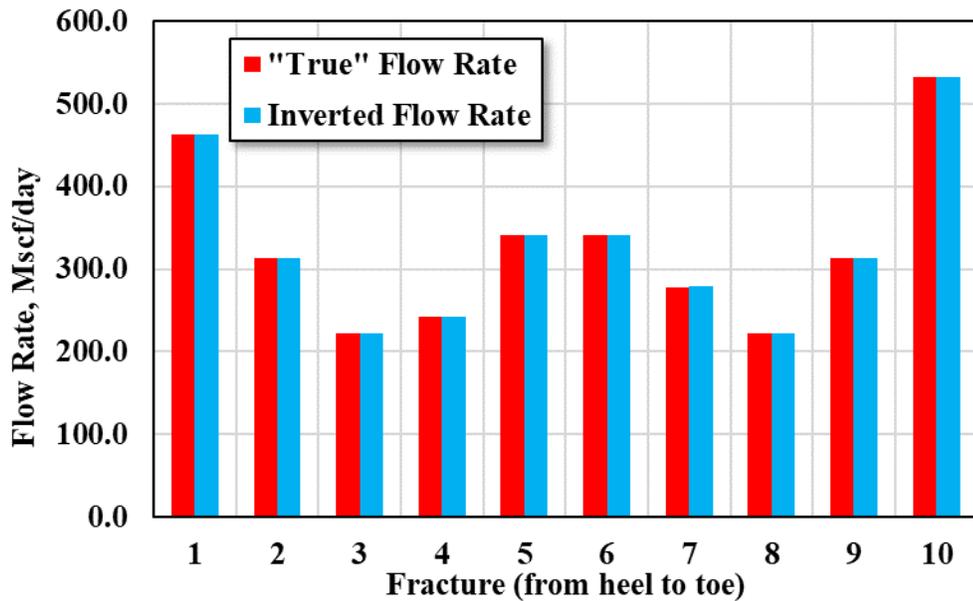
**Figure 3.10 Inverted flow rate distribution along the wellbore with known fracture conductivity of 10 md·ft**

For this example, the inversion is processed independently fracture by fracture. The simulation domain of each fracture is discretized with 16 grids along wellbore direction, 301 grids along fracture direction and 1 layer in the height direction. The time is discretized with 20 timesteps. In this single-phase example, the average time for one forward simulation is about 2.2 minutes. Within each iteration of the inversion, multiple times of forward simulations are required to compute sensitivity matrix and update the damping factor. Table 3.7 shows the inversion time for each fracture in this case for sequential computation. Sequential computation refers to inverting each fracture sequentially from Fracture 1 to Fracture 10. With parallel computing techniques, each core of the computer can run an inversion modeling for one fracture, which allows multiple

inversions running at the same time. This reduces the total computation time for this 10-fracture example to 43 min.

Table 3.7 Computation time for Geometry 1

	No. of iterations	Inversion time, min
Frac 1	2	17.47
Frac 2	2	17.86
Frac 3	3	25.90
Frac 4	3	25.81
Frac 5	2	17.01
Frac 6	2	17.36
Frac 7	2	17.34
Frac 8	3	26.48
Frac 9	3	26.11
Frac 10	2	17.92

3.4.2.2 Geometry 2

Similar to Geometry 1 interpretation, we can also invert the fracture conductivity when fracture half-length keeps constant as 320 ft (Geometry 2) with non-uniform initial guess. Figure 3.11(a) shows the initial guess of fracture conductivity and its values through each iteration, Figure 3.11(b) shows the inverted fracture conductivity comparing with the "True" value, and Figure 3.11(c) shows the objective function at each iteration. Inverting fracture conductivity also gives us a promising match although with a slightly larger error of 3% maximum and the iteration number for conversion is 3 to 4. Temperature is more sensitive to the fracture half-length change, but the fracture conductivity has a larger changing range than fracture half-length.
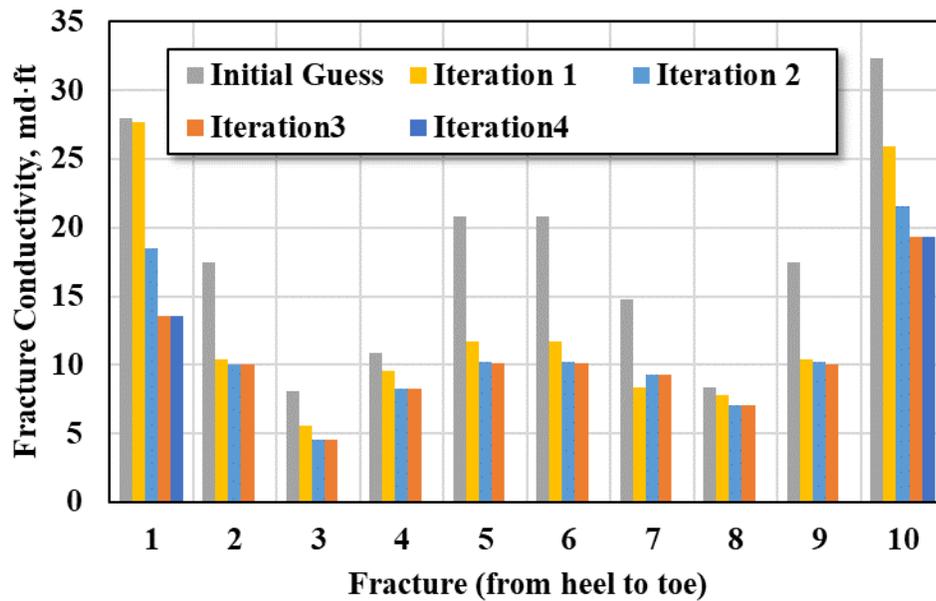
(a) Fracture conductivity for each iteration
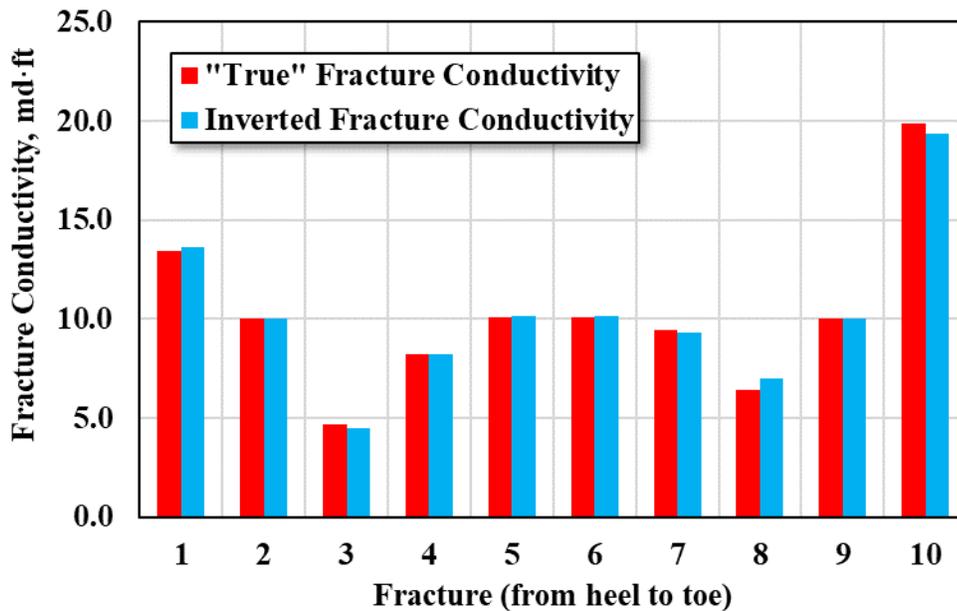
(b) Fracture conductivity distribution along the wellbore

Figure 3.11 Fracture conductivity inversion result with known fracture half-length of 320 ft
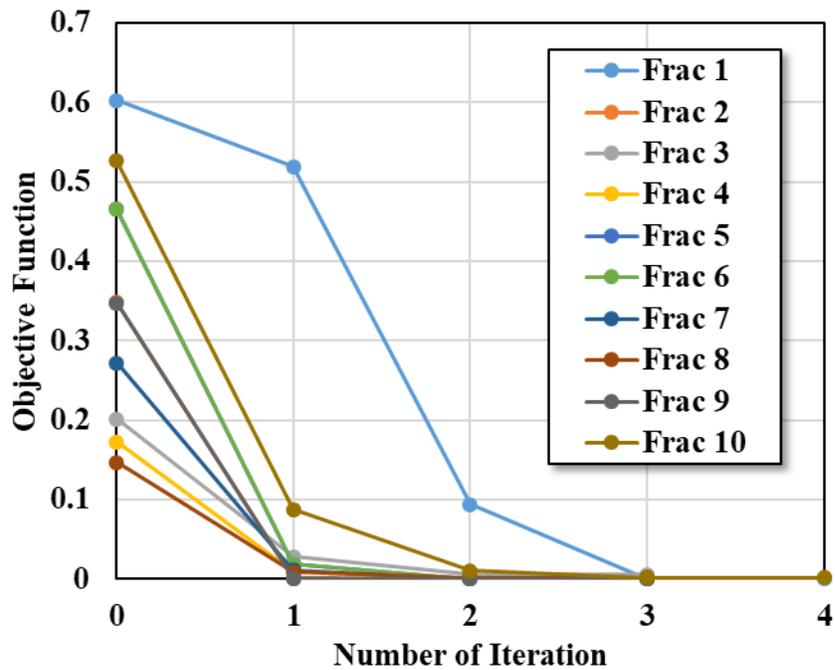
(c) Objective function changing with iterations
Figure 3.11 Continued

Figure 3.12 and Figure 3.13 show the inverted temperature profile and flow rate profile of Geometry 2. The inverted temperature profile also has a good match with the "observed" temperature. Also, the inverted flow rate holds good consistency with the "True" value with a maximum error of 1.3%. In this case, the same grids are used as in Geometry 1. Table 3.8 shows the computation time for this case when compute sequentially. In this case, the inversion needs more iterations compared to Geomery 1, thus results in a longer computation time.

Overall, the synthetic example proves its feasibility and computational efficiency of this inversion procedure using non-uniform initial guess.
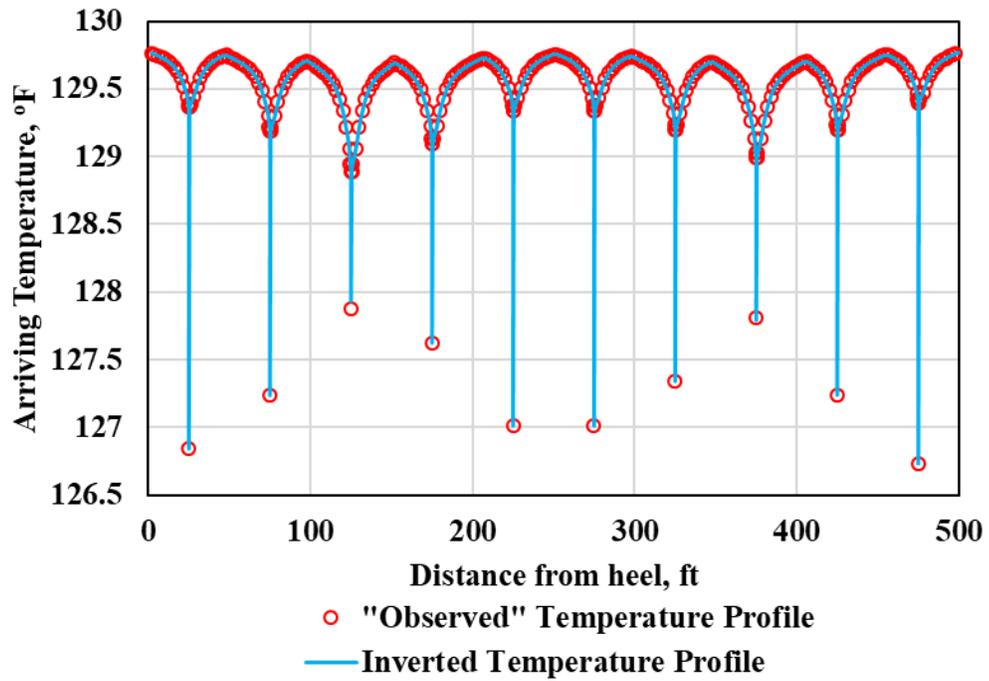
Figure 3.12 Inverted temperature distribution along the wellbore with known fracture half-length of 320 ft
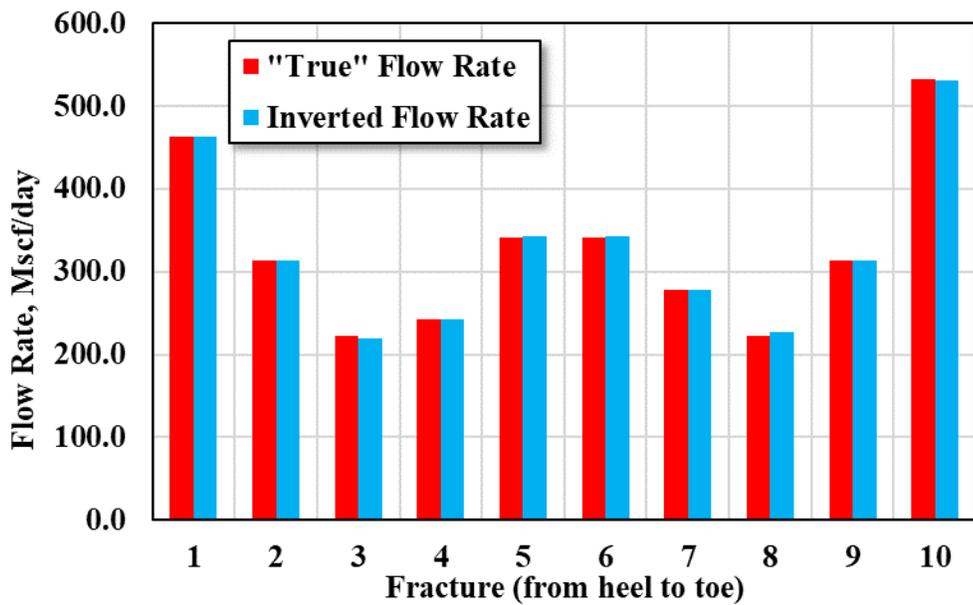

Figure 3.13 Inverted flow rate distribution along the wellbore with known fracture half-length of 320 ft

Table 3.8 Computation time for Geometry 2

|	No. of iterations	Inversion time, min
Frac 1	4	34.00
Frac 2	3	26.76
Frac 3	3	26.64
Frac 4	3	25.81
Frac 5	3	27.14
Frac 6	3	26.19
Frac 7	3	26.45
Frac 8	3	25.81
Frac 9	3	27.02
Frac 10	4	33.89

3.4.3 Interpretation with Uniform Initial Guess

In the last section, the interpretation is performed with non-uniform initial guess based on the temperature drop. For comparison purpose, in this section the same synthetic example is interpreted with a uniform initial guess as the starting point. Geometry 2 shown in Figure 3.6 is studied in this section for the comparison.

In Geometry 2, the fracture half-length is assumed as known and kept constant of 320 ft. To obtain the inverted fracture conductivity, the interpretation starts with the uniform initial guess that the fracture conductivity is 28 md·ft for all 10 fractures. The other interpretation setups are kept the same as in Section 3.4.2.2.

Figure 3.14 to Figure 3.16 show the interpretation results. Figure 3.14(a) presents the initial guess of fracture conductivity and its values through each iteration. Figure 3.14(b) shows the inverted fracture conductivity comparing with the "True" value. Figure 3.14 (c) presents the objective function of each iteration. Figure 3.15 and Figure 3.16 show the inverted temperature profile and flow rate profile. Still, the inversion reaches to an acceptable convergence and the inversion result has a satisfactory consistency with the

"True" value. Compared to the inversion result with non-uniform initial guess (presented in Section 3.4.2.2), this inversion requires 11 more iterations, which results in 34.4% increase of the computational time.
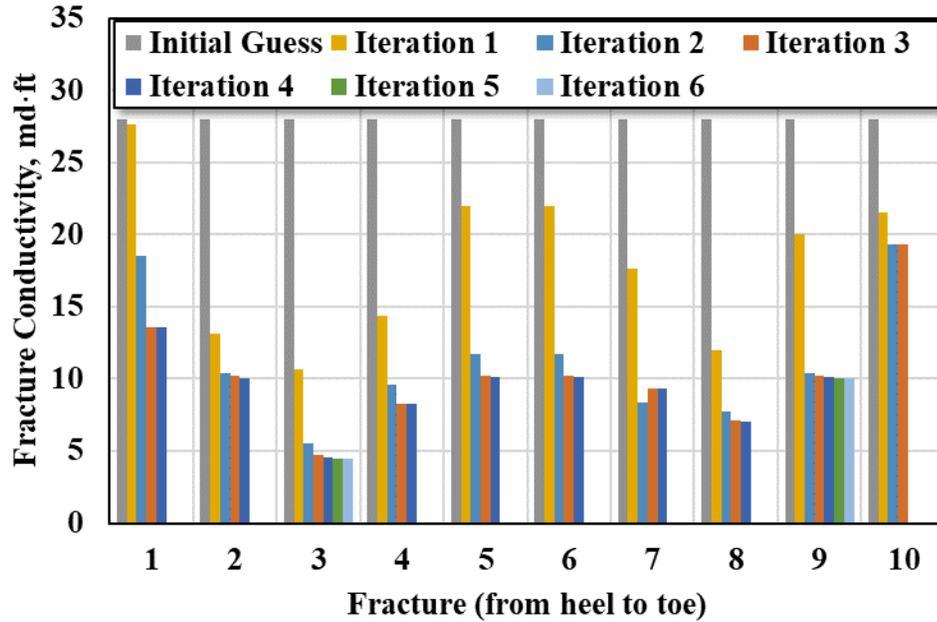
(a) Fracture conductivity for each iteration
Figure 3.14 Fracture conductivity inversion result with uniform initial guess
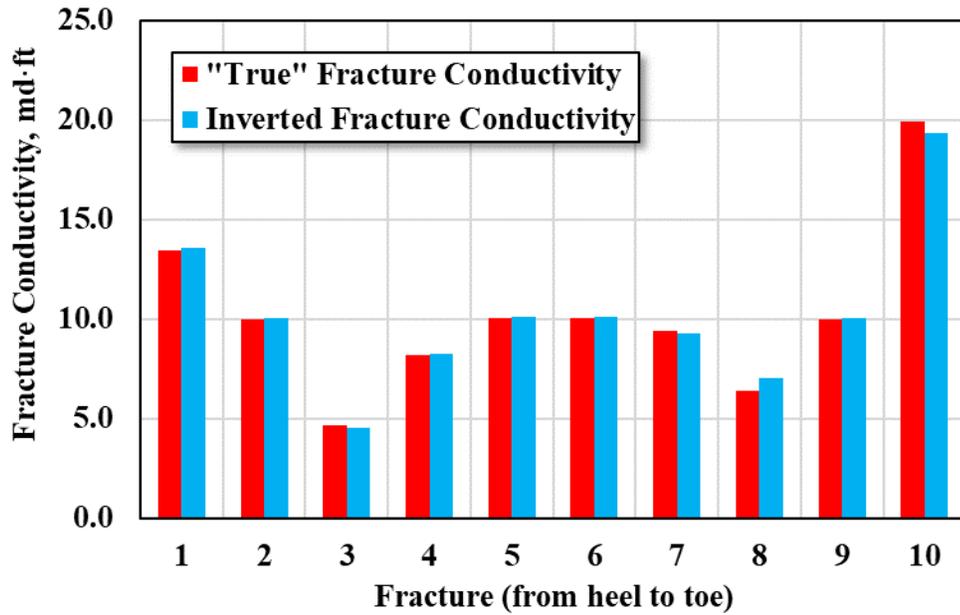
(b) Fracture conductivity distribution along the wellbore
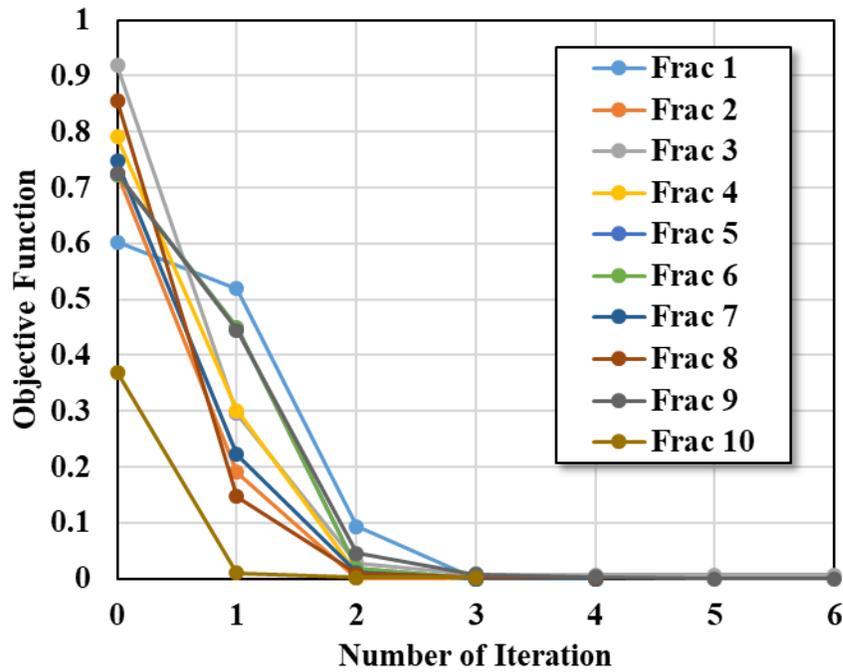
(c) Objective function changing with iterations
Figure 3.14 Continued
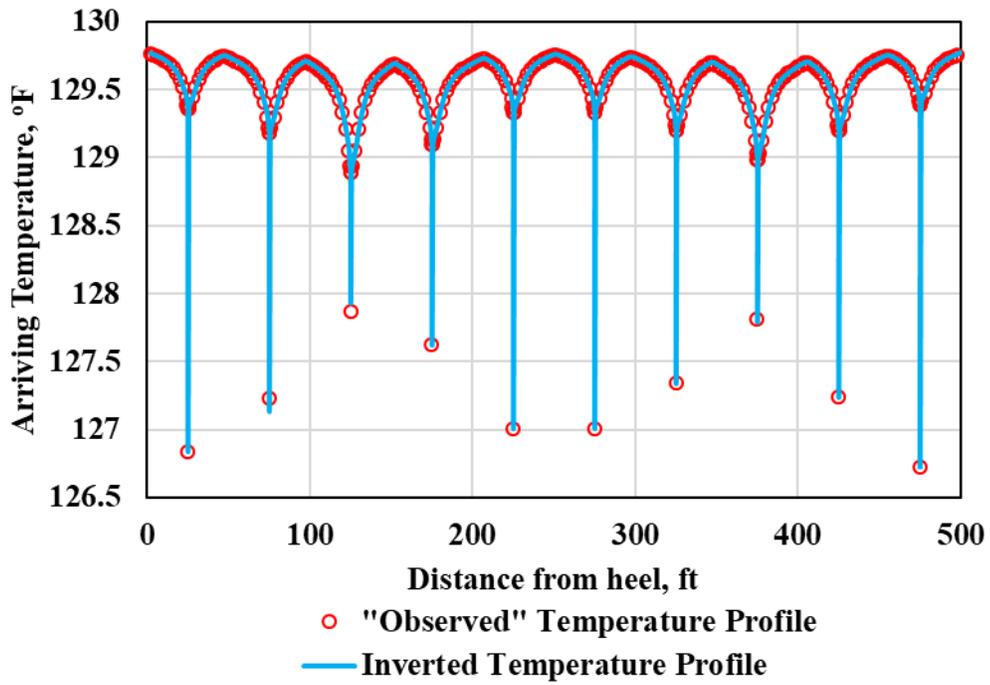
Figure 3.15 Inverted temperature distribution along the wellbore (uniform initial guess)
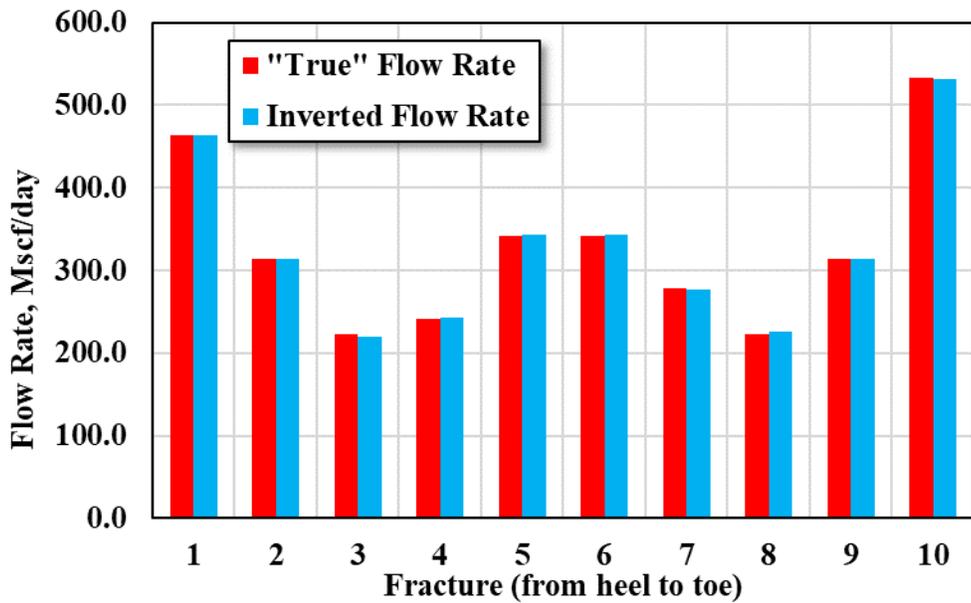
Figure 3.16 Inverted flow rate distribution along the wellbore (uniform initial guess)

3.5 Section Summary

This section presents the temperature interpretation procedure to interpret downhole temperature data for multistage fractured wells and to generate the flow rate profile. This interpretation procedure consists of four main steps including the pre-processing of the measured data, initial evaluation, local temperature matching, and global re-examination. This sensitivity study is first performed in this section to identify the most influential parameters, which are the fracture half-length, matrix porosity, and fracture permeability. The interpretation procedure is then applied to a synthetic example which proves that the inversion procedure is feasible as a promising tool to interpret downhole temperature data quantitatively.

CHAPTER IV

APPLICATION I: SINGLE-PHASE GAS PRODUCTION DIAGNOSIS

4.1 Introduction

The temperature interpretation procedure proposed in Chapter 3 is applied to a field case. This is a horizontal well with multiple fractures which is producing gas. When gas is entering the wellbore, temperature decreases sharply because of the Joule-Thomson effect. This chapter explains how to use this temperature phenomena to eliminate the non-producing fractures from the inversion problem, which can help to reduce the problem size and increase computational efficiency. This field case illustrates how to apply the general interpretation procedure to the gas producing well and interpret the downhole temperature measurement to a flow rate distribution.

4.2 Well Information

The well is a part of the study by Marcellus Shale Energy and Environment Laboratory (MSEEL) initiated by the Department of Energy (MSEEL 2019). The well is producing from Marcellus Shale near Morgantown in West Virginia to provide a long-term field-testing site for developing and validating the new technology. Figure 4.1 shows the location of the well. The depth of producing zone is about 7400 ft below the surface.
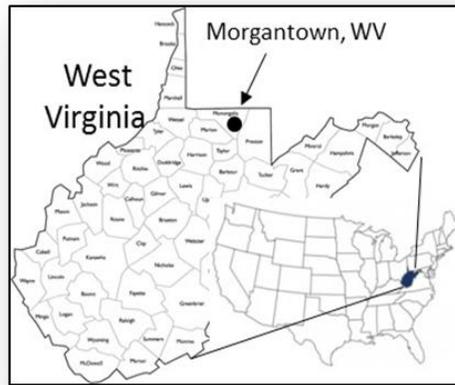
Figure 4.1 Location of the well (reprinted from (MSEEL 2019))

The horizontal well is completed with 28 stages, and each stage consists of four or five clusters. Figure 4.2 shows the well trajectory and cluster locations. Each triangle represents a cluster. The stage is labeled in the figure.
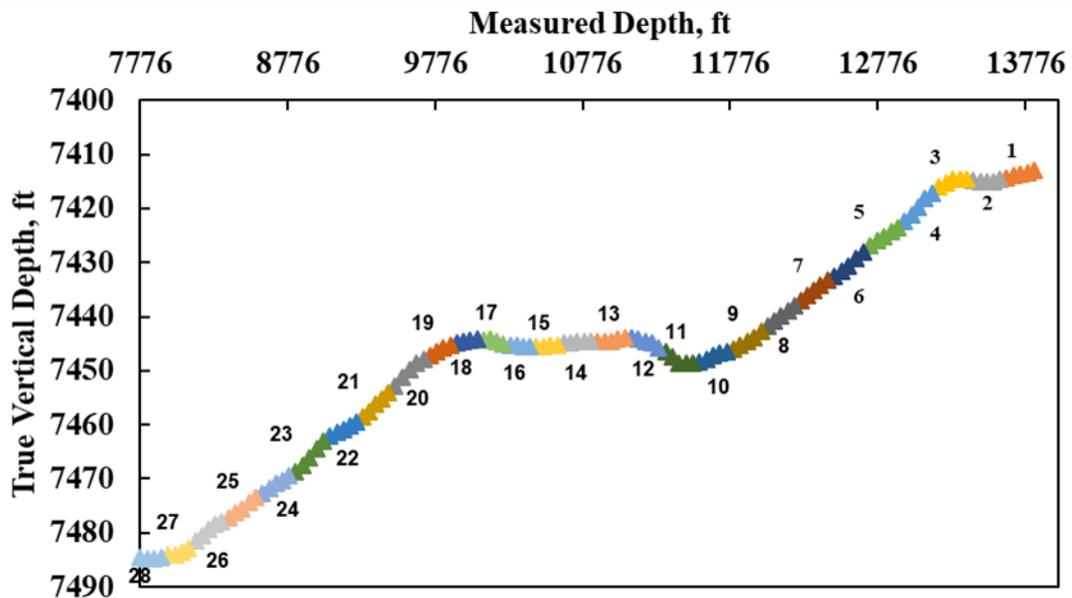

Figure 4.2 Well trajectory and perforation locations (redrawn from (MSEEL 2019))

The well is divided into five different sections, and different completion practice is applied to different section. Table 4.1 presents the details of the completion design of this well. The perforation diameter is the same for all the stages, which is 0.42 inches. The well is stimulated by hydraulic fracturing. The injection time of each stage varies from 80 minutes to 100 minutes.

Table 4.1 Well completion design (reprinted from (MSEEL 2019))

Section	Stage	Cluster Count	Total Shot Count	Shot Density (shot/ft)	Stage Length (ft)	Pumping rate (bpm)
	28	4	40	6	191	94
	27	4	40	6	184	93
	26	5	40	6	225	100
E	25	5	32	6	231	99
	24	5	30	6	222	100
	23	5	40	6	237	100
	22	5	40	6	220	93
D	21	5	40	5	218	95
	20	5	40	5	240	100
	19	4	32	6	180	99
	18	4	32	8	180	92
	17	4	32	6	181	79
C	16	4	26	6	178	78
	15	4	26	6	186	80
	14	5	30	6	228	100
	13	5	30	6	230	95
	12	5	50	5	231	99
	11	5	50	5	232	100
B	10	5	50	5	227	100
	9	5	50	5	237	99
	8	5	50	5	222	100
	7	5	50	5	224	87
	6	5	50	5	245	89
	5	5	50	5	234	89
A	4	5	50	5	230	100
	3	5	50	5	238	85
	2	5	50	5	223	88
	1	5	50	5	223	80

The horizontal well is producing gas at a flow rate of 1.83 MMSCF/Day at 180 days of production. The water production is 0.78 bbl/Day, which is a tiny volume fraction. Since water production is negligible, we assume a single-phase gas production in temperature interpretation. A fiber optic cable was permanently installed outside the casing to measure the temperature distribution along the wellbore. Figure 4.3 shows the measured temperature distribution along the wellbore by the fiber optic sensor. The interpretation considers the effects of geothermal temperature on the measured temperature behavior due to wellbore trajectory.
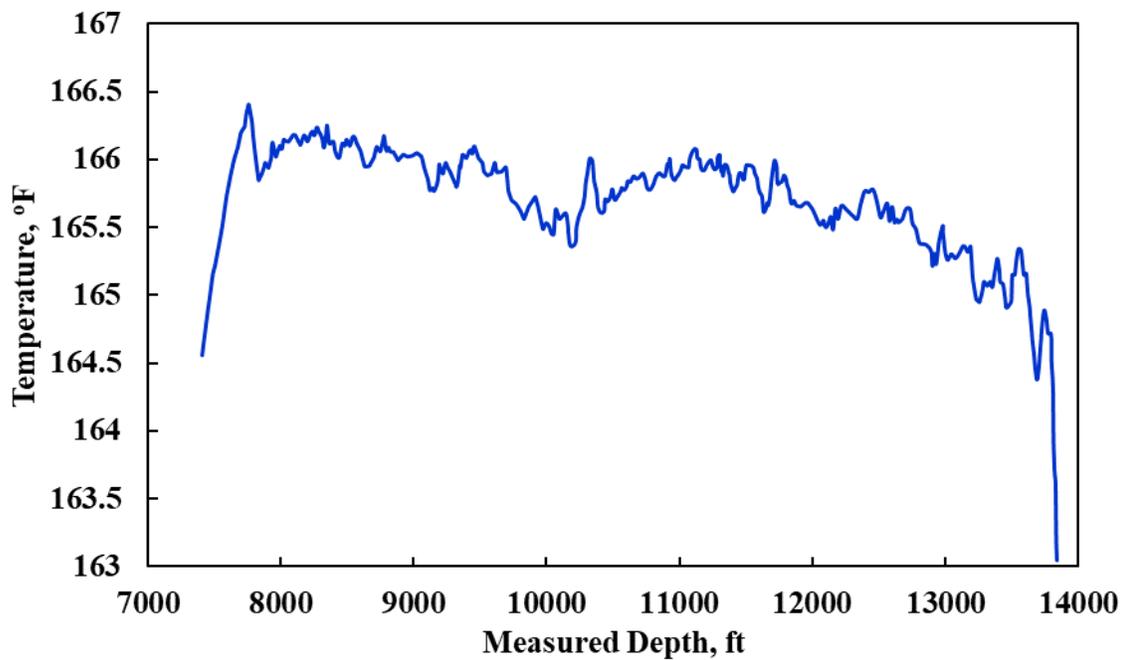

Figure 4.3 Measured temperature profile (redrawn from (MSEEL 2019))

4.3 Interpretation Results

The general temperature interpretation procedure presented in the last chapter can be applied to this field case. The details for each step are explained in the following.

4.3.1 Initial Fracture Diagnosis

For this gas producing well, we can first diagnose the clusters that are contributing to production based on the temperature behavior. Under the most common conditions, gas has a Joule-Thomson cooling effect, which causes a sharp temperature decrease at the location where the gas is entering the wellbore. Defining the temperature gradient along wellbore as the temperature derivative to distance (shown in Figure 3.3 in the last chapter), the temperature gradient at the gas production locations are negative. If the cluster does not contribute to production, the heat conduction between the reservoir and the fluid in the tubing will heat the fluid, resulting in a temperature increase and therefore a positive gradient. Based on this principle, we can diagnose which fracture is contributing to production and which is not. As illustrated in Figure 4.4, Fracture 1 is a producing fracture while Fracture 2 is a non-producing fracture. By the fracture diagnosis, the clusters that do not contribute to production can be eliminated from interpretation and assigned a zero flow rate. Only the flow rate for those clusters that contribute to production will be further inverted. This method can reduce the problem size and save computation time.
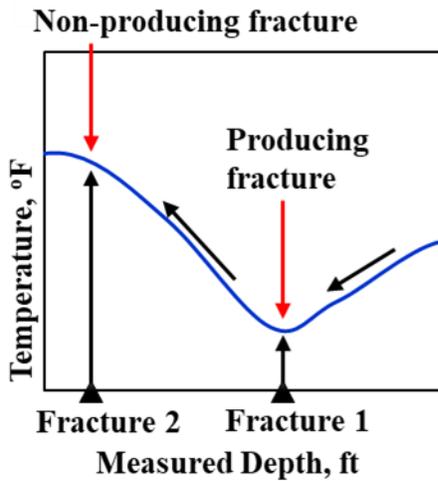
Figure 4.4 Illustration of fracture diagnosis

Based on the principal mentioned above, the fracture diagnosis is performed for this well. Figure 4.5 shows the temperature gradient at the cluster location. The negative temperature gradient indicates a temperature decrease from the near-toe side to the near-heel side. This temperature behavior indicates the gas flow as it comes into the wellbore. Hence, at these cluster locations, fractures are contributing to production, which is represented by the green bars in Figure 4.5. On the other hand, the cluster locations with the positive temperature gradient are marked as "non-producing clusters" since the temperature is increasing by the surrounding reservoir with higher temperature, and no Joule-Thomson cooling by gas entering the wellbore. According to the diagnosis, we can see that the cluster efficiency of this well is about 60%.
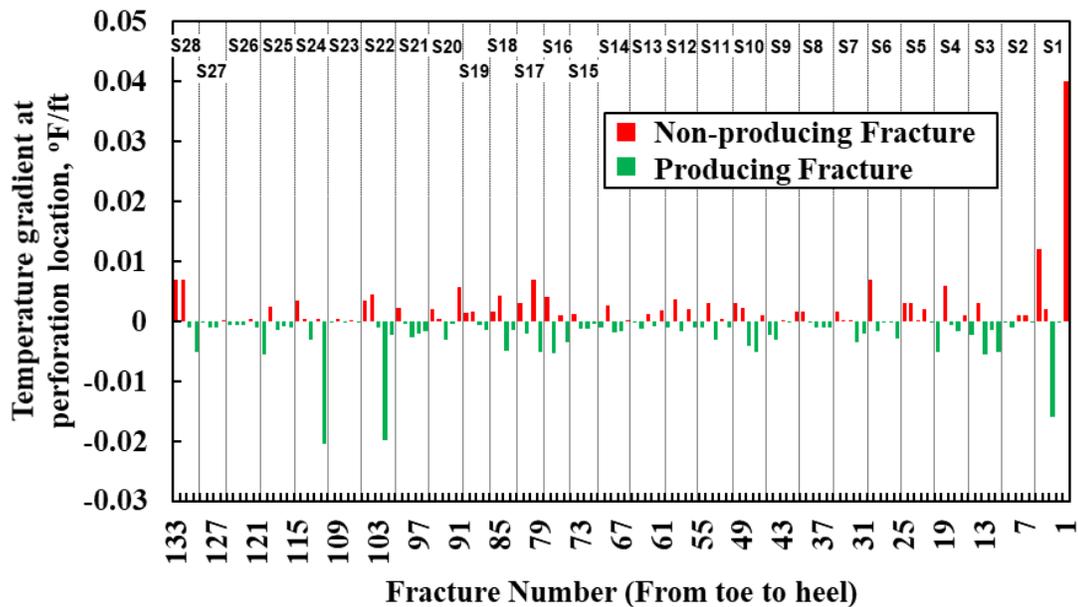
Figure 4.5 Fracture diagnosis

4.3.2 Non-uniform Initial Guess of Flow Rate Profile

Once we identify the producing fractures, we can further assign the initial guess of flow rate to each existing fractures based on the level of temperature drop. This step is done by assuming that for all producing fractures, the production rate is proportional to how much the temperature drop is, and the total production rate from all producing fractures must be equal to the surface production rate from the well. As illustrated in Figure 4.6, Frature 2 has a more significant temperature drop in comparison to Fracture 1. Hence, a larger flow rate should be assigned to Fracture 2. Although the temperature behavior has a much more complicated relationship with the flow rate for each producing fracture, this initial estimation provides a reasonable start point for the following inversion procedures. A reasonable initial guess can lead to a fast convergence, a less chance of trapping in the local minimum, and a sensible final solution. This is because with a

100

reasonable initial guess, the start point of the inversion is more likely to be closer to the

global minimum compared to the random start point.
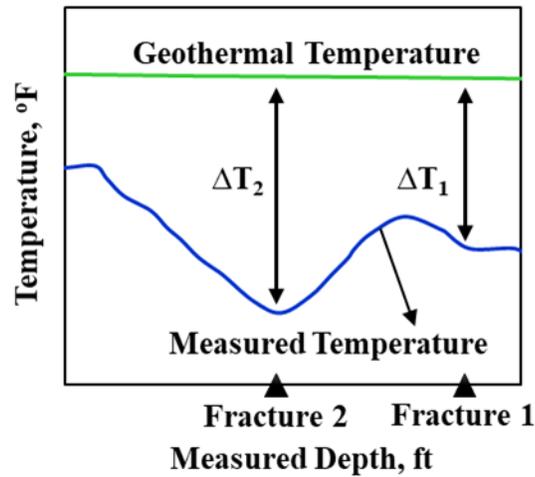
Figure 4.6 Illustration of the initial evaluation
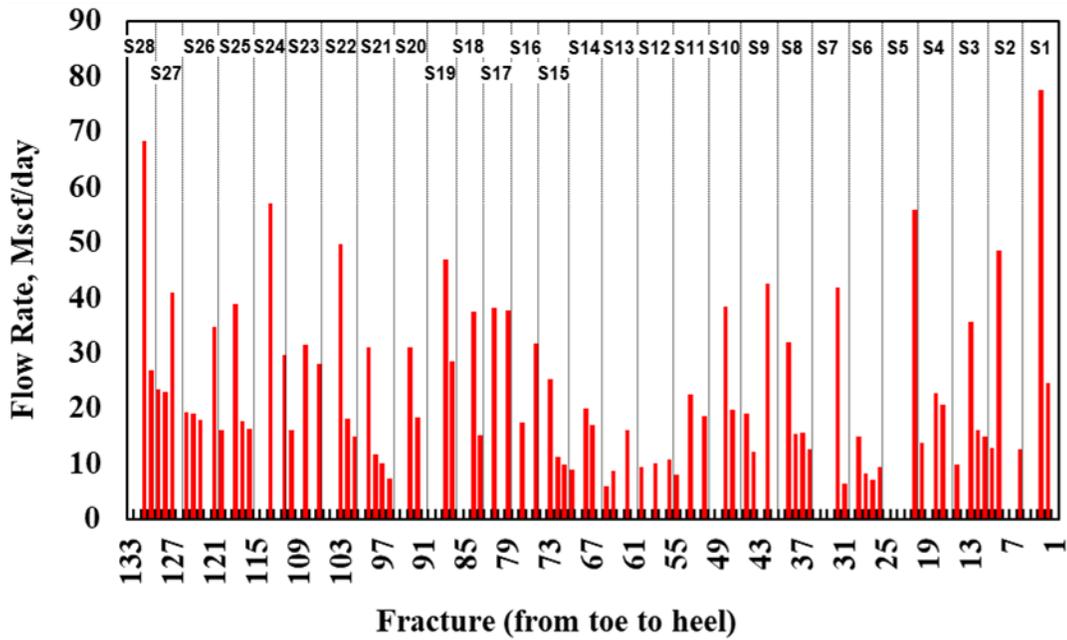
Figure 4.7 Initial guess of flow rate

Based on this principle, a non-uniform initial guess of flow rate distribution is evaluated for all producing fractures, as shown in Figure 4.7. At the non-producing cluster locations, the flow rate coming into the cluster is 0, and we skip these cluster locations in the inversion procedure. At the producing cluster locations, we assign different initial flow rate according to the temperature drop magnitude.

4.3.3 Interpretation Results

With the first step in the inversion procedure being to eliminate all non-producing fractures and assign the non-uniform initial guess of flow rate, the inversion is further performed fracture by fracture independently. In this field case, the fiber optic cable is permanently installed outside the casing. The temperature behavior can be approximated with an assumption that temperature is only influenced by the fluid from the fracture. In this case, we can use the parallel computing technique to invert more than one fractures at the same time, which can dramatically reduce the computational time. On the other hand, if temperature sensors are installed inside the wellbore, the inversion should be done from the toe of the well, with one fracture at a time, and consecutively marching towards the heel of the well. The mixing of in-coming cold fluid from the fractures and the upstream warm fluid inside the wellbore smears the temperature drop.

In this field case, 78 out of 133 clusters are producing. The inversion is performed independently for each cluster. Figure 4.8 shows the iterations of the inversion for several representative fractures. The convergence is rapid within several iterations.
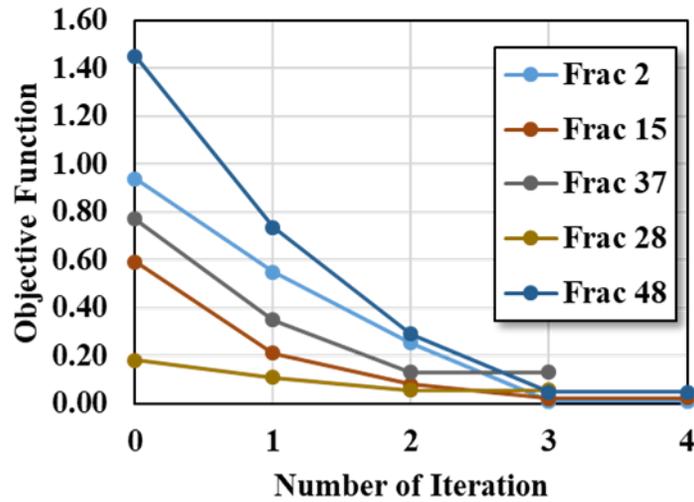
Figure 4.8 Inversion convergence

Figure 4.9 shows the inversion results of the flow rate profile. The blue bars represent the inversion results, which are compared with the initial guesses of flow rate profile (represented by the red bars). The nonuniform initial guess based on the temperature drop provides a reasonable estimate, and the inversion results have a similar trend as the initial guess. The flow rate distribution for each cluster in the heel and toe stages is more uneven than the middle stages. Some clusters produce more fluid than the others in these zones. In contrast, at the center of the well, stages 11 to 15 have more evenly distributed flow rate, but each cluster produces a smaller amount of gas compared with the end-stages.
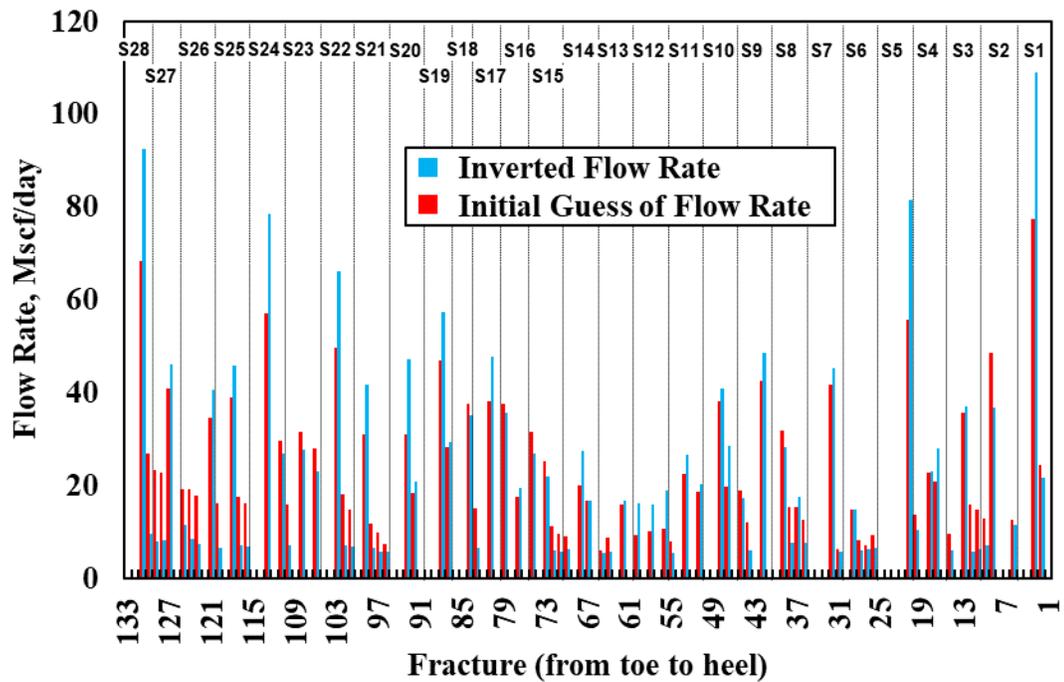
Figure 4.9 Inverted flow rate profile

Figure 4.10 shows the matched temperature and cumulative flow rate distribution. The color-coded triangles indicate the location of the clusters, and each color represents a stage. The figure shows a good match between the inversion temperature and the measured data. The brown line shows the cumulative flow rate along the well. The inversion total flow rate of the well is 1.82 MMSCF/D which matches the real flow rate of 1.83 MMSCF/D with a difference of 0.5%.
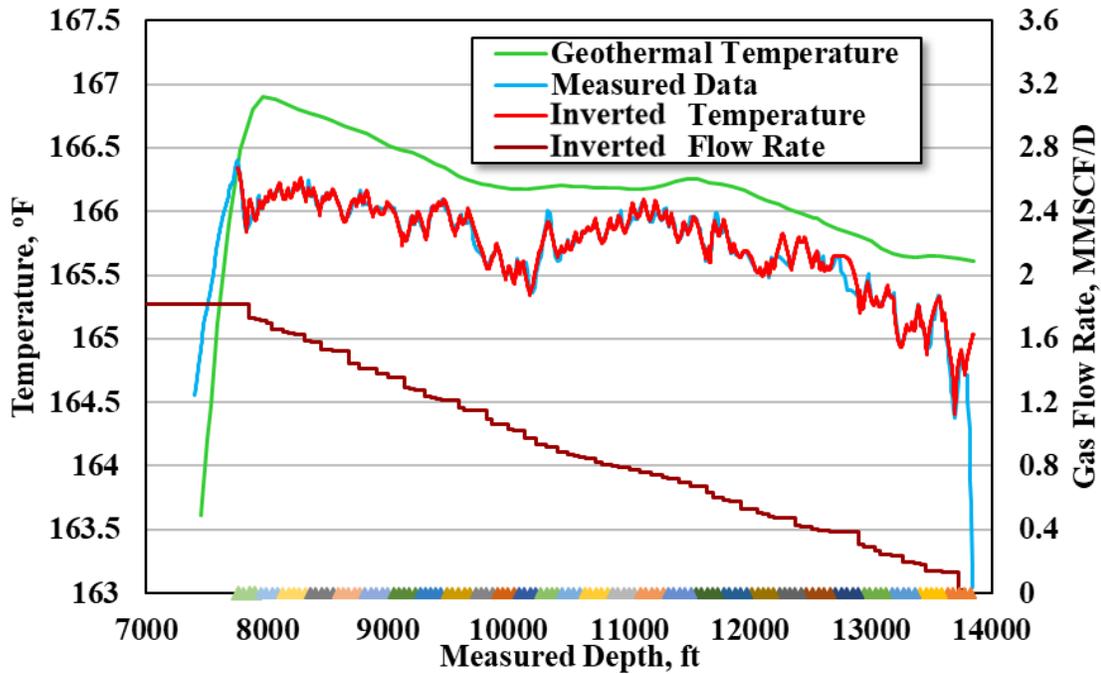
Figure 4.10 Inverted temperature and flow rate

4.3.4 Discussion

In Figure 4.9, the initial guess of flow rate is based on the assumption that the production rate of the fracture is proportional to how much the temperature drop is, and the total production rate from all producing fractures must be equal to the total production rate from the well. Hence, the initial guess of flow rate for each producing fracture is estimated based on the relationship:

$$\frac{q_{ini}}{q_{total}} = \frac{\Delta T}{\Sigma(\Delta T)} \qquad (4.1)$$

where ΔT is the temperature drop at the producing fracture location, $\Sigma(\Delta T)$ is the summation of the temperature drop for all the producing fractures, q_{ini} is the initial guess of each producing fracture, and q_{total} is the total production rate.

Comparing the initial guess of flow rate with the inverted flow rate, as shown in Figure 4.9, we observe that the initial guess for some of the fractures with relatively high production rate tends to underestimate the flow rate, while the initial guess for some of the fractures with low production rate tends to overestimate the flow rate. To find a better correlation to estimate the the flow rate for each producing fracture based on the temperature drop, the inversion result of the flow rate is analyzed with the temperature drop for each producing fracture. Figure 4.11 plots the inverted flow rate percentage versus the temperature drop percentage for each producing fracture. From this observation, we can obtain a correlation as the following:

$$\frac{q_{ini}}{q_{total}} = 19 \times \left[\frac{\Delta T}{\Sigma(\Delta T)}\right]^2 + 0.7009 \times \frac{\Delta T}{\Sigma(\Delta T)} - 0.0005 \qquad (4.2)$$

The constants in this correlation should be related to many parameters such as reservoir properties, well properties, and fluid properties.
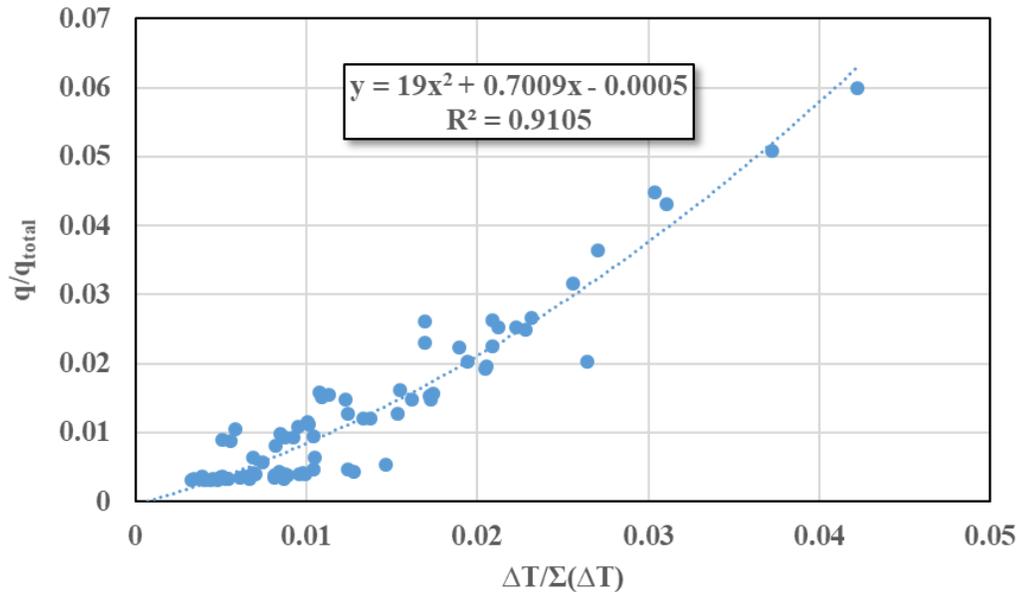
Figure 4.11 Relationship between the temperature drop and inverted flow rate for each producing fracture

Instead of using the relationship shown in Equation 4.1 to estimate the initial guess of flow rate based on the temperature drop, if we use the relationship shown in Equation 4.2, we can obtain a new estimation of initial guess of flow rate which is represented by the black bars in Figure 4.12. For most of the fractures, the new estimation gives a closer initial guess of flow rate to the inverted flow rate compared to the linear estimation. However, more studies are needed to quantify the constants in the quadratic relationship.
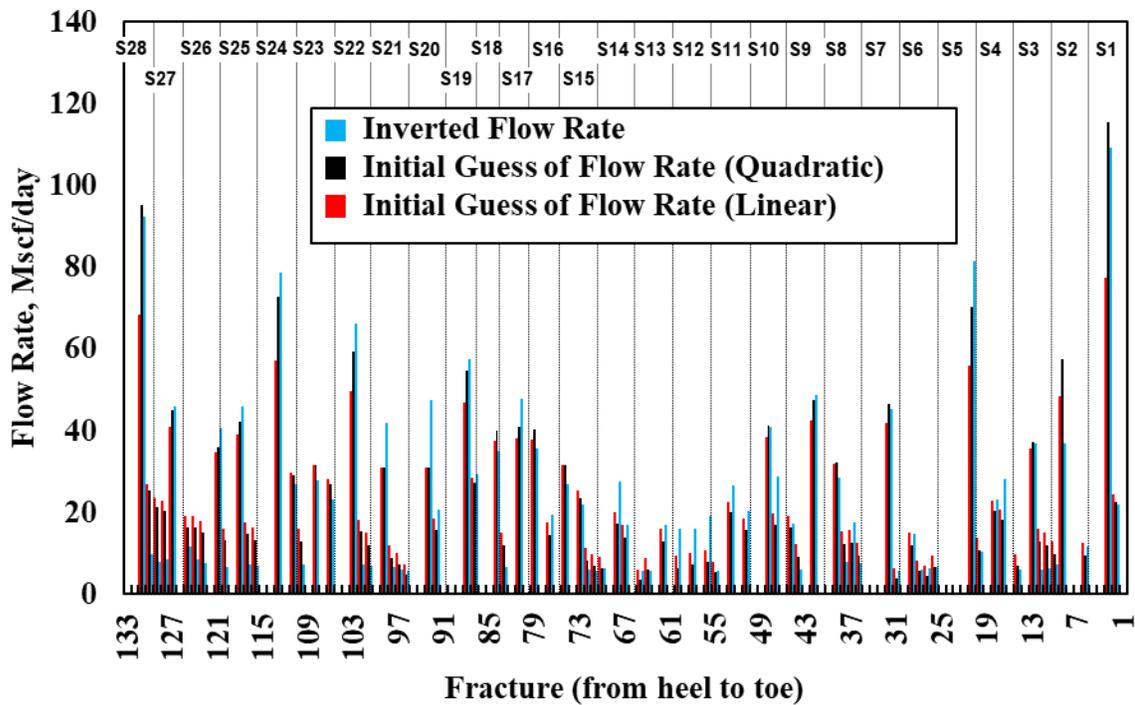
Figure 4.12 New initial guess of flow rate

4.4 Section Summary

In this section, a field case with a multi-stage hydraulic fractured horizontal well producing single-phase gas is presented to show how to apply the general temperature interpretation procedure. The initial evaluation to eliminate the non-producing fractures

in inversion procedure reduces the problem size and improves the computational efficiency, and the non-uniform initial guess leads to faster convergence and ensures a gradient method for inversion being used without local minimization trap.

With one set of temperature measurement, only flow rate distribution can be interpreted from the DTS measurement. The examples showed successful interpretation with acceptable error and computational efficiency. To further interpret the fracture half-length or conductivity, additional constraints or information is needed, such as lab data or DAS data.

CHAPTER V

APPLICATION II: TWO-PHASE OIL/WATER PRODUCTION DIAGNOSIS

5.1 Introduction

During the production of horizontal wells with multiple fractures, interpretation of temperature measurements can help to allocate the flow rate for each fracture along the wellbore quantitatively. In the last chapter, the developed general interpretation procedure has been successfully applied to the temperature interpretation for the gas-producing well during the production period. The strong Joule-Thomson effect of gas flow makes temperature interpretation viable for flow profiling. However, for multi-phase liquid-dominant production, it is still challenging to interpret temperature measurements for production rate profile. The main challenges include: The Joule-Thomson effect of liquid (water and oil) is small, and the small temperature change may not be enough to overcome the noise with the measurements for accurate interpretation; more unknown parameters and more uncertainties compare to single-phase flow; the similarity between thermal properties of water and oil.

Consequently, this chapter proposes a modified interpretation workflow particularly for liquid production based on the previous study in the last chapter and presents a field example of implementing this developed interpretation workflow to interpret temperature data to flow rate profile for a multistage fractured horizontal well with the multiphase flow quantitatively with reasonable assumptions. In the field example presented in this chapter, the temperature measurements are from the production logging

tool (PLT). The following sessions discuss the workflow in detail and show the interpretation results.

5.2 Well Information

A horizontal well is located in the Argentina. This well is targeting the formation at around 3000-meter true vertical depth, with a lateral about 1500 meters long. The well is completed with plug-and-perf, with a casing outer diameter of 4.5 inches. The horizontal well is stimulated with multi-stage hydraulic fracturing. It was planed with 18 stages, but for operation reason, Stage 7 was canceled, and Stage 19 was added. Each stage has three clusters, and the cluster spacing is about 20 meters, the cluster width is 1 meter. Figure 5.1 shows the well trajectory of the lateral. The triangles locate the clusters, and each color represents a stage.
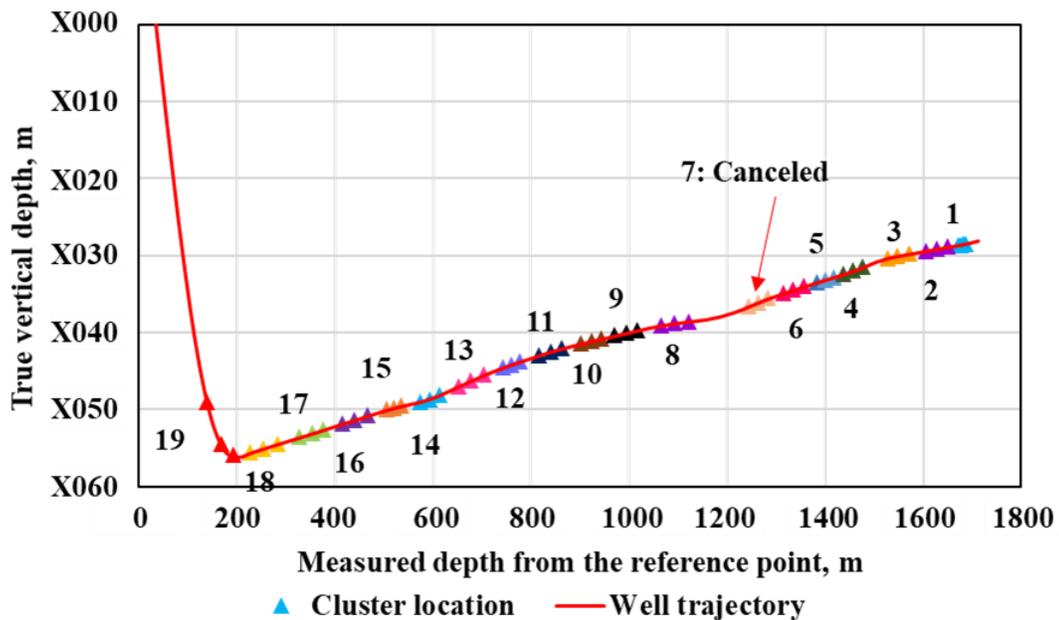

Figure 5.1 Well trajectory and perforation locations

110

During the hydraulic fracturing treatment of the well, the pumping schedule varies slightly for different stages. In general, the injection time varies from 80 minutes to 120 minutes per stage, and the injection rate is about 80 bpm. After the hydraulic fracturing of the entire well, the well was shut-in for about 48 days until it starts producing. The well is operating at a bottomhole pressure of 504 kg/cm^2, which is above the bubble point (205 kg/cm^2 according to the PVT report), the main produced fluid at downhole is oil with some water. PLT was run after the well was fractured and produced for 71 days in half of the lateral near the heel. There were three runs for PLT. At the time of logging, the average surface production rate is 13343 m^3/day of gas, 86 m^3/day of oil and 18.2 m^3/day of water. We convert this surface production rate to the downhole condition, which results in 132 m^3/day of oil and 18.2 m^3/day of water. There is no gas at the downhole condition. The oil formation volume factor is 1.53 according to the PVT report, and the water formation volume factor is assumed as 1. Figure 5.2 is the temperature measurements from three down passes of this production logging. The data is available from Stage 9 to Stage 19. In this work, we choose the first down pass temperature to interpret the flow profile because the temperature anomalies would be smeared over great distance during the up passes, which reduces the resolution (Hill 1990). We calculate the geothermal temperature based on the well trajectory, local temperature, and general geothermal temperature gradient of the targeting area, which is about 3.1ºC/100m. The calculated geothermal temperature is further calibrated with the information from the PVT report. The geothermal temperature and the measured temperature for interpretation (the first down pass temperature) are shown in Figure 5.3.
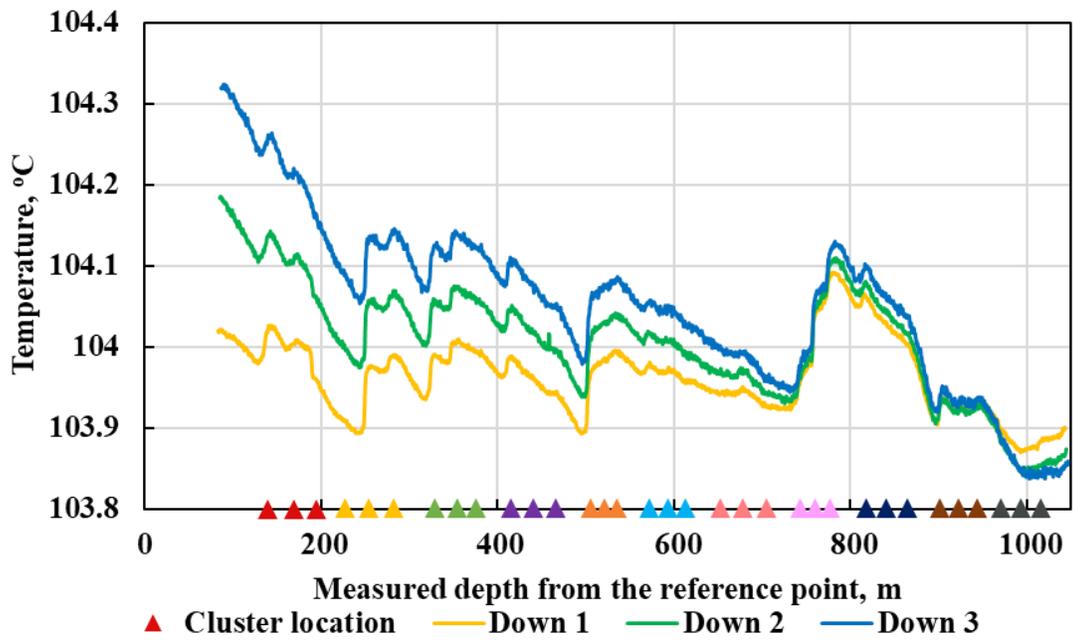
Figure 5.2 Temperature measurements from the production logging tool
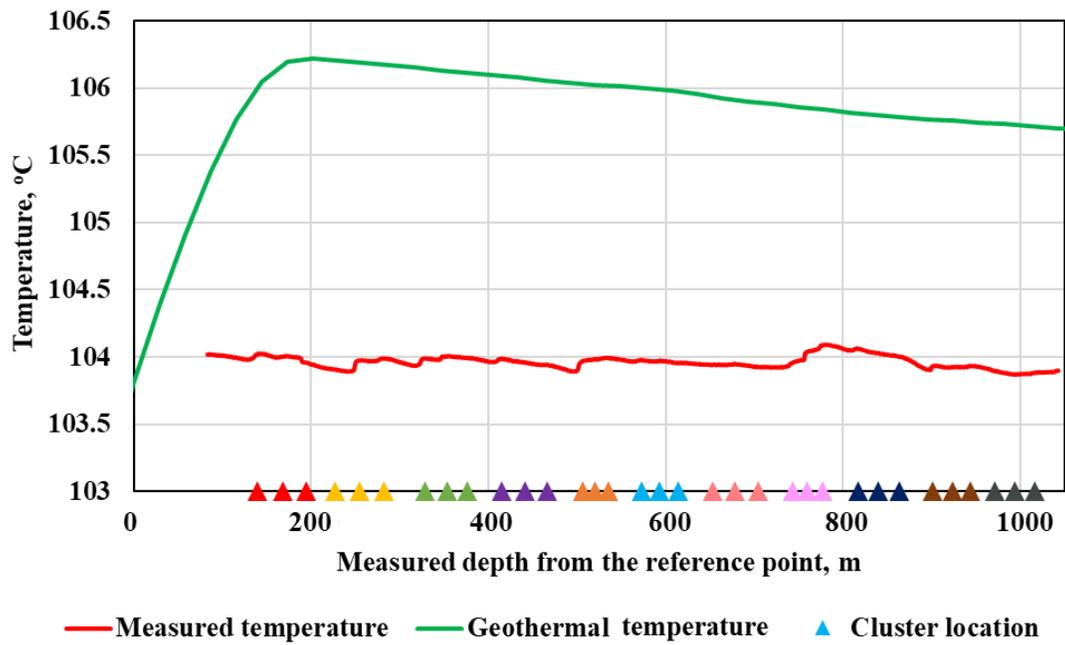
Figure 5.3 Geothermal temperature and the measured temperature

5.3 Modified Interpretation Methodology and Results

5.3.1 Interpretation Model Setup

To interpret this temperature data to a flow rate profile, an interpretation model is set up. Table 5.1 and Table 5.2 show the rock and fluid properties as well as the reservoir and fracture information.

Table 5.1 Rock and fluid properties

Media	Parameter	Value
Rock	Rock Density, kg/m^3	3560
	Thermal conductivity, W/m·K	2.1
	Specific heat, J/kg·K	847
	Pore compressibility, 1/psia	6.89E-06
Water	Density, kg/m^3	985.9
	Thermal conductivity, W/m·K	0.66
	Specific heat, J/kg·K	4136
	Viscosity, cp	0.55
	Compressibility, 1/psia	3.0E-06
	Thermal expansibility, 1/K	4.80E-03
Oil	Density, kg/m^3	827
	Thermal conductivity, W/m·K	0.159
	Specific heat, J/kg·K	2219
	Viscosity, cp	0.78
	Formation volume factor, m^3/m^3	1.53
	Solution gas/oil ratio, m^3/m^3	199
	Thermal expansibility, 1/K	8.0E-4

Table 5.2 Reservoir and fracture information

Region	Parameter	Value
Reservoir	Net pay thickness, m	240
	Matrix permeability, nD	200
	Matrix porosity, %	4.79
	Initial pressure, kg/cm^2	640
	Reservoir temperature gradient, °C/m	0.031
	Residual water saturation, fraction	0.1
Fracture	Fracture width, m	0.0015
	Fracture porosity, %	20
	Fracture height, m	116
	Fracture permeability, mD	1000

From Figure 5.2 and Figure 5.3, we observed that the measured temperature is lower than the geothermal temperature. Also, at some cluster locations, there is a sharp temperature drop at the cluster location, and the temperature gradually recovers as the fluid flowing towards the heel. During hydraulic fracturing, because of injection fluid with low temperature entering the formation/fracture, the temperature around the well is lower than the surrounding formation temperature. The locations take more injection fluid would have a lower temperature. After shut-in, the temperature warms up, and this warm-back continues during production time (Li and Zhu 2016). As liquid-phase flows, either through the porous medium or production pipe, fractional heating also increases fluid temperature. Yoshida et al. (2018) have found that the temperature around the fracture cannot fully recover back to the initial geothermal temperature even after a reasonably long period of shut-in. Combining this finding with the observations mentioned above, the temperature

around the well has been cooled down due to the injection during hydraulic fracturing. After shut-in, the temperature around the fractures is still lower than the initial geothermal temperature (green line in Figure 5.3). During production, the cold fluid flowing into the wellbore can cause a sudden temperature drop at the cluster locations. Meanwhile, the Joule-Thomson heating effect of the liquid (oil or water) will compete with this cooling and can reduce or balance this temperature change. Considering all these effects, we need to start from the geothermal temperature, simulate the temperature from the injection, shut-in, to production for oil-water two-phase flow, which makes the developed multiphase black-oil thermal model in Chapter 2 a good candidate as the forward model.

Figure 5.4 shows an example of the forward model simulation domain. The simulation is from the injection, shut-in to the production. In this example, the stage has an injection time of 100 min with an injection rate of 70 bpm. The injection fluid temperature is 11 $^{\circ}$C, and the geothermal temperature is 106.2 $^{\circ}$C. Then the stage is shut-down for 49 days until it starts production. The production time is 71 days. In this forward example, the three fractures are the same. However, in the inversion, the fracture half-length is adjusted in order to match the measured temperature with the simulated temperature. The inversion results will be shown in the next section.

Figure 5.5 shows the inflow temperature at each different time period. The inflow temperature is defined as the fluid temperature at the intersection of the fracture and wellbore before the inflow fluid mixes with the wellbore fluid. As shown in this figure, we can see that the inflow temperature is still not fully recovered back to the geothermal temperature even after 49 days of shut-in.

115
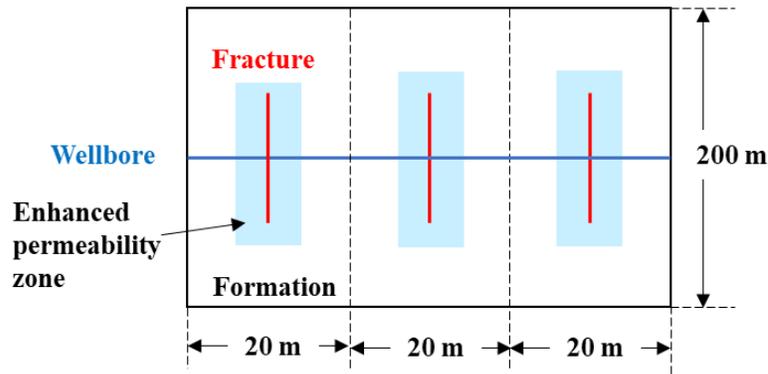
Figure 5.4 Forward model simulation domain
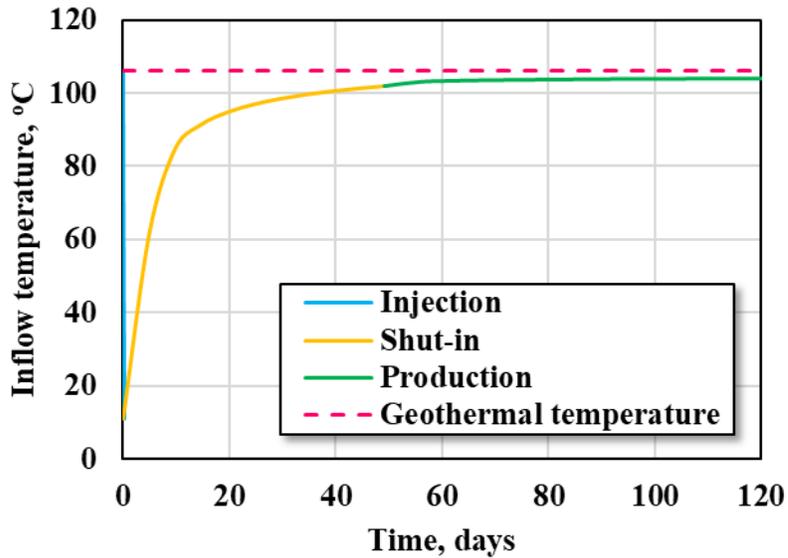
Figure 5.5 Inflow temperature at different period

The forward model is used to simulate the temperature profile. Meanwhile, an inversion model is needed to match the simulated temperature with the measured temperature and to update the inversion parameters through iterations. Chapter 3 and Chapter 4 have presented the general interpretation procedure for downhole temperature measurement interpretation in multi-stage fractured horizontal wells and the field example

of temperature interpretation for single-phase gas production. The general interpretation procedure can be applied in this field example, but additional procedures are needed because of two-phase flow.

5.3.2 Modified Interpretation Methodology and Results

In this field case, it is assumed that there is no formation water produced, and the produced water is from the flow back of the fracture fluid for hydraulic fracturing. The interpretation procedures consist of three main steps.

Step 1: invert oil flow rate by assuming single-phase oil production. A reasonable initial guess is essential for a quick conversion. At the downhole condition, the total water production rate is about 12% of the total flow rate (oil and water). Hence, we start by assuming there is only oil produced from the well. Starting from Stage 9 (the first stage that has temperature data), the temperature of this stage is simulated using the developed black-oil thermal model starting from the injection, then shut-in, and to production. By applying the general interpretation procedure, we can match the simulated wellbore temperature with the measured temperature. Through this, we obtain the oil flow rate profile for each fracture in this stage. Then we move to the next stage and obtain the oil flow rate profile for that stage. Once we finish inversion for all the stages, we need to confirm the total inverted oil flow rate matches the total oil rate which is converted from the measured surface rate to the downhole condition.

Step 2: ratio the water flow rate to each fracture according to the oil flow rate profile from step 1, assuming the water-oil-ratio is constant along the entire wellbore.

117

Figure 5.6 shows the inverted oil flow rate profile from step 1 and the assigned water flow rate based on oil rate distribution for step 2. Also, the inverted oil flow rate from the first eight stages is 46 m^3/day with the total water flow rate of 6.3 m^3/day at the downhole condition. By adding the water production, the simulated temperature changes and no longer match the measured temperature. However, for those fractures with small production rate such as those in Stage 13, adding such a small amount of water does not change the temperature in this stage significantly. Only at the fracture locations where the flow rate is relatively large, further inversion is needed.
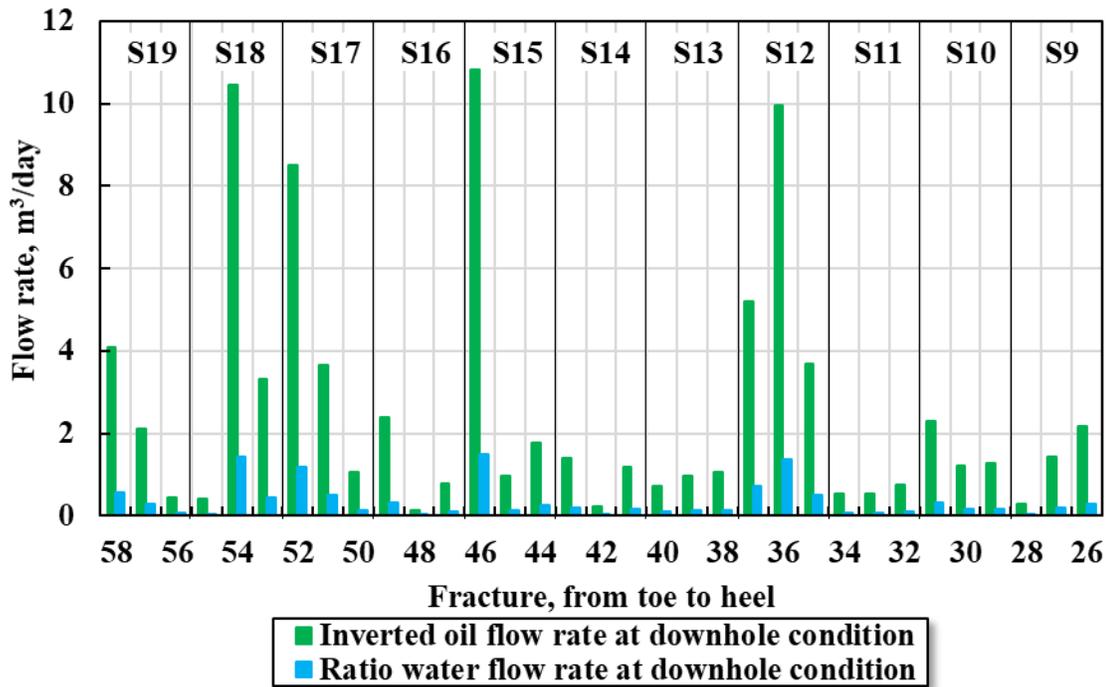

Figure 5.6 Flow rate profile from steps 1 and 2

Step 3: re-match the temperature by adjusting water-oil-ratio locally only for high flow rate fractures. From step 2, we can see that Stages 12, 15, 17, 18 and 19 have a relatively high flow rate. At these stages, adding water production will change the

simulated temperature which results in a mismatch of temperature. A further inversion for these stages is needed to re-match the temperature profile. To do so, we release the water-oil-ratio assumption used in step 2 and allow a moderately different water-oi-ratio at these stages. In this step, we still need to meet the total production rate constraint. Eventually, we obtained the inverted oil and water flow rate profile which is shown in Figure 5.7. The oil and water flow rate from the first eight stages keeps the same, 46 m^3/day and 6.3 m^3/day respectively. Figure 5.8 shows the inverted temperature with the measured temperature. The inverted temperature matches the measured temperature very well with the mean squared error (MSE) of 8.15e-5 and R-squared (R^2) of 0.96.

With the interpretation of temperature to flow rate profile, we can see that the flow rate varies dramatically along the horizontal well. Figure 5.9 shows the comparison of oil rate distribution to a constant rate distribution. This uneven rate distribution may be caused by formation heterogeneity or well completion issues.
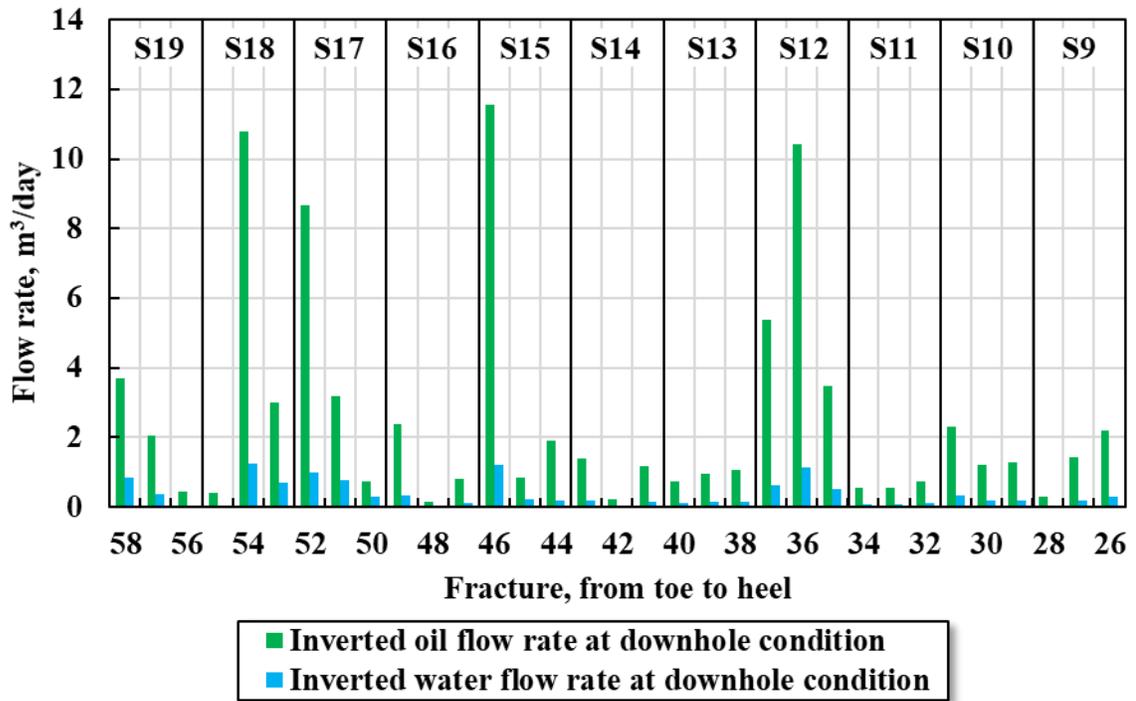
Figure 5.7 Flow rate profile from step 3
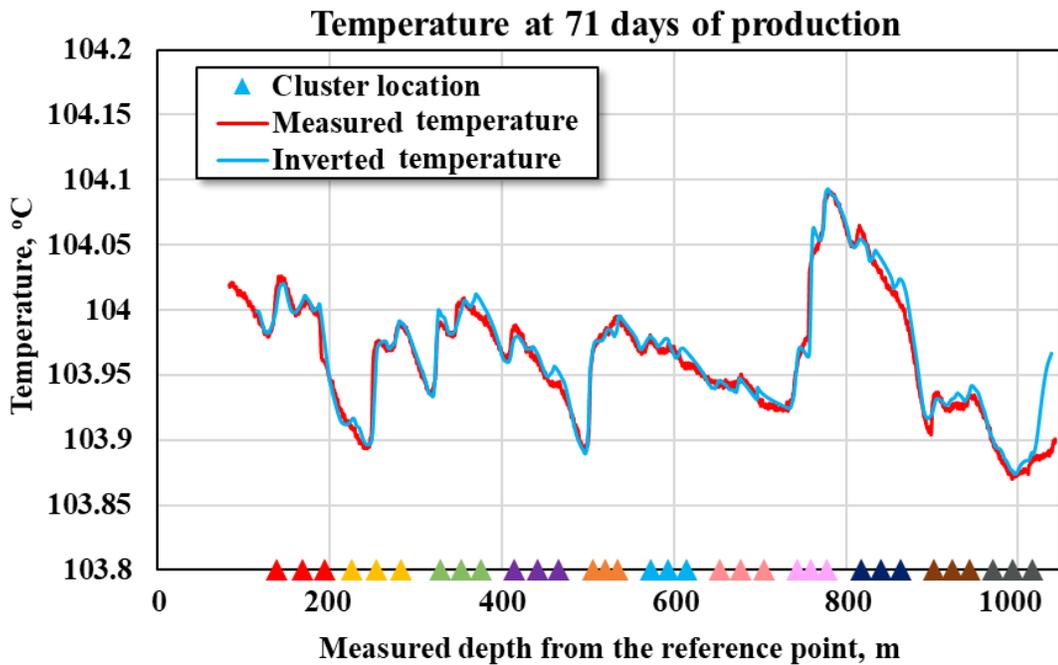
Figure 5.8 Inverted temperature matches the measured temperature
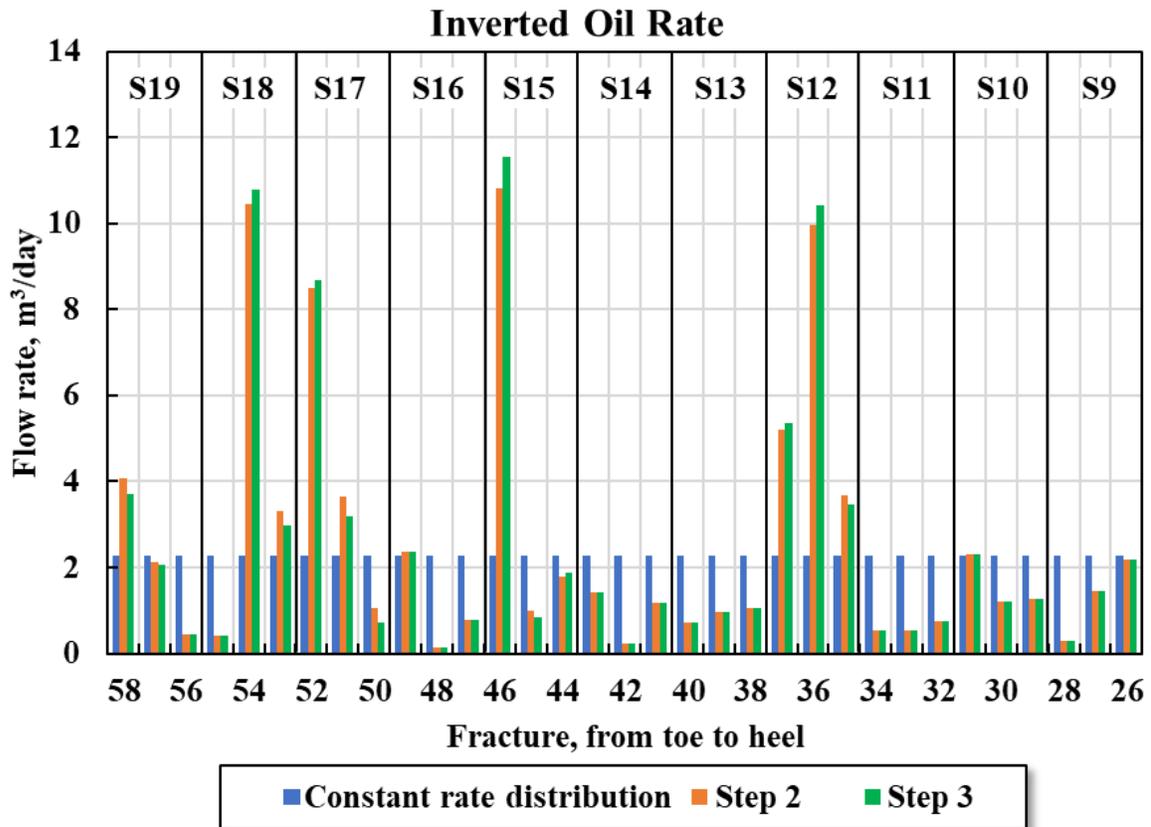
Figure 5.9 Oil rate profile at the downhole condition

5.3.3 Discussion

Of all assumption made, the critical one, which is also the weakest one, is to assume that the water-oil ratio at each fracture is a constant. The assumption leads to the interpretation results. Because we also assumed that there is no water aquifer near-by, and the produced water is fracture fluid, the constant water-oil ratio assumption is tolerable. If the water source is other than fracture fluid, this approach can result in high errors.

The two-phase oil-water flow problem is a challenging problem. To start with, we do not have a large temperature difference to work with as we do in gas producing wells. For gas producing well, gas flow through formation and fractures makes the temperature

further reduces, in addition to the injection of cold fluid, enhancing the possibility to interpret flow distribution. Oppositely, oil production results in a slightly increased temperature because of frictional heating, reducing the temperature signals because of cold fluid injection. The temperature changes caused by liquid flow is much smaller compared with gas flow, adding more difficulty to interpretation. Higher resolution measurement is more critical for oil-producing wells than for gas-producing wells.

Interpreting temperature for flow distribution is a complex problem. There are many parameters involved, from reservoir properties to well structure and completion, to fracturing design and operation. For example, the general idea of the liquid-flowing well should yield an increased temperature because of flow. If we do not simulate the temperature from the beginning of injection, we cannot explain why the temperature is below the geothermal temperature for a liquid-flowing well, and the interpretation can be completely wrong. Eventually, the cold signal of injection diminishes. This period can be days, weeks or even months. The field case presented in the paper is a good example illustrating that each case should be interpreted based on well operation condition.

Finally, using monitored temperature interpretation only can provide a flow rate distribution. Additional monitoring/measurements/testing are needed to obtain more information such as fracture operation, completion efficiency or reservoir permeability distribution.

5.4 Section Summary

This chapter presents the interpretation of the temperature measurements from production logging tools for oil/water production in a multi-stage hydraulic fractured horizontal well. From this interpretation, we obtain the oil and water production rate profile. Only one set of temperature measurements can result in large uncertainties. In this situation, a reasonable initial point and necessary assumptions are critical to a sensible solution. In oil/water two-phase production well, the influences on the temperature of the water production are not significant when the flow rate is low.

Interpretation of temperature for flow rate profile depends on many parameters such as reservoir properties, well structure, and completion design. It is essential to analyze the temperature case by case based on the well operation condition. Interpretation of temperature can provide the flow rate profile for the multi-stage fractured well. Additional constraints are needed to obtain more information about the fracture.

CHAPTER VI

CONCLUSIONS

In this dissertation, a downhole temperature interpretation procedure is proposed. This interpretation procedure includes two main parts.

The first part is the development of the multi-phase black-oil thermal model to simulate the transient temperature behavior during hydraulic fracturing fluid injection, shut-in, and well production. This model includes a reservoir model and a wellbore model, which are coupled iteratively through the boundary conditions. The model is validated against the compositional model, semi-analytical model, and analytical solution. This model shows a consistent result as the other models.

The second part is the inversion procedure which consists of four main steps including the pre-processing of the measured data, initial evaluation, local temperature matching, and global re-examination. A sensitivity study is performed to identify the most influential parameters. The interpretation procedure is then applied to a synthetic example which proves that the inversion procedure is feasible as a promising tool to interpret downhole temperature data quantitatively.

The established temperature interpretation procedure is applied to two field cases. One is a single-phase gas producing horizontal well with multiple hydraulic fractures. The other one is for two-phase oil/water production in a multi-stage hydraulic fractured horizontal well. Both field examples have shown the successful application of this proposed temperature interpretation procedure.

Based on the study in this dissertation, the main conclusions are summarized below:

(1) The developed black-oil thermal model shows its robustness to handle the multi-phase flow and meantime maintains its computational efficiency. Compared with the compositional model, this model has a faster computational speed. Compared with the semi-analytical model, this model can handle two-phase oil/water or gas/liquid flow and heterogeneous reservoirs.

(2) When the influence of the composition changes and the impact of near wellbore flow convergence on temperature are significant, this developed black-oil thermal model may have deviation. This model applies to most of the common field conditions.

(3) The sensitivity study identified the most influential parameters to the temperature behavior, which are the fracture half-length, matrix porosity, and fracture permeability.

(4) In the interpretation for gas producing well, the initial evaluation to eliminate the non-producing fractures based on the temperature gradient reduces the problem size and improves the computational efficiency.

(5) In the interpretation procedure, the non-uniform initial guess and necessary assumptions are critical to faster convergence and a sensible solution with fewer uncertainties. Also, the non-uniform initial guess allows the gradient method for inversion being used with less chance of local minimization trap.

(6) In oil/water two-phase production well, the influences on the temperature of the water production are insignificant when the flow rate is low.

(7) Interpretation of temperature can provide the flow rate profile for the multi-stage fractured well. Additional constraints are needed to obtain more information about the fracture.

(8) Interpretation of temperature for flow rate profile depends on many parameters such as reservoir properties, well structure, and completion design. It is essential to analyze the temperature case by case based on the well operation condition.

(9) Because of the large number of parameters involved in temperature interpretation, and because the temperature is only measured along the wellbore, a non-unique solution is a common problem, and engineering judgment should be applied to ensure a more accurate interpretation.

REFERENCES

Al-Najim, A., Zahedi, A., Al-Khonaini, T. et al. 2012. A New Methodology for Stimulation of a High-Water-Cut Horizontal Oil Well through the Combination of a Smart Chemical System with Real-Time Temperature Sensing: A Case Study of South Umm Gudair Field, Pz Kuwait. Paper presented at the SPE/ICoTA Coiled Tubing & Well Intervention Conference and Exhibition, The Woodlands, Texas, USA. 10. Society of Petroleum Engineers SPE-154387-MS. DOI: 10.2118/154387-MS.

App, J. and Yoshioka, K. 2013. Impact of Reservoir Permeability on Flowing Sandface Temperatures: Dimensionless Analysis. *SPE Journal* **18** (04): 685-694. DOI: 10.2118/146951-PA

Aslanyan, A., Wilson, M., Al Shammakhy, A. et al. 2013. Evaluating Injection Performance with High-Precision Temperature Logging and Numerical Temperature Modelling. Paper presented at the SPE Reservoir Characterization and Simulation Conference and Exhibition, Abu Dhabi, UAE. 14. SPE-166007-MS. DOI: 10.2118/166007-MS.

Attia, A., Brady, J., Lawrence, M. et al. 2019. Validating Refrac Effectiveness with Carbon Rod Conveyed Distributed Fiber Optics in the Barnett Shale for Devon Energy. Paper presented at the SPE Hydraulic Fracturing Technology Conference and Exhibition, The Woodlands, Texas, USA. 10. SPE-194338-MS. DOI: 10.2118/194338-MS.

Bello, O., Bale, D.S., Yang, L. et al. 2018. Integrating Downhole Temperature Sensing Datasets and Visual Analytics for Improved Gas Lift Well Surveillance. Paper presented at the SPE Annual Technical Conference and Exhibition, Dallas, Texas, USA. 14. SPE-191626-MS. DOI: 10.2118/191626-MS.

Biot, M.A., Masse, L., and Medlin, W.L. 1987. Temperature Analysis in Hydraulic Fracturing. *Journal of Petroleum Technology* **39** (11): 1389-1397. DOI: 10.2118/13228-PA

Chen, N.H. 1979. An Explicit Equation for Friction Factor in Pipe. *Industrial Engineering Chemistry Fundamentals* **18** (3): 296-297.

Chen, R., Xue, X., Yao, C. et al. 2018. Coupled Fluid Flow and Geomechanical Modeling of Seismicity in the Azle Area North Texas. Paper presented at the SPE Annual Technical Conference and Exhibition, Dallas, Texas, USA. 19. SPE-191623-MS. DOI: 10.2118/191623-MS.

Corey, A.T. 1954. The Interrelation between Gas and Oil Relative Permeabilities. *Producers Monthly* **19** (1): 38-41.

Cui, J. 2015. Diagnosis of Multi-Stage Fracture Stimulation in Horizontal Wells by Downhole Temperature Measurements. Ph.D. dissertation, Texas A&M University.

Cui, J., Yang, C., Zhu, D. et al. 2016b. Fracture Diagnosis in Multiple-Stage-Stimulated Horizontal Well by Temperature Measurements with Fast Marching Method. *SPE Journal* **21** (06): 2289-2300. DOI: 10.2118/174880-PA

Cui, J., Zhu, D., and Jin, M. 2016a. Diagnosis of Production Performance after Multistage Fracture Stimulation in Horizontal Wells by Downhole Temperature Measurements. *SPE Production & Operations* **31** (04): 280-288. DOI: 10.2118/170874-PA

Davarpanah, A., Mirshekari, B., Behbahani, T.J. et al. 2017. Application of Production Logging Tools in Estimating the Permeability of Fractured Carbonated Reservoirs: A Comparative Study. *Journal of Petroleum and Gas Engineering* **8** (5): 36-41.

Davis, E.R., Zhu, D., and Hill, A.D. 1997. Interpretation of Fracture Height from Temperature Logs - the Effect of Wellbore/Fracture Separation. *SPE Formation Evaluation* **12** (02): 119-124. DOI: 10.2118/29588-PA

Deng, L. and King, M.J. 2018. Theoretical Investigation of Water Blocking in Unconventional Reservoirs Due to Spontaneous Imbibition and Water Adsorption. Paper presented at the SPE/AAPG/SEG Unconventional Resources Technology Conference, Houston, Texas, USA. 18. Unconventional Resources Technology Conference URTEC-2875353-MS. DOI: 10.15530/URTEC-2018-2875353.

Deng, L. and King, M.J. 2019. Theoretical Investigation of the Transition from Spontaneous to Forced Imbibition. *SPE Journal* **24** (01): 215-229. DOI: 10.2118/190309-PA

Dittus, F.W. and Boelter, L.M.K. 1930. Heat Transfer in Automobile Radiators of the Tubular Type. *University of California Publications of Engineering* **2**: 443-461.

Dranchuk, P.M. and Abou-Kassem, H. 1975. Calculation of Z Factors for Natural Gases Using Equations of State. *Journal of Canadian Petroleum Technology* **14** (03): 34-37. DOI: 10.2118/75-03-03

Duru, O.O. and Horne, R.N. 2010. Modeling Reservoir Temperature Transients and Reservoir-Parameter Estimation Constrained to the Model. *SPE Reservoir Evaluation & Engineering* **13** (06): 873-883. DOI: 10.2118/115791-PA

EIA. **https://www.eia.gov/maps/images/shale_gas_lower48.pdf**. Accessed March 2019.

Ertekin, T., Abou-Kassem, J.H., and King, G.R. 2001. *Basic Applied Reservoir Simulation*. Richardson, TX USA: Society of Petroleum Engineers. Original edition. ISBN 978-1-55563-089-8.

Gonzalez, S., Al Rashidi, H., Pandey, D.C. et al. 2018. Real-Time Fiber-Optics Monitoring of Steam Injection in Unconsolidated High Viscous Formation. Paper presented at the SPE EOR Conference at Oil and Gas West Asia, Muscat, Oman. 16. SPE-190362-MS. DOI: 10.2118/190362-MS.

Halliburton.com. Fiber-Optic Sensing Technologies. **https://www.halliburton.com/content/dam/ps/public/pinnacle/contents/Brochures/web/fiber-optics.pdf**. Accessed March, 2019.

Harrington, L.J., Hannah, R.R., and Robert, B. 1978. Post Fracturing Temperature Recovery and Its Implication for Stimulation Design. Paper presented at the SPE Annual Fall Technical Conference and Exhibition, Houston, Texas. 6. Society of Petroleum Engineers SPE-7560-MS. DOI: 10.2118/7560-MS.

Hartley, H.O. 1961. The Modified Gauss-Newton Method for the Fitting of Non-Linear Regression Functions by Least Squares. *Technometrics* **3** (2): 269-280.

Hasan, A.R., Kabir, C.S., and Wang, X. 1997. Development and Application of a Wellbore/Reservoir Simulator for Testing Oil Wells. *SPE Formation Evaluation* **12** (03): 182-188. DOI: 10.2118/29892-PA

Hill, A.D. 1990. *Production Logging: Theoretical and Interpretive Elements*. Richardson, TX USA: Society of Petroleum Engineers. Original edition. ISBN 1555630308.

Hoang, H.N., Mahadevan, J., and Lopez, H. 2012. Injection Profiling During Limited-Entry Fracturing Using Distributed-Temperature-Sensor Data. *SPE Journal* **17** (03): 752-767. DOI: 10.2118/140442-PA

Holland, J.H. 1992. Genetic Algorithms. *Scientific American* **267** (1): 66-73.

Huang, J., Yang, C., Xue, X. et al. 2016. Simulation of Coupled Fracture Propagation and Well Performance under Different Refracturing Designs in Shale Reservoirs. Paper presented at the SPE Low Perm Symposium, Denver, Colorado, USA. 26. Society of Petroleum Engineers SPE-180238-MS. DOI: 10.2118/180238-MS.

Jayawardena, S., Alkaya, B., Redus, C. et al. 2000. A New Model for Dispersed Multi-Layer Oil-Water Flow. In *BHR Group Conference Series Publication*, 40:77-90: Bury St. Edmunds; Professional Engineering Publishing; 1998.

Kamphuis, H., Davies, D.R., and Roodhart, L.P. 1993. A New Simulator for the Calculation of the in Situ Temperature Profile During Well Stimulation Fracturing Treatments. *Journal of Canadian Petroleum Technology* **32** (05): 10. DOI: 10.2118/93-05-03

Kragas, T.K., Williams, B.A., and Myers, G.A. 2001. The Optic Oil Field: Deployment and Application of Permanent in-Well Fiber Optic Sensing Systems for Production and Reservoir Monitoring. Paper presented at the SPE Annual Technical Conference and Exhibition, New Orleans, Louisiana. 9. SPE-71529-MS. DOI: 10.2118/71529-MS.

Li, X. and Zhu, D. 2016. Temperature Behavior of Multi-Stage Fracture Treatments in Horizontal Wells. Paper presented at the SPE Asia Pacific Hydraulic Fracturing Conference, Beijing, China. SPE-181876-MS. DOI: 10.2118/181876-MS.

Li, Z. and Zhu, D. 2010. Predicting Flow Profile of Horizontal Well by Downhole Pressure and Distributed-Temperature Data for Waterdrive Reservoir. *SPE Production & Operations* **25** (03): 296-304. DOI: 10.2118/124873-PA

Liao, L. 2013. Interpretation of Array Production Logging Measurements in Horizontal Wells for Flow Profile. Master thesis, Texas A&M University.

Ma, X., Al-Harbi, M., Datta-Gupta, A. et al. 2008. An Efficient Two-Stage Sampling Method for Uncertainty Quantification in History Matching Geological Models. *SPE Journal* **13** (01): 77-87. DOI: 10.2118/102476-PA

McGinley, M., Zhu, D., and Hill, A.D. 2015. The Effects of Fracture Orientation and Elastic Property Anisotropy on Hydraulic Fracture Conductivity in the Marcellus Shale. Paper presented at the SPE Annual Technical Conference and Exhibition, Houston, Texas, USA. SPE-174870-MS. DOI: 10.2118/174870-MS.

Menkhaus, A., Ryan, T., Taboada Antona, J.P. et al. 2012. Fiber Optic Technology Allows Real-Time Production Logging Well Campaign to Continue Where Traditional Logging Tools Fell Short. Paper presented at the SPE/ICoTA Coiled Tubing & Well Intervention Conference and Exhibition, The Woodlands, Texas, USA. 9. SPE-154064-MS. DOI: 10.2118/154064-MS.

Meyer, B.R. 1989. Heat Transfer in Hydraulic Fracturing. *SPE Production Engineering* **4** (04): 423-429. DOI: 10.2118/17041-PA

MSEEL. Well Datasets. **http://www.mseel.org/research/research.html**. Accessed 02 March 2019.

Natareno, N., Thelen, M., Charbonneau, J. et al. 2019. Continuous Use of Fiber Optics-Enabled Coiled Tubing Used to Accelerate the Optimization of Completions Aimed at Improved Recovery and Reduced Cost of Development. Paper presented at the SPE Hydraulic Fracturing Technology Conference and Exhibition, The Woodlands, Texas, USA. 13. SPE-194331-MS. DOI: 10.2118/194331-MS.

Oliver, D.S., Reynolds, A.C., and Liu, N. 2008. *Inverse Theory for Petroleum Reservoir Characterization and History Matching*. Cambridge, UK: Cambridge University Press. Original edition. ISBN 1139472615.

Peaceman, D.W. 1993. Representation of a Horizontal Well in Numerical Reservoir Simulation. *SPE Advanced Technology Series* **1** (01): 7-16. DOI: 10.2118/21217-PA

Peacock, D.R. 1965. Temperature Logging. Paper presented at the Society of Professional Well Log Analysis 6th Annual Logging Symposium (Volume I), Dallas, Texas. SPWLA-1965-F.

Ramey, H.J., Jr. 1962. Wellbore Heat Transmission. *Journal of Petroleum Technology* **14** (04): 427-435. DOI: 10.2118/96-PA

Ribeiro, P.M. and Horne, R.N. 2013. Pressure and Temperature Transient Analysis: Hydraulic Fractured Well Application. Paper presented at the SPE Annual Technical Conference and Exhibition, New Orleans, Louisiana, USA. 21. Society of Petroleum Engineers SPE-166222-MS. DOI: 10.2118/166222-MS.

Ribeiro, P.M. and Horne, R.N. 2014. Detecting Fracture Growth out of Zone Using Temperature Analysis. Paper presented at the SPE Annual Technical Conference and Exhibition, Amsterdam, The Netherlands. 24. Society of Petroleum Engineers SPE-170746-MS. DOI: 10.2118/170746-MS.

Roberts, G., Whittaker, J.L., and McDonald, J. 2018. A Novel Hydraulic Fracture Evaluation Method Using Downhole Video Images to Analyse Perforation Erosion. Paper presented at the SPE International Hydraulic Fracturing Technology Conference and Exhibition, Muscat, Oman. 14. SPE-191466-18IHFT-MS. DOI: 10.2118/191466-18IHFT-MS.

Ruder, S. 2016. An Overview of Gradient Descent Optimization Algorithms. *arXiv.org preprint*.

Sahdev, N. and Cook, P.F. 2016. Coiled Tubing Deployed Fiber Optics Utilized in Observing Cross-Well Communication During Stimulation. Paper presented at the SPE/AAPG/SEG Unconventional Resources Technology Conference, San Antonio, Texas, USA. 26. URTEC-2430791-MS. DOI: 10.15530/URTEC-2016-2430791.

Schlumberger. 2009. *The Essentials of Fiber-Optic Distributed Temperature Analysis*. Sugar Land, Texas, USA: Schlumberger. Original edition. ISBN 1937949133.

Seth, G., Reynolds, A.C., and Mahadevan, J. 2010. Numerical Model for Interpretation of Distributed-Temperature-Sensor Data During Hydraulic Fracturing. Paper presented at the SPE Annual Technical Conference and Exhibition, Florence, Italy. SPE-135603-MS. DOI: 10.2118/135603-MS.

Shi, H., Holmes, J.A., Durlofsky, L.J. et al. 2005. Drift-Flux Modeling of Two-Phase Flow in Wellbores. *SPE Journal* **10** (01): 24-33. DOI: 10.2118/84228-PA

Shirdel, M., Buell, R.S., Wells, M. et al. 2016. Horizontal Steam Injection Flow Profiling Using Fiber Optics. Paper presented at the SPE Annual Technical Conference and Exhibition, Dubai, UAE. 27. SPE-181431-MS. DOI: 10.2118/181431-MS.

Sierra, J.R., Kaura, J.D., Gualtieri, D. et al. 2008. Dts Monitoring of Hydraulic Fracturing: Experiences and Lessons Learned. Paper presented at the SPE Annual Technical Conference and Exhibition, Denver, Colorado, USA. 15. Society of Petroleum Engineers SPE-116182-MS. DOI: 10.2118/116182-MS.

Starling, K.E. 1973. *Fluid Thermodynamic Properties for Light Petroleum Systems*. Houston, TX USA: Gulf Publishing Co. Original edition. ISBN 087201293X.

Tabatabaei, M. and Zhu, D. 2012. Fracture-Stimulation Diagnostics in Horizontal Wells through Use of Distributed-Temperature-Sensing Technology. *SPE Production & Operations* **27** (04): 356-362. DOI: 10.2118/148835-PA

Tang, J., Ehlig-Economides, C., Fan, B. et al. 2019. A Microseismic-Based Fracture Properties Characterization and Visualization Model for the Selection of Infill Wells in Shale Reservoirs. *Journal of Natural Gas Science and Engineering* **67**: 147-159.

Tang, J. and Wu, K. 2018. A 3-D Model for Simulation of Weak Interface Slippage for Fracture Height Containment in Shale Reservoirs. *International Journal of Solids and Structures* **144**: 248-264.

Tang, J., Wu, K., Li, Y. et al. 2018a. Numerical Investigation of the Interactions between Hydraulic Fracture and Bedding Planes with Non-Orthogonal Approach Angle. *Engineering Fracture Mechanics* **200**: 1-16.

Tang, J., Wu, K., Zeng, B. et al. 2018b. Investigate Effects of Weak Bedding Interfaces on Fracture Geometry in Unconventional Reservoirs. *Journal of Petroleum Science and Engineering* **165**: 992-1009.

Tarantola, A. 2005. *Inverse Problem Theory and Methods for Model Parameter Estimation*. Paris, France: Society for Industrial and Applied Mathematics. Original edition. ISBN 0-89871-572-5.

Tardy, P.M.J., Ramondenc, P., Weng, X. et al. 2011. Inversion of Dts Logs to Measure Zonal Coverage During and after Wellbore Treatments with Coiled Tubing. Paper presented at the SPE/ICoTA Coiled Tubing & Well Intervention Conference and Exhibition, The Woodlands, Texas. SPE-143331-MS. DOI: 10.2118/143331-MS.

Tardy, P.M.J., Ramondenc, P., Weng, X. et al. 2012. Inversion of Distributed-Temperature-Sensing Logs to Measure Zonal Coverage During and after Wellbore Treatments with Coiled Tubing. *SPE Production & Operations* **27** (01): 78-86. DOI: 10.2118/143331-PA

Towler, B.F. 2002. *Fundamental Principles of Reservoir Engineering*. Richardson, TX USA: Society of Petroleum Engineers. Original edition. ISBN 978-1-55563-092-8.

Ugueto, G.A., Huckabee, P.T., and Molenaar, M.M. 2015. Challenging Assumptions About Fracture Stimulation Placement Effectiveness Using Fiber Optic Distributed Sensing Diagnostics: Diversion, Stage Isolation and Overflushing. Paper presented at the SPE Hydraulic Fracturing Technology Conference, The Woodlands, Texas, USA. 12. SPE-173348-MS. DOI: 10.2118/173348-MS.

Ugueto, G.A., Huckabee, P.T., Molenaar, M.M. et al. 2016. Perforation Cluster Efficiency of Cemented Plug and Perf Limited Entry Completions; Insights from Fiber Optics Diagnostics. Paper presented at the SPE Hydraulic Fracturing Technology Conference, The Woodlands, Texas, USA. 17. Society of Petroleum Engineers SPE-179124-MS. DOI: 10.2118/179124-MS.

Ugueto, G.A., Huckabee, P.T., Reynolds, A. et al. 2018a. Hydraulic Fracture Placement Assessment in a Fiber Optic Compatible Coiled Tubing Activated Cemented Single Point Entry System. Paper presented at the SPE Hydraulic Fracturing Technology Conference and Exhibition, The Woodlands, Texas, USA. 13. SPE-189842-MS. DOI: 10.2118/189842-MS.

Ugueto, G.A., Wojtaszek, M., Huckabee, P.T. et al. 2018b. Accelerated Stimulation Optimization Via Permanent and Continuous Production Monitoring Using Fiber Optics. Paper presented at the SPE/AAPG/SEG Unconventional Resources Technology Conference, Houston, Texas, USA. 12. Unconventional Resources Technology Conference URTEC-2901897-MS. DOI: 10.15530/URTEC-2018-2901897.

Van Laarhoven, P.J. and Aarts, E.H. 1987. *Simulated Annealing: Theory and Applications*. Dordrecht: Kluwer Academic Publishers. Original edition. ISBN 978-90-481-8438-5

Vazquez, M. and Beggs, H.D. 1977. Correlations for Fluid Physical Property Prediction. Paper presented at the SPE Annual Fall Technical Conference and Exhibition, Denver, Colorado, USA. SPE-6719-MS. DOI: 10.2118/6719-MS.

West Virginia GIS Technical Center. Unconventional Hydrocarbon Resources. **http://www.unconventionalenergyresources.org/docs/shaleGasBasinsWorld.pdf**. Accessed March 2019.

Whittaker, C. 2013. *Fundamentals of Production Logging*. Houston, Texas, USA: Schlumberger. Original edition. ISBN 1937949079.

Winterton, R.H. 1998. Where Did the Dittus and Boelter Equation Come From? *International journal of heat and mass transfer* **41** (4-5): 809-810.

Xie, J., Huang, H., Ma, H. et al. 2018. Numerical Investigation of Effect of Natural Fractures on Hydraulic-Fracture Propagation in Unconventional Reservoirs. *Journal of Natural Gas Science and Engineering* **54**: 143-153.

Xu, B., Kabir, S., and Hasan, A.R. 2018. Modeling Coupled Nonisothermal Reservoir/Wellbore Flow Behavior in Gas Reservoir Systems. Paper presented at the SPE Western Regional Meeting, Garden Grove, California, USA. 19. SPE-190067-MS. DOI: 10.2118/190067-MS.

Xue, X., Rey, A., Muron, P. et al. 2019a. Simplification and Simulation of Fracture Network Using Fast Marching Method and Spectral Clustering for Embedded Discrete Fracture Model. Paper presented at the SPE Hydraulic Fracturing Technology Conference and Exhibition, The Woodlands, Texas, USA. 15. SPE-194368-MS. DOI: 10.2118/194368-MS.

Xue, X., Yang, C., Onishi, T. et al. 2019b. Modeling Hydraulically Fractured Shale Wells Using the Fast Marching Method with Local Grid Refinements Lgrs and Embedded Discrete Fracture Model Edfm. *SPE Journal* **preprint**. DOI: 10.2118/193822-PA

Xue, X., Yang, C., Park, J. et al. 2018. Reservoir and Fracture-Flow Characterization Using Novel Diagnostic Plots. *SPE Journal* **Preprint**. DOI: 10.2118/194017-PA

Yang, C., Xue, X., Huang, J. et al. 2016. Rapid Refracturing Candidate Selection in Shale Reservoirs Using Drainage Volume and Instantaneous Recovery Ratio. Paper presented at the SPE/AAPG/SEG Unconventional Resources Technology Conference, San Antonio, Texas, USA. 16. URTEC-2459368-MS. DOI: 10.15530/URTEC-2016-2459368.

Yang, D., Xue, X., and Chen, J. 2018. High Resolution Hydraulic Fracture Network Modeling Using Flexible Dual Porosity Dual Permeability Framework. Paper presented at the SPE Western Regional Meeting, Garden Grove, California, USA. 14. Society of Petroleum Engineers SPE-190096-MS. DOI: 10.2118/190096-MS.

Yoshida, N. 2016. Modeling and Interpretation of Downhole Temperature in a Horizontal Well with Multiple Fractures. Ph.D. dissertation, Texas A&M University.

Yoshida, N., Hill, A.D., and Zhu, D. 2018. Comprehensive Modeling of Downhole Temperature in a Horizontal Well with Multiple Fractures. *SPE Journal* **25** (05): 1580-1602. DOI: 10.2118/181812-PA

Yoshioka, K. 2007. Detection of Water or Gas Entry into Horizontal Wells by Using Permanent Downhole Monitoring Systems. Ph.D. dissertation, Texas A&M University.

Yoshioka, K., Zhu, D., Hill, A.D. et al. 2007. Prediction of Temperature Changes Caused by Water or Gas Entry into a Horizontal Well. *SPE Production & Operations* **22** (04): 425-433. DOI: 10.2118/100209-PA

Zhang, F., Adel, I.A., Park, K.H. et al. 2018a. Enhanced Oil Recovery in Unconventional Liquid Reservoir Using a Combination of Co2 Huff-N-Puff and Surfactant-Assisted Spontaneous Imbibition. Paper presented at the SPE Annual Technical Conference and Exhibition, Dallas, Texas, USA. 20. SPE-191502-MS. DOI: 10.2118/191502-MS.

Zhang, F., Saputra, I.W.R., Adel, I.A. et al. 2018b. Scaling for Wettability Alteration Induced by the Addition of Surfactants in Completion Fluids: Surfactant Selection for Optimum Performance. Paper presented at the SPE/AAPG/SEG Unconventional Resources Technology Conference, Houston, Texas, USA. 17. Unconventional Resources Technology Conference URTEC-2889308-MS. DOI: 10.15530/URTEC-2018-2889308.

Zuber, N. and Findlay, J.A. 1965. Average Volumetric Concentration in Two-Phase Flow Systems. *Journal of Heat Transfer* **87** (4): 453-468. DOI: 10.1115/1.3689137